Semiclassical Electron Magnetotransport in Two-Dimensional Lorentz Gases

Inaugural-Dissertation

zur Erlangung des Doktorgrades
der Mathematisch-Naturwissenschaftlichen Fakultät
der Heinrich-Heine-Universität Düsseldorf

vorgelegt von

BEATE HORN-COSFELD

aus Köln

DÜSSELDORF, MÄRZ 2020

aus dem Institut für Experimentelle Physik der kondensierten Materie
der Heinrich-Heine-Universität Düsseldorf

Gedruckt mit der Genehmigung der
Mathematisch-Naturwissenschaftlichen Fakultät der
Heinrich-Heine-Universität Düsseldorf

Berichterstatter:
1. Prof. Dr. Thomas Heinzel
2. Prof. Dr. Jürgen Horbach

Tag der mündlichen Prüfung: 24.09.2020

ZUSAMMENFASSUNG

Die vorliegende Arbeit befasst sich mit dem klassischen Elektronentransport in zwei Dimensionen. Die Elektronen bewegen sich in einer Ebene und streuen elastisch an künstlichen, zufällig verteilten Streuzentren gleicher Form. Ein solches System nennt man *zweidimensionales Lorentzgas*. Die zweidimensionale Ebene, in der sich Elektronen bei Helium-Temperatur ballistisch bewegen formt sich an der Heterostruktur von modulationsdotiertem $\mathrm{GaAs/Al}_x\mathrm{Ga}_{1-x}\mathrm{As}$. Die Lorentzgas-Streuer werden durch Ätzen in die Kristalloberfläche realisiert. Ein Magnetfeld zwingt die Elektronen auf Kreisbahnen, wodurch der Spannungsabfall entlang der Probe verändert wird. Dies erlaubt es auf verschiedene Transporteffekte des zweidimensionalen Lorentzgases Rückschlüsse zu ziehen. Die Streuerpositionen sind statisch, sodass die Streuung der Elektronen korreliert ist, was zu sogenannten *Memoryeffekten* führt und der Elektronentransport stark von den Vorhersagen des Drude-Boltzmann-Modells abweicht. In den ersten drei Kapiteln werden fundamentale Konzepte umrissen. Die in dieser Arbeit erzielten experimentellen Ergebnisse werden in vier weiteren Kapiteln vorgestellt:

Kapitel drei untersucht zweidimensionale Lorentzgase retroreflektierender Kreuze hoher Dichte. Diese Form begünstigt den Memoryeffekt der „Retroreflektion“. Die Ergebnisse werden mit vorherigen Arbeiten an kreisförmigen Streuern verglichen. Gemeinsam ist ein Leitfähigkeitsmaximum im Magnetotransport, verursacht durch zielgerichteten Transport entlang der Lorentzgaskontur. Nur bei retroreflektierenden Lorentzgasen tritt bei niedrigen Magnetfeldern ein zusätzliches Maximum auf. Dieses markiert das Aufbrechen der Retroreflektion durch den reduzierten Zyklotronradius und ist eine Signatur anormaler Diffusion, was in molekular dynamischen Simulationen bestätigt wurde.

Im vierten Kapitel der Arbeit, wurde der Einfluss dynamischer und statischer Hintergrundstreuung auf den Magnetotransport kreisförmiger Lorentzgase untersucht. Bei niedrigen Magnetfeldern erhöht dynamische Streuung, verursacht durch Phononen, die Leitfähigkeit. Statische Streuung wird durch ein sekundäres Lorentzgas niedrigerer Dichte und Streuergröße verursacht und erniedrigt die Leitfähigkeit. Bei höheren Magnetfeldern hat die Art der Hintergrundstreuung keinen Einfluss auf die Leitfähigkeitsmodulation.

Im fünften Kapitel wird der Magnetowiderstand des unstrukturierten zweidimensionalen Elektronengases in Hinblick auf den „giant negative magnetoresistance“ untersucht. Dieser besteht aus zwei Maxima. Das innere Maximum wird nach jüngerer Literatur durch ein dünnes zweidimensionales Lorentzgas erklärt, gebildet durch probenwachstumsbedingte Defekte. Die Charakterisierung des Magnetowiderstandes niederdichter Lorentzgase bestätigt dies.

Zuletzt wurden zweidimensionale Lorentzgase durch verschiedene Einflüsse aus dem Gleichgewicht

gebracht. Unteranderem konnte gezeigt werden, dass elektromagnetische Bestrahlung im Terahertz-Bereich Widerstandsoszillationen induziert welche durch akustische Phononen hervorgerufen werden. Darüber hinaus wurden Hall-induzierte und Mikrowelleninduzierte Widerstandsoszillationen an Lorentzgasen vermessen.

ABSTRACT

This thesis focuses on classical electron transport in two dimensions. The electrons move in a plane and scatter elastically at intentionally implemented obstacles, which are equal in size and randomly distributed. Such a system is called a *two-dimensional Lorentz gas*. The two-dimensional plane in which electrons move ballistically at helium temperatures is formed at the heterostructure of GaAs/$\mathrm{Al_xGa_{1-x}As}$. Lorentz gas obstacles are realized by etching into the crystal plane. A magnetic field bends the electron trajectories on an orbit, thereby changing the voltage drop along the sample. This allows for the deduction of different electron transport effects in a two-dimensional Lorentz gas. The first three chapters outline fundamental concepts. The experimental results obtained in this work are presented in four further chapters:

Chapter 3 investigates two-dimensional high-density Lorentz gases comprising obstacles with the shape of retroreflective crosses. This shape favors the memory effect of “retroreflection.” The results are compared with prior works on two-dimensional Lorentz gases formed by circular obstacles. Both systems share a conductivity maximum in the magnetotransport caused by guided transport along the Lorentz gas contour. Only for retroreflecting Lorentz gases, an additional maximum occurs at low magnetic fields. This marks the breaking of retroreflection by the reduced cyclotron radius and is a signature of anomalous diffusion, which was confirmed through molecular dynamics simulations.

In Chapter 4, the influence of dynamic and static background scattering on the magnetotransport of circular Lorentz gases is investigated. At low magnetic fields, dynamic scattering caused by phonons increases the conductivity, whereas static scattering caused by a secondary Lorentz gas of reduced density and obstacle size decreases it. At elevated magnetic fields, the type of background scattering does not influence the conductivity modulation.

In Chapter 5, the magnetoresistance of the unstructured two-dimensional electron gas is investigated with regard to the "giant negative magnetoresistance". This consists of two maxima. According to recent publications, the inner maximum is explained by a dilute two-dimensional Lorentz gas formed by growth-related defects. This was confirmed by characterization of the magnetoresistance of low-density Lorentz gases.

Finally, Chapter 6 describes how two-dimensional Lorentz gases were brought out of equilibrium by different influences. In particular, it is shown that electromagnetic radiation in the terahertz spectrum causes acoustic phonon-induced resistance oscillations. Moreover, Hall- and microwave-induced resistance oscillations were measured on Lorentz gas samples.

CONTENTS

ABBREVIATIONS

2DEG	two-dimensional electron gas
2DLG	two-dimensional Lorentz gas
AD	antidot
AlGaAs	aluminum gallium arsenide
DOS	density of states
EBL	electron beam lithography
EWT	Ehrenfest wind-tree model
FIRO	far-infrared resistance oscillation
FWHM	full width at half maximum
GNMR	giant negative magnetoresistance
GaAs	gallium arsenide
GHz	gigahertz
HIRO	Hall-induced resistance oscillation
LL	Landau level
LG	Lorentz gas
MBE	molecular beam epitaxy
MD	molecular dynamic
MFP	mean free path
MIRO	microwave-induced resistance oscillation
MSD	mean squared displacement
OL	optical lithography
PIRO	phonon induced resistance oscillation
QHE	quantum Hall effect
RC	retroreflective cross
SEM	scanning electron microscopy
SdHo	Shubnikov-de Haas oscillations
THz	terahertz
WL	weak localization

CHAPTER 1

INTRODUCTION

A Lorentz gas is a system of electrons moving within a matrix of Poisson- distributed static obstacles, which are allowed to mutually overlap. Within this assembly of scattering centers, particles move freely and scatter specularly at the obstacles while not interacting with each other. In 1905, Hendrik Anton Lorentz provided this system for explaining the electron motion and heat conduction in metals. [1]

Because of its analogy to an ideal gas, it was later called the “Lorentz gas.” Since then, the Lorentz gas has offered a universal model for describing a variety of transport phenomena in nature.

Examples are pathogens moving in the blood stream of erythrocytes, such as trypanosomes, which cause sleeping sickness [2, 3], or proteins and lipids diffusing through cell membranes. [4] Different transport phenomena of heterogeneous media, such as anomalous diffusion, are explainable within this model. [5–10] Of high technological and fundamental scientific interest are porous electronic conductors, such as porous electrodes applicable for fuel cells [11, 12] or catalysis in electrochemistry. [13] Another example are randomly distributed defects within a conductor, which are unintentionally formed during the sample's growth process and provide scattering thereof. [14]

The occurrence of systems with noninteracting tracer particles moving within a plane of randomly distributed scattering centers is diverse and omnipresent in nature; however, the understanding of their transport properties is far from comprehensive. Investigations on two-dimensional Lorentz gases (2DLGs) promise an understanding of the universal character of the anomalous transport phenomena. Therefore, it is desirable to tailor essential properties like the density and shape of Lorentz gas obstacles on a model system that is accessible through experiments and simulations.

A system that offers this in experiments is achieved through the lateral patterning of a semiconductor heterostructure containing a 2D electron gas (2DEG), such as $\mathrm{GaAs/Al_xGa_{1-x}As}$, which provides high mobilities in the range of $\mu = 10^7\,\mathrm{Vs/m^2}$. [15] This corresponds to mean free paths of a few hundred μm, in which electrons are able to move ballistically within the 2DEG plane. The electrons do not influence each other. So-called “antidots” (Ads), lithographically defined and etched into the crystal plane, provide hard scattering centers. [16] A 2DLG is realized through a random distribution of ADs of equal size within a GaAs/$\mathrm{Al_xGa_{1-x}As}$ heterostructure. The electron transport is dominated by the 2DLG if the average distance of obstacles is smaller than the host structure’s intrinsic mean free path. [17]

At the same time, this system is implementable into classical molecular dynamics (MD) simulations, providing information of the electrons’ mean squared displacement (MSD). [15, 18] The combination of both approaches provides valuable insights into the transport properties of 2DLGs. Here, a magnetic field that is aligned perpendicular to the 2DLG bends the electrons’ trajectory on an orbit, where the cyclotron radius provides another characteristic length scale to the system. At the same time this system is implementable into classical molecular dynamics (MD) simulations, providing information of the electrons mean squared displacement (MSD).[15, 18] The combination of both approaches provides valuable insights into the transport properties of the 2DLG. Hereby a magnetic field, which is aligned perpendicular to the 2DLG bends the electron’s trajectory on an orbit, where the cyclotron radius provides another characteristic length scale to the system.

For 2DLGs with dilute obstacle densities, analytic descriptions exist that promote the concept of *memory effects*. [19] Such effects cause major deviations for transport observables such as magnetoresistivity $\rho_{xx}(B)$ and magnetoconductivity $\sigma_{xx}(B)$ compared with the Drude–Boltzmann model, where uncorrelated scattering in space and time is assumed. [20] Here, $\rho_{xx}(B)$ is predicted to be constant and independent of the magnetic field. Within the theories of 2DLGs, deviations from the Boltzmann model occur because of the obstacle’s static character, which causes memory effects. One prominent example is electrons that complete cyclotron orbits without being scattered and therefore do not contribute to the longitudinal conductivity. [19, 21, 22] Because this effect is more pronounced with an increased magnetic field, it generates an exponential decay in magnetoresistivity.

Other memory effects are repeated scattering at the same obstacles, which slightly modifies the above mentioned behavior, [19, 21, 23] and the memory effect of retroreflection, which causes a linear decay in magnetoresistivity close to $B = 0$. [24]

The objective of this thesis is to study different aspects of the transport properties of 2DLGs. The following four major questions are addressed, which are presented below along with an outline of the thesis.

***Question 1*:**

Does anomalous transport exist in retroreflecting 2DLGs, and are signatures of it distinguishable at low magnetic fields?

Chapter 3 is dedicated to investigations on 2DLGs formed by retroreflecting crosses. [25] These investigations are based on prior works [15, 26] on 2DLGs formed by circular obstacles. For both studies, the obstacle density was in the regime called “dense” (i.e., memory effects such as retroreflection contribute the magnetoconductivity to a non-negligible extent). For both scatterer shapes, a conductivity maximum occurs in magnetotransport, which is caused by a guided motion along the Lorentz gas contour. This magnetoconductivity maximum is found for magnetic fields at which the cyclotron radius corresponds to the average distance of the obstacles. In contrast to circular obstacles, the magnetotransport of a retroreflecting 2DLG exhibits an additional maximum at low magnetic fields. Not only does this mark the breaking of the system's retroreflectivity due to the reduced cyclotron radius, but it is also a signature of anomalous diffusion, which is shown through MD simulations.

The shape of retroreflecting crosses favors the backreflection between neighboring obstacles and assemblies of several obstacles on short time scales. This is one of the major properties of the Ehrenfest wind–tree model (EWT), [27] where a 2DLG is formed by square obstacles. For this special case of a 2DLG, it was proposed that the MSD does not grow linearly for low densities, but sublinearly. For these conditions, no diffusion constant can be defined. This anomalous behavior was confirmed in early computer simulations of the EWT. [28]

***Question 2*:**

How do dynamic and static background scattering modulate the magnetoresistivity / magnetoconductivity of a 2DLG compared with an undisturbed 2DLG?

In Chapter 4, the influence of dynamic and static background scattering on the magnetotransport of circular 2DLGs is investigated. [29] Static background scattering is caused by the implementation of a secondary 2DLG that has a lower dimensionless obstacle density and a smaller obstacle radius than the primary 2DLG. At low magnetic fields, dynamic scattering increases the conductivity, whereas static scattering reduces it. At increased magnetic fields, the type of background scattering does not influence the conductivity modulation but it changes sign after a certain magnetic-field threshold. These observations are explained by the influence of background scattering on retroreflection [16] and superdiffusive transport due to the $\vec{E} \times \vec{B}$-drift along the obstacle contour. [15, 30]

***Question 3*:**

How does a 2DLG modulate the giant negative magnetoresistance?

Chapter 5 of this thesis deals with 2DLGs with low obstacle densities. In terms of magnetoresistance, the unpatterned 2DEG of GaAs/$\mathrm{Al_xGa_{1-x}As}$ exhibits the characteristic shape of the *giant negative magnetoresistance*, which consists of two maxima centered around zero magnetic field. [14, 31–33] Two major approaches discussed in Chapter 3 are provided to explain this phenomenon: one is the hydrodynamic description [34] provided by Alekseev, where the electron transport is described in terms of a viscous fluid. The second approach is the interaction model [35] of Mirlin et al., which argues that the characteristic shape in magnetoresistance is based on long- and short-range potentials that interact with each other. In recent publications, the inner maximum has been interpreted to be caused by a 2DLG, comprising short-range strong scatterers (so-called *oval defects*), which form during the sample growth, generating the short-ranged potential of the interaction model.

[14, 32] This is proven using 2DLGs with low obstacle densities as well as through investigating their influence on both peaks with regard to different experimental conditions (in-plane magnetic fields, temperature, sample current, and sample width).
It was possible to correlate these experimental findings with different models from the literature and show the validity of each model within certain experimental conditions.

***Question 4*:**
Do non-equilibrium effects exist in the magnetoresistivity of 2DLGs, and how does the magnetic field interval in which they might occur correlate to the properties of 2DLGs?
Finally, the magnetoresistance of 2DLGs was investigated by bringing the system out of equilibrium. Nonequilibrium phenomena usually occur in 2DEG systems exposed to a magnetic field perpendicular to the 2DEG plane, when high DC currents are applied (Hall-induced resistance oscillations) or when the sample is exposed to irradiation (microwave-induced resistance oscillations) or temperature (phonon-induced resistance oscillations). One relevant study [17] provides a detailed review of recent advances in these magnetoresistance oscillations, which all share a $1/B$-periodicity caused by a similar mechanism. Any results in the literature are presented on pristine 2DEG systems. Here, we investigate different nonequilibrium phenomena on 2DLG samples and compare them with the respective unpatterned samples (which can also be interpreted as being dilute 2DLGs). This is motivated by Beltukov et al., [36] who suggested that microwave-induced resistance oscillations (MIRO) are caused by memory effects from scattering at randomly distributed sample defects. Therefore, the question arises of whether irradiation from the terahertz spectrum on the implemented scattering matrix of a 2DLG can lead to additional memory effects, which is based on the fact that the irradiation wavelength corresponds approximately to the averaged obstacle distance.
Additionally in this thesis, it is shown that electromagnetic terahertz irradiation causes acoustic phonon resistance oscillations (PIRO). No photon-induced $1/B$-periodic oscillations are found at harmonics of the cyclotron frequency. In the terahertz regime, PIRO dominate MIRO, and vice versa, the detection of PIRO in the gigahertz regime being caused by photon irradiation is absent.
Moreover, HIRO and MIRO are measured at 2DLGs, and for each case, reference measurements are performed on nonpatterned samples.

In each of the respective chapters, one major research question is addressed. The conclusion summarizes the main results of the work presented within this thesis. Finally, some open questions identified in this work are proposed.

CHAPTER 2

FUNDAMENTAL EXPERIMENTAL TECHNIQUES

2.1 Sample preparation and processing techniques

In subsection 2.3.1, the growth of the structure of 2DEG GaAs/AlGaAs using molecular beam epitaxy (MBE) is explained. Any sample with measurement results presented in this thesis was processed from a $(5 \times 5)\,\mathrm{mm}^2$ piece of the host material, which was grown by Klaus Pierz in the group of Hans Werner Schumacher at the *Physikalisch-Technische Bundesanstalt, Braunschweig.*

Two major lithography techniques were used for the sample processing: optical lithography (OL), which was used to define the Hall bar mesa and ohmic contacts, and electron beam lithography (EBL), which was employed for the Lorentz-gas obstacles. Both lithography techniques share the fact that the image of a mask is transferred to the sample surface with the contrast of resist to no resist. The major difference between the techniques is that OL uses photons as irradiation particles, whereas EBL uses electrons. The resolution of EBL is restricted by the de Broglie wavelength of the electron (a few nm at keV-acceleration) and imaging electron lenses, and thus it is suitable for patterning structures of a few nm such as Lorentz-gas obstacles, which are in the range of µm. The EBL performed on the samples discussed in this thesis was performed at the Centre national de la recherche scientifique by Dominique Mailly.

By contrast, OL is a fast, clean, and reliable tool for pattering large structures that do not demand resolution in the nm-range, but rather in the range of a few µm.

The GaAs/AlGaAs crystal $(5 \times 5)\,\mathrm{mm}^2$ hosts space for four samples, and thus all sample processing steps could be performed on four samples simultaneously. As a last step, the chip was broken into the four sample pieces such that each sample was introduced in its own chip carrier and measured in a separate cooldown.

Figure 2.1 presents an illustration of the respective sample processing steps.

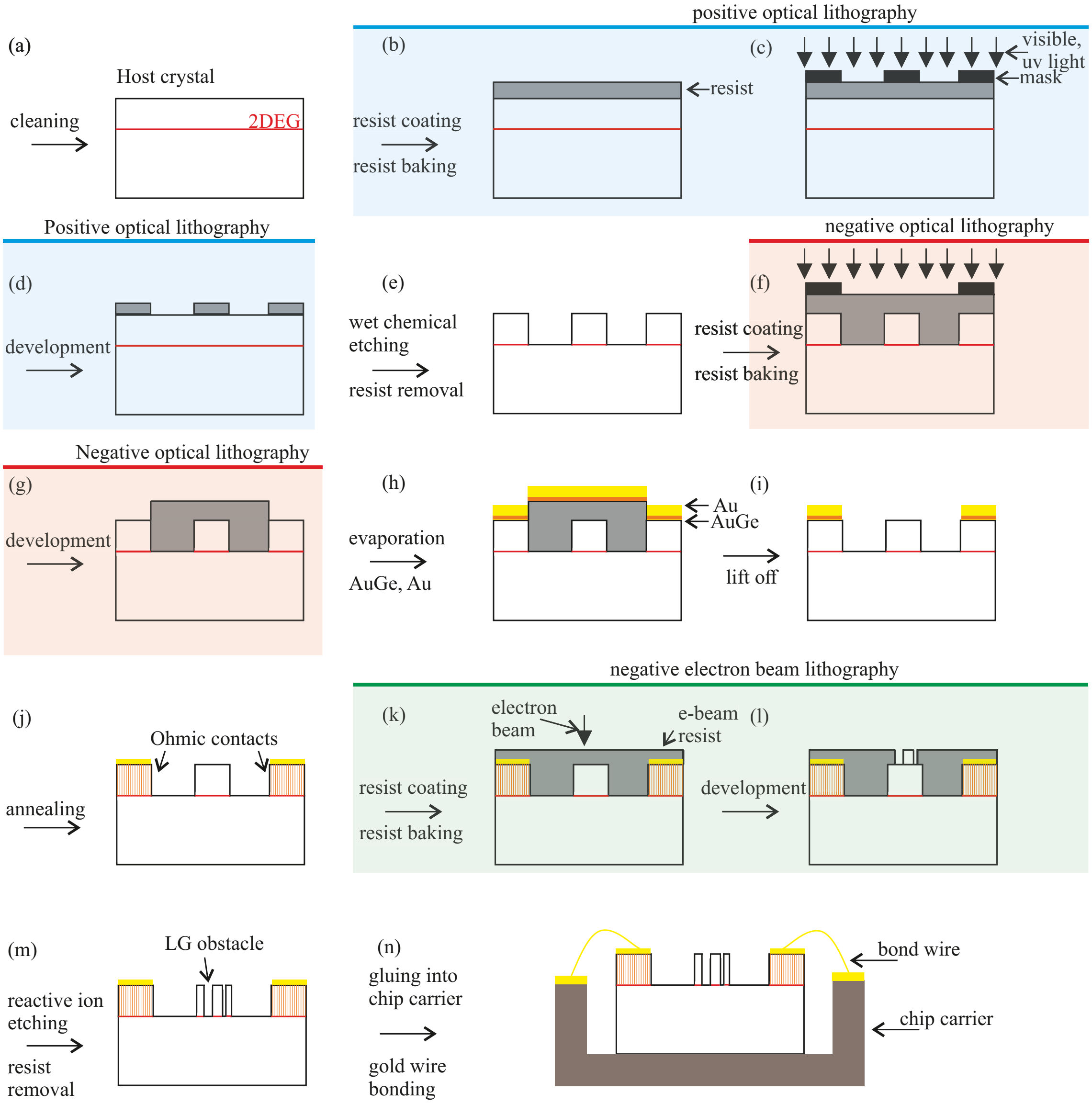

Figure 2.1: Schematic overview of the sample processing. The sample is shown as a cross-section. Steps (a)-(e) are performed to define the Hall bar mesa by employing positive OL and wet chemical etching. Negative OL (steps (f)-(g)) is used to define Ohmic contacts, which are realized through the evaporation of AuGe/Au (step (h)), lift off (step (i)) and annealing (step (j)). The LG fields are realized by EBL and reactive ion etching (steps (k)-(m)). Finally the sample is glued into a chip carrier; bond wires connect the Ohmic contacts with single gold pads of the chip carrier (step (n)).

Positive OL was used to transfer the Hall bar pattern from a chrome-covered glass mask to the resist-covered sample. In 2.1, these steps referring to positive OL are marked by the blue shaded interval. First, the sample (step (a)) was cleaned of any protective resist covering the surface by rinsing it in acetone, isopropanol, and deionized water, followed by a drying step of 60 s at 110 °C. The cleaned sample was then spin coated with photolithography resist (AZ 5214 E - microchemichals, 30 s, 5000 rpm) and dried for 40 s at 113 °C.

Irradiation from a mercury lamp is used to break the polymer chaining of the resist that is not covered by chrome such that these areas are soluble to the developer. The sample is exposed to the irradiation for 13 s (see step (c)). After the sample is rinsed for approximately 35 s in the developer (AZ-325 MIR, MicroChemicals), the positive OL is finished and the chrome-glass image of the mask is transferred to the sample.

Wet chemical etching removes layers of crystal in a controlled manner, which depletes the 2DEG in any area that is not part of the Hall bar. Therefore (step (e)), the sample is rinsed in a mixture of sulfuric acid (H_2SO_4), hydrogen peroxide (H_2O_2) and water (H_2O) at the ratio of $1:3:100$. The rate at which the material is etched away is approximately 1 nm/s, and thus the desired etch depth can be determined by the time the sample stays in the etching solution. To deplete the 2DEG, an etching time is chosen that corresponded with the 2DEG depth (150 nm). The parts of the sample covered with the resist were protected from the etching solution such that the Hall bar mesa is defined after step (e).

As the next processing step, Ohmic contacts are introduced to the sample by negative OL (steps (f)-(g), marked by the red shaded interval); evaporation of AuGe (150 nm) and Au (150 nm) (steps (h)-(i)); and annealing (step (j)). Negative OL is termed “negative” because the image of the mask is reversed; that is, any area covered with chrome corresponds to an area with no resist on the sample surface after the development (step (g)). Thus, it is possible to evaporate metals into the defined holes (step (h)). The resist below the metal layers is soluble in acetone and can thus be removed with the metal from the sample. After step (i), which is called “lift-off,” only areas of the sample are covered with metal where it had been evaporated directly onto the surface. The AuGe/Au on the GaAs forms a Schottky barrier. To electronically access the 2DEG with an Ohmic connection, the sample is heated for a few minutes in the inert atmosphere of a diffusion oven (90 s at 400 °C). The germanium diffuses to lower layers of the crystal, thereby doping the substrate such that an Ohmic contact is formed from the gold contact at the surface to the 150 nm deep 2DEG.

Through the EBL performed at the Centre national de la recherche scientifique (green shaded interval), the Lorentz gas arrays were patterned into the respective measurement field of the Hall bar (step (k)). Negative EBL is used, which means that any resist irradiated with electrons is more soluble to the developer because the accelerated electrons break the resist chains. Afterwards, the developing irradiated areas (which will become the LG obstacles) are free from resist (see step (l)). Subsequently (step (m)), the sample is exposed to the plasma of a reactive ion etching chamber such that the etching depth is as deep as the 2DEG.

Finally, the chip is broken into the four samples. Each of them was glued into a chip carrier (step (n)) that fitted into the cryostat sample holder. Bond wires connected the Ohmic contacts of the sample chip and the respective pads of the chip carrier, allowing the sample to be electronically accessed via the measurement connections outside of the cryostat.

2.2 Measurement setup

To reach mean free paths of tens of micrometers, the electron–phonon and electron–electron scattering processes caused by temperature must be reduced through cooling the sample. Therefore, two cryogenic setups were used for the work presented in this thesis. The first was a helium bath cryostat from Oxford Instruments, which offers a temperature interval of $T = 1.4\,\mathrm{K} - 300\,\mathrm{K}$, and then lower temperatures ($25\,\mathrm{mK} - 1\,\mathrm{K}$) were reached using a dilution refrigerator (*Leiden Cryogenics*). Both cryostats are equipped with superconducting solenoids, which also require temperatures of a few Kelvin to reach the regime of superconductivity [37]. Magnetic fields up to 12 T (dilution refrigerator) and 8 T (helium bath cryostat) are experimentally accessible.

Some physical effects depend on an additional magnetic field along the 2DEG plane. Both setups allow for this parameter through tilting the sample in the main magnetic field. The sample holder used in the helium bath cryostat is equipped with a mechanical rotator, allowing for steps of approximately 1°. The sample holder of the dilution refrigerator hosts a rotation stage mounted on a piezo-crystal, which has a precision better than 0.01°.

The helium bath cryostat has the following working principle: liquid helium (He^4) has at atmospheric pressure a temperature of 4.2 K. By pumping the He^4 from the cryostat's helium reservoir to the sample chamber the temperature can be reduced to 1.4 K. The two chambers are connected by a needle valve. The opening of this valve controls the helium gas flow such that the sample chamber temperature is tunable in between 1.4 K and 4.2 K. Additionally the temperature can be further increased (from 4.2 K to room temperature) and adjusted by heaters installed in the sample chamber. For a more detailed description of the cryogenic principle the reader is referred to [38, 39].

The closed cycle dilution refrigerator from *Leiden Cryogenics* features two separated cooling circles, which are both closed to ensure that no helium gas is lost during use. A pulse tube cooler pre-cools the inner He^3 - He^4. Both isotopes are mixed in the mixing chamber. Different to bosonic He^4, He^3 is a Fermi gas and thus the miscibility of both isotopes is restricted. As the system pursues reaching a state of the lowest energy possible, the increase in Fermi energy is higher than the energetic gain from the two isotopes of helium being mixed. Consequently, a pure He^3 phase is formed on top of a mixed phase. The He^3 evaporates at a lower pressure compared with the He^4, thereby realizing a constant flow of He^3 across the mixing chamber. This leads to evaporative cooling of the mixture, which theoretically is not limited. Experimentally, the cooling power of the system and external heat leaks lead to a finite minimal temperature, which for the cryostat used in this study is 25 mK. For the original description of He^3-He^4 cooling, the reader may refer to [40], and a detailed overview is given in [41].

The measurement principle, of which Fig. 2.2 is an illustration, is based on the four terminal geometry and is the same for both cryostats. A small, low frequency (17 Hz) AC-current in the range of 100 nA to 500 nA is passed from the sample's source to the drain contact. Therefore, a resistor with a resistance much larger (usually 10 MΩ) than the sample resistance (in the range of a few Ohms) and an AC-voltage source are connected in series.

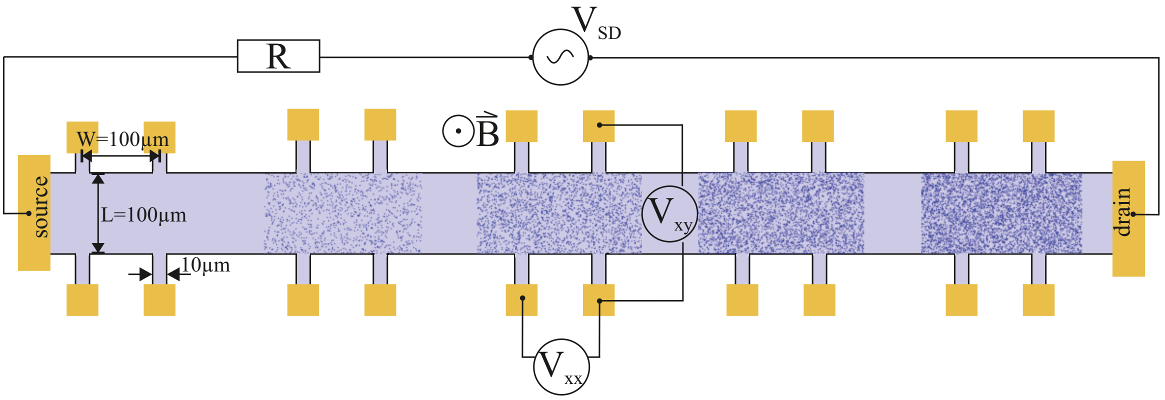

Figure 2.2: The typical Hall bar geometry of the samples used in this study. An AC-voltage source and a resistor (in the range of 10 MΩ) in front of the sample are used to apply an AC current from the source to the drain contact. The voltage drop V_{xx} and V_{xy} can be measured using the lock-in technique.

By picking up the voltage at two probes, which are separated by the 2DEG structure of interest, it is possible to measure the resistance from just this area. Any contributions from the wire resistance, filters, or Ohmic contacts are not recorded using four contacts, which is different to applying the current and reading the voltage from two contacts. Low noise signals, even under the noise level, can be measured using the lock-in technique. The AC-voltage drop at two probes is therefore mixed with the AC signal used for the source-drain current. After a low pass filter of the two mixed signals, it is possible to detect the voltage drop phase and frequency sensitive. Furthermore, from the phase information, it is possible to distinguish ohmic contributions, which are in phase with the reference signal, and nonohmic contributions, which are out of phase with the reference signal.

The voltage drop along two voltage probes can be measured either along the sample or perpendicular to the current direction. In Fig. 2.2, a Hall bar with five measurements fields is shown, with four hosting a Lorentz gas (with increasing obstacle density from left to right). Exemplary the voltage measurement in the longitudinal direction V_{xx} and the perpendicular direction V_{xy} of the second Lorentz gas field is shown. The resistance R is directly proportional to the resistivity ρ of the respective measurement field:

$$R_{\mathrm{xx}} = \frac{V_{\mathrm{xx}}}{I_{\mathrm{SD}}} = \rho_{\mathrm{xx}}\frac{L}{W}; \qquad R_{\mathrm{xy}} = \frac{V_{\mathrm{xy}}}{I_{\mathrm{SD}}} = \rho_{\mathrm{xy}}\frac{L}{W} \tag{2.2.0.1}$$

L is the length in between the voltage probes and W the Hall bar width. A magnetoresistivity trace can be obtained by recording the voltage drop in between the respective voltage probes of interest and recording the magnetic field. The magnetoconductivity can be calculated from ρ_{xx} and ρ_{xy} using

$$\sigma_{\mathrm{xx}} = \frac{\rho_{\mathrm{xx}}}{\rho_{\mathrm{xx}}^2 + \rho_{\mathrm{xy}}^2} \tag{2.2.0.2}$$

The abovementioned measurement setup was used to obtain the magnetoresistivity and magnetoconductivity of two-dimensional (2D) dense retroreflective Lorentz gases (Chapter 4), 2D bimodal Lorentz gases (Chapter 5), and the 2DLG samples with a low obstacle density (Chapter 6).

The measurement setup for the experiments of the 2DEG samples out of equilibrium (Chapter 7) was performed using high Hall electric fields, electromagnetic irradiation, or temperature with slight modifications, as described in the corresponding chapter.

2.3 Two-dimensional electron gas

A 2DEG is a system in which the electrons' movement is confined in one dimension. Free movement in the other two directions is possible. Many examples of how 2DEGs can be realized exist, and some are described as follows.

One example is the formation of a 2DEG at the surface of liquid helium caused by surface states [42], [43]. Metal-oxide-semiconductor field-effect transistors, which are common in daily life, host a 2DEG where the confinement to a thin layer is caused by the attracting potential of a gate voltage and an oxide layer [44]. Graphene is a 2D material composed of one carbon monolayer (i.e., its conduction is two dimensional) [45]. A general review of 2DEGs in condensed matter was presented in [46]. In recent years, topological insulators have received increasing scientific attention. At their surface and corners exist protected states, which enable 2D electron transport. [47]

Another way to realize the confinement in one direction is by combining the interfaces of III-V or II-VI compound semiconductors. Here, one of the most prominent experimental implementations of a 2DEG is formed at the boundary of the III-V semiconductors of GaAs and $\mathrm{Al_xGa_{1-x}As}$ (x is the ratio of Al atoms replacing Ga).

In addition to the well-established processing techniques, this material offers mobilities reaching $\mu \leq 10^7 \mathrm{cm^2/(Vs)}$, thereby providing by far the most disorder-free 2D material known today [48]. In the following subsection, the formation of the 2DEG is explained using this prominent example, which is the host material of any sample used within this thesis.

2.3.1 2DEG formed at the GaAs/AlGaAs interface

The crystal growth of the $\mathrm{GaAs/Al_xGa_{1-x}As}$ heterostructure can be realized by means of molecular bean epitaxy (MBE), where the materials are deposited on a heated substrate in an ultra-high vacuum. MBE allows the exact atomic composition to be controlled along the crystal growth direction (z-direction) monolayer by monolayer. [48] To grow a 2DEG, the band-bending at the interface of GaAs and $\mathrm{Al_xGa_{1-x}As}$ can be designed as follows:

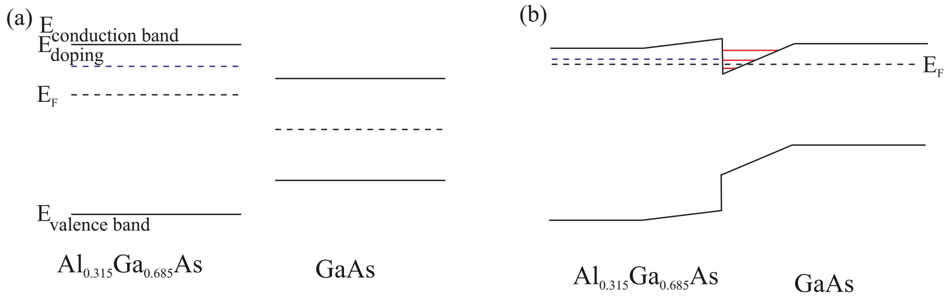

Figure 2.3: (a) Schematic band diagram of the n-doped $Al_{0.315}Ga_{0.685}As$ and undoped GaAs. (b) After the materials are brought into contact, the conduction band bends such that E_F is aligned along the whole crystal, which leads to the formation of a triangular potential well. Figure adapted from [26].

The bandgap of GaAs amounts to 1.42 eV and lies completely within that of AlAs (2.16 eV). Depending on the amount of x in the $Al_xGa_{1-x}As$, its bandgap can be tuned between those of GaAs and AlAs. The different heights in the conduction band bottom of the two materials is called the band offset. For the typical choice of x = 0.3, the band offset amounts to 300 meV between the higher conduction band of $Al_{0.3}Ga_{0.7}As$ and the lower one of GaAs. [49] After both materials are brought into contact, the chemical potential aligns throughout the whole crystal. This leads to a bending of the conduction band because the two materials are grown directly on top of each other, resulting in a triangular potential well (see Fig. 2.3). Because the length of this triangular potential along the z-direction is comparable to the electron Fermi wavelength λ_F, the electrons' density of state discretizes quantum-mechanically into sub-bands. If the crystal growth is tuned such that only the first sub-band is energetically lower than the Fermi energy, the electrons are confined along the z-direction and only able to move in the x-y plane. Thus, at the interface of GaAs and $Al_xGa_{1-x}As$, the 2DEG is formed. Additionally, n-dopants (e.g. silicon) can be introduced in the growth of $Al_xGa_{1-x}As$ at a distance d higher than the 2DEG position. This will lead to an increase of the electron density n_e as well as a higher mobility μ. This technique is called modulation doping [50], and has the advantage of reducing the scattering of electrons at ionized donors through spatial separation by the distance d. Because of the spatial separation between the 2DEG and the dopants, the electrons are only weakly scattered, and high mobilities in the order of $10^6\,\mathrm{cm}^2/(\mathrm{Vs})$ are reached.

AlAs and GaAs exhibit the Zincblende structure with lattice constants of a(GaAs) = 565 pm and a(GaAs) = 562 pm. [51] Because of this almost negligible variation in a (less than 1 %), the strain at the interface of the crystals is rather a minor scattering contribution. These high mobilities are one reason why the heterostructure of GaAs/$Al_xGa_{1-x}As$ is the workhorse for many fundamental experiments.

Every measurement result discussed within this thesis was obtained from a sample that was processed from a 2DEG GaAs/$Al_xGa_{1-x}As$ heterostructure. The 2DEG heterostructures H012 used in the experiments were grown by Klaus Pierz at the *Physikalisch-Technische Bundesanstalt (Braunschweig)* in the group of Hans Werner Schumacher. The same host material as that described in [26] was used. Fig. 2.4 (a) is a qualitative sketch of the growth sequence of $H012$. The All ratio of the $H012$ structure was chosen to be x = 0.315. The left-hand side provides the energetic potential of the conduction band with respect to the z-coordinate. At a depth of approximately 150 nm, the electron's motion is confined along z by the triangular potential well formed by the band offset formed at the GaAs/Al$_x$Ga$_{1-x}$As interface. A zoom-in of the potential well is shown in the upper right corner of Fig. 2.4 (b). The growth is designed such that only the lowest level of the potential well lies energetically lower than E_F, meaning that only this sub-band is occupied.

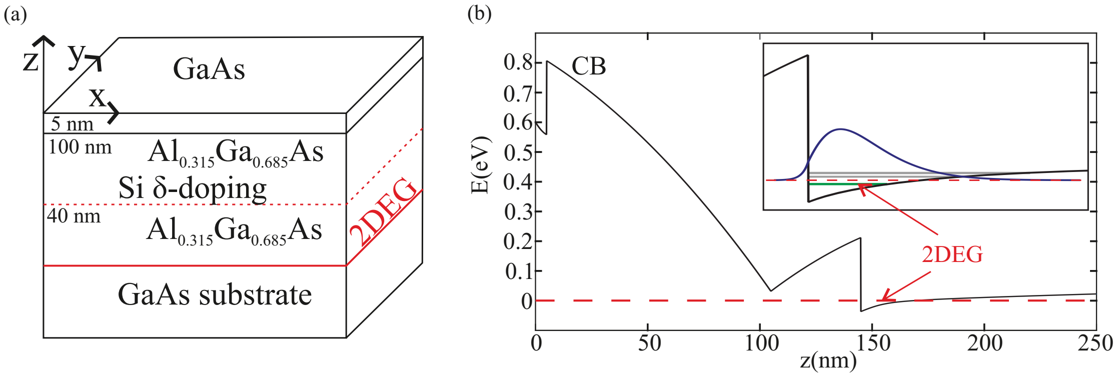

Figure 2.4: (a) Schematic growth sequence of the host material $H012$ used within this thesis. The 2DEG is formed approximately 150 nm below the surface. (b) Calculated conduction band at the bottom of the heterostructure depicted in (a). Figure adapted from [26].

CHAPTER 3

FUNDAMENTAL CONCEPTS: THEORY

3.1 The Drude model

In 1900, Paul Drude formulated a classical model of diffusive electron transport in metals and solids [20]. Therefore, reasonable assumptions starting from the Boltzmann equation [52] are applied. The Boltzmann equation describes the thermodynamic behavior of colliding particles, forming a system that is out of equilibrium. The general nonsimplified Boltzmann equation is a nontrivial, nonlinear, integro-differential equation describing the multidimensional phase space.

Later, the Drude model was extended by H. A. Lorentz in 1905. [1] It is a completely classical description of diffusive electron transport and was later supplemented with the results from quantum theory, resulting in the Drude-Sommerfeld model. [53]

Nevertheless, the Drude model connects the microscopic behavior of electrons in a metal with measurable experimental quantities such as resistivity and capacity, and offers reasonable values at low magnetic fields.

Within the Drude-Boltzmann model, one assumes that every collision of an electron with a scattering center is random. As a descriptive picture, one could say the electron does not have memory. Every scattering event is uncorrelated to the next one as well as each particle collision. There are many examples of scattering in electron transport, such as scattering at lattice imperfections, at lattice vibrations (phonons), at other electrons, or at interface roughness. All scattering rates can be summed up in the Drude scattering time τ.

Applying a small external electric field $\vec{E}$ to a metal will lead to a constant current density $\vec{j}$. This is the well-known Ohm's law. The proportionality constant is the conductivity $\underline{\sigma}$:

$$\vec{j} = \underline{\sigma}\,\vec{E} \tag{3.1.0.1}$$

where $\underline{\sigma}$ is a tensor describing the electron transport in three dimensions and considers any microscopic scattering process. These give rise to a Stokes-type frictional force $\vec{F}_{\text{friction}}$ friction. These scattering processes cause the electrical resistivity $\underline{\rho} = 1/\underline{\sigma}$. τ quantifies the average time in between scattering events of an electron that travels the mean free path $l_{\text{mfp}} = v_F \cdot \tau$, with v_F being the Fermi velocity. With an external electric field $\vec{E}$ applied to a metal, an electron will follow the external force $\vec{F}_{\text{el}} = -\vec{E} \cdot e$. Here, the elementary charge $e = 1.602 \cdot 10^{-19}\,\text{C}$ is defined as positive. $\vec{E}$ accelerates the electrons, which simultaneously experience scattering, causing a frictional force $\vec{F}_{\text{friction}}$ friction that is the second term of the classical equation of motion:

$$m^* \frac{d^2\vec{r}}{dt^2} + \frac{m^*}{\tau}\left(\frac{d\vec{r}}{dt}\right) = -e\vec{E} \tag{3.1.0.2}$$

where $\vec{r}$ is the position of the electron; t is the time; and m^* is the effective mass. Within the effective mass approximation, the net effect of the crystal periodic potential on the motion of an electron is taken into account by changing the value of the electron's mass from the value of free space $m_e = 9.11 \cdot 10^{-31}\,\text{kg}$ to m^*, which for $m^* = 0.067 \cdot m_e$. [54] This model allows the motion of one electron to be described using the classical equation of motion 3.1.0.2. Since the model of the effective mass is deduced from a quantum mechanical approach, this description is called *semiclassical.*
Applying an electric field $\vec{E}$ to the sample will accelerate charge carriers in the conductor. At the same time, this will cause an increase of $\vec{F}_{\text{friction}} = \frac{m^*}{\tau}\left(\frac{d\vec{r}}{dt}\right)$ until the system reaches a steady state; that is, charge carriers are not accelerated but maintain a constant velocity, which is the drift velocity $\vec{v}_d$. With $m^* \frac{d^2\vec{r}}{dt^2} = 0$ at the steady state, one finds the following for $\vec{v}_d$:

$$\vec{v}_d = \frac{d\vec{r}}{dt} = -\frac{e\vec{E}\tau}{m^*} \tag{3.1.0.3}$$

The current density $\vec{j}$ is proportional to $\vec{v}_d$ via: $\vec{j} = en_e\vec{v}_d$; and n_e is the electron density. From this and (3.1.0.3) follows the zero-field conductivity:

$$\sigma_0 = \frac{n_e e^2 \tau}{m^2} \tag{3.1.0.4}$$

In the next section, the influence of an additional perpendicular magnetic field on the magnetoconductivity tensor $\underline{\sigma}$ is discussed with regard to the different components.

3.2 Magnetotransport: 2DEG in a perpendicular magnetic field

3.2.1 Low perpendicular magnetic fields

For perpendicular magnetic fields that are weak, in that the cyclotron frequency $\omega_c = eB/m^*$ is smaller than the scattering rate $1/\tau$, a description using the classical equation of motion 3.1.0.2 with an additional Lorentz contribution is justified. This criterion means an electron will be scattered more than one time before one cyclotron orbit is fulfilled. Once a small magnetic field $\vec{B}$ is applied additionally to $\vec{E}$, the equation of motion 3.1.0.2 must be supplemented with the Lorentz force:

$$m^* \frac{d^2\vec{r}}{dt^2} + \frac{m^*}{\tau}\frac{d\vec{r}}{dt} = -e\left(\vec{E} + \frac{d\vec{r}}{dt} \times \vec{B}\right) \tag{3.2.1.1}$$

Under the steady state conditions $\vec{v}_d = \text{const.}$ and the electron is not further accelerated i.e. $d^2\vec{r}/dt^2 = 0$. Thus, 3.2.1.1 reduces with $\vec{j} = -n_e e \vec{v}_d$ to

$$\vec{j} = \frac{n_e e^2 \tau}{m^*}\left(\vec{E} + \vec{v}_d \times \vec{B}\right) \tag{3.2.1.2}$$

The magnetic field is usually designed such that it is applied along the z-direction (i.e. $\vec{B} = B\vec{e}_z$) . The Lorentz equation 3.2.1.2 may be split along the three spatial coordinates with $\sigma_0 = n_e e^2 \tau / m^*$. Solving this system of three equation leads to the magnetoconductivity tensor, for which $\vec{j} = \underline{\sigma}\vec{E}$ holds:

$$\underline{\sigma} = \frac{\sigma_0}{1+\omega_c^2\tau^2}\begin{pmatrix} 1 & -\omega_c\tau & 0 \\ \omega_c\tau & 1 & 0 \\ 0 & 0 & 1+\omega_c^2\tau^2 \end{pmatrix} \tag{3.2.1.3}$$

Within this thesis, only 2D conductivity is considered because the motion in the z-direction is prohibited by the potential confinement. The tensor inversion of the conductivity leads to the resistivity: $\underline{\rho} = 1/\underline{\sigma}$. From this, the resistivity tensor in two dimensions is as follows:

$$\underline{\rho} = \begin{pmatrix} 1/\sigma_0 & -B/(n_e e) \\ B/(n_e e) & 1/\sigma_0 \end{pmatrix} \tag{3.2.1.4}$$

Noticeably the ρ_{xx} and ρ_{yy} do not depend on B. The off-diagonal elements of $\underline{\rho}$ i.e. ρ_{xy} and ρ_{yx} are directly proportional to B. The slope of this linear characteristic is the Hall coefficient $R_H = 1/(n_e e)$. Fig. 3.1 depicts the magnetoconductivity (a) and resistivity tensor (b) along the xx and xy directions.

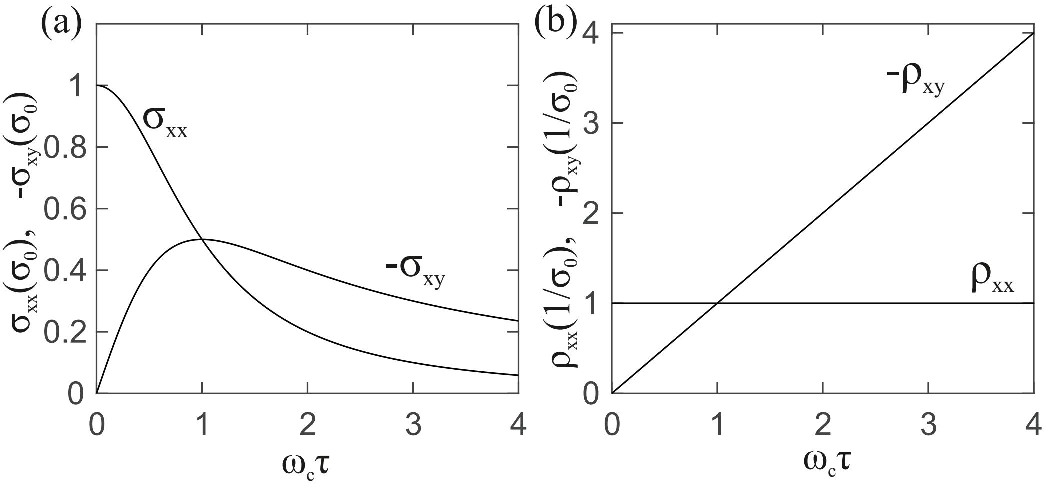

Figure 3.1: (a) Magnetoconductivity derived from the Drude model in units of zero-field conductivity σ_0 versus $\omega_c\tau$. (b) The same representation but for the magnetoresistivity. Figure from [49].

The main assumption in the deduction of the magnetoconductivity tensor is that the scattering events are of non-Markovian nature. Once this is changed e.g. by means of a two dimensional Lorentz gas one will observe differences to the described behavior (see Section 3.3).

3.2.2 Quantizing magnetic fields

3.2.2.1 The density of states in quantizing magnetic fields

At sufficiently high magnetic fields, the product $\omega_c\tau$ will be much larger than unity. In a descriptive picture, this means the electron fulfills more than one cyclotron orbit without being scattered. Consequently, quantum mechanical effects will change the magnetotransport properties and the concept of the Drude-Boltzmann model will not hold in this regime any more. As depicted in Fig. 3.2 (a), the density of states (DOS) in two dimensions is independent of the energy and constant as long as no magnetic field is applied:

$$D(E) = \frac{m^*}{\pi\hbar^2} \tag{3.2.2.1}$$

where m^* denotes the effective mass. Consequently, the Fermi energy E_F is directly proportional to the electron density n_e:

$$E_F = \frac{\pi\hbar^2}{m^*} n_e \tag{3.2.2.2}$$

The Hamiltonian of a system with confinement in the z-direction is as follows:

$$H = \frac{\hbar^2(k_x^2 + k_y^2)}{2m^*} + E_0 \tag{3.2.2.3}$$

An external magnetic field is considered using the Peierls substitution. [55] Additional electrostatic potentials $\Phi(x,y)$ are additively included into the Hamiltonian by applying the superposition principle, which defines the system's Schrödinger equation:

$$\left[\frac{(\vec{p}+e\vec{A})^2}{2m^*}+\Phi(x,y)+E_0\right]\Psi(\vec{r})=E\Psi(\vec{r}) \tag{3.2.2.4}$$

where $\vec{A}$ is the magnetic vector potential, $\vec{p}$ the electron's momentum, and $\Psi(\vec{r})$ is the electron's wavefunction. The vector potential, which satisfies $\vec{B}=\vec{\nabla}\times\vec{A}$, can be chosen by the Landau gauge, for example, as follows: $\vec{A}=(-By,0,0)$. Solving equation 3.2.2.4 conveys that the electron's energy is discretized by means of the quantum mechanical oscillator:

$$E_j=\hbar\omega_c\left(j-\frac{1}{2}\right) \tag{3.2.2.5}$$

where j is an integer starting from 0 that counts the eigenvalues of the system. The DOS is discretized from a constant to a series of δ-peaks, which are the Landau levels (LL). [56]

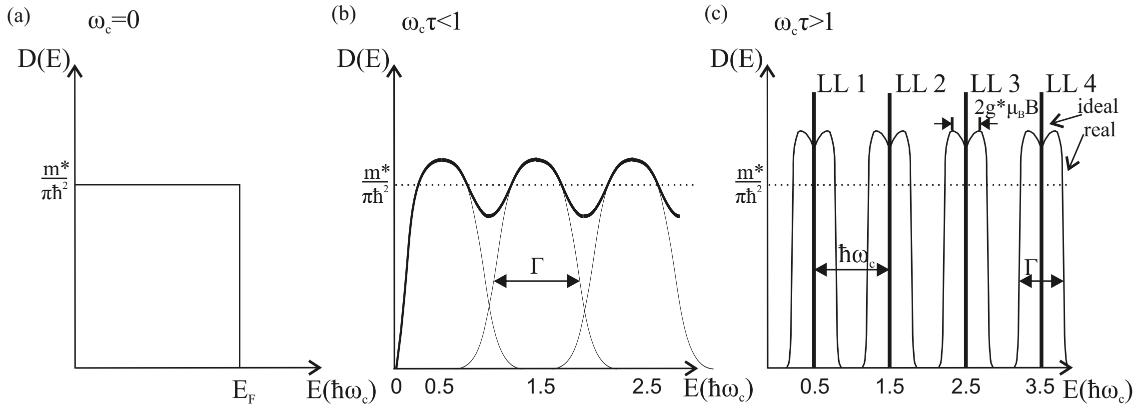

Figure 3.2: (a) The DOS of a 2DEG at zero magnetic field. (b) At intermediate magnetic fields the Landau-quantization modulates the DOS, while neighboring LLs with a full width at half maximum of Γ still overlap. (c) At high magnetic fields the middle of adjacent LLs are separated by $\hbar\omega_c$. Zeeman splitting separates the spin-up and -down state of the electron distribution of each LL.

Figure 3.2 (c) illustrates the DOS at magnetic fields for which $\omega_c\tau>1$ holds. Adjacent LL are energetically separated by $\hbar\omega_c$. Each LL is degenerated and the applied magnetic field will lead to Zeeman splitting of the spin-up and -down population. For each LL, the two spin states are separated by an energy value of $E_Z=2g^*\mu_B|\vec{B}|$, where μ_B is the Bohr magneton and g^* is the Landé-factor, which deviates for GaAs strongly from the free electron g-factor of $g_0=+2.0023$ because of the spin-orbit interaction, and $g^*(\mathrm{GaAs})=0.44$. [57] In real samples, the disorder, which is always present in the host crystal, causes a certain full width at half maximum (FWHM) Γ of each LL, which may be further

increased by temperature. At temperatures in the mK-range, the width Γ is determined by the quantum scattering time τ_q: $\Gamma = \hbar/(2\tau_q)$.
The low magnetic field regime is characterized by $\hbar\omega_c > \Gamma$ such that adjacent LL overlap. This is why within this regime no Shubnikov–de Haas oscillations (SdHos) or plateaus that form in the Hall-resistivity are measurable and the magnetoresistivity obeys the Drude-Boltzmann description. The essence of SdHos and quantum Hall plateaus is the discretization of the DOS with increasing magnetic fields, which is discussed in the following subsection.

3.2.2.2 Quantum Hall Effect and Shubnikov-de Haas Oscillations

As the regime of low temperatures and sufficiently high magnetic fields is reached (i.e., $\omega_c\tau \gg 1$), SdHos, which are $1/B$ periodic, are experimentally observed in the magnetoresistance. Increasing the magnetic field to approximately 1 T causes the minima evolve to into zero resistance states. Because the LL spacing is such that E_F lies between a lower filled and the next higher unfilled LL, no electron states are available to carry the current such that the conductivity of the system vanishes. As σ_{xx} and ρ_{xx} are connected through tensor inversion, this leads to zero resistance states in the longitudinal resistivity. The number of filled LL below E_F is called the filling factor ν. The inset of Fig. 3.3 depicts the DOS with a 2DEG system at filling factor $\nu = 4$. At this magnetic field of approximately 6.5 T, ρ_{xx} is in a zero-resistance state.
As the magnetic field is increased and the DOS changes such that E_F lies within an LL, charge transport is possible because free states are available. Thus, the longitudinal resistivity changes from the zero resistance state to a finite value. The system is periodically changed from a metal to an insulator depending on the LL spacing with respect to E_F as the magnetic field is increased. This was observed for the first time in 1930 by L. Shubnikov and W. J. de Haas in bismuth crystals. [58] At high magnetic fields, the minima of SdHos evolve into zero-resistance states.
Whenever the resistivity in the direction along the sample $\rho_{xx}$is minimal, ρ_{xy} forms a plateau and deviates from linear Hall resistivity. With no current-carrying state available, electrons are not able to move along the sample such that the Hall voltage saturates. In the spin-resolved case, ρ_{xy} exhibits plateau regions at integer filling factors ν following the characteristic:

$$\rho_{xy} = \frac{h}{e^2\nu} \tag{3.2.2.6}$$

In 1980, Von Klitzing et al. [59] discovered the quantization of ρ_{xy} in a 2DEG formed in a silicon metal-oxide-semiconductor (MOS) structure in multiple integers of h/e^2. This phenomenon is called the quantum Hall effect (QHE). In 1982, Tsui et al. [60] found ρ_{xy} to be quantized with fractions of h/e^2 at higher magnetic fields, which is known as the fractional QHE.

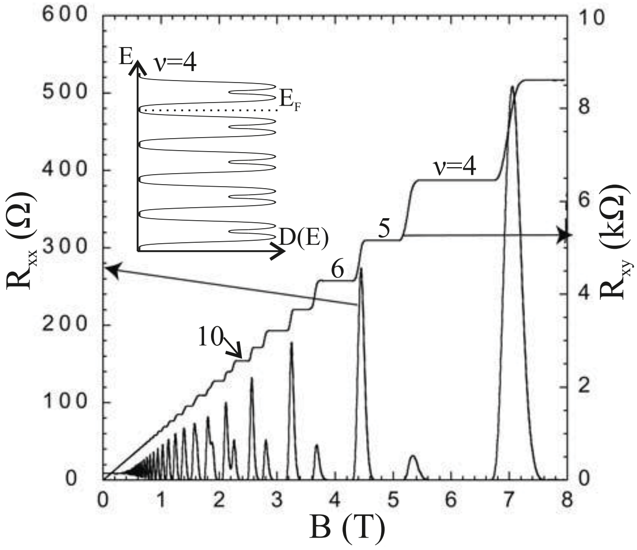

Figure 3.3: Measurement of the Hall effect (right axis) and Shubnikov–de Haas oscillations (left axis). The number of filled LL below E_F decreases as the magnetic field is increased, causing ρ_{xx} to oscillate with $1/B$. At elevated magnetic fields, ρ_{xx} exhibits zero-resistance states. At these positions, ρ_{xy} forms quantum Hall plateaus. The main figure is taken from [49].

3.2.3 Analysis of the Shubnikov-de Haas oscillations

According to the analysis of the SdHos, several transport properties can be determined, such as the electron density n_e , the quantum scattering time τ_q, or the electron mass m^*. In 1974, Ando formulated a model for describing SdHos analytically. At small and intermediate fields ($\omega_c\tau < 1$, see Fig. 3.2) the quantum Hall effect is weak but ρ_{xx} oscillates with $1/B$. Zero-resistance states are not yet evolved, although the DOS is weakly modulated by the Landau quantization. Ando found an analytic expression for $\rho_{xx}(B)$:

(3.2.3.1) $$\rho_{xx}(B) = \rho_{xx}(0)\left[1 - 4\cos\left(\frac{\pi\hbar n_e}{eB}\right) D(m^*, T) E(m^*, \tau_q)\right]$$

Equation 3.2.3.1 is called the Ando formula. By means of the argument of the cosine function the $1/B$ periodicity of the SdHo is exploited. The position of E_F as well influences the periodicity which is introduced by means of the electron density n_e in the cosine argument. $D(m^*, T)$ is the Dingle term, which depends on the electron temperature T. The crystal potential is considered by means of the effective electron mass m^*:

(3.2.3.2) $$D(m^*, T) = \frac{x}{\sinh(x)}, \quad x = \frac{2\pi^2 k_B}{\hbar e B} m^* T$$

The third contribution $E(m^*, \tau_q)$ influencing the amplitude of the SdHos is the exponential term:

$$E(m^*, \tau_q) = \exp\left(-\frac{\pi}{\omega_c \tau_q}\right)$$

where τ_q is the quantum scattering time. This is a time that characterizes any small angle scattering event within the electron transport.

The Ando formula thus offers the opportunity to determine the electron density n_e by analyzing the periodicity of $\rho_{xx}(B)$ in a $1/B$ representation. From the amplitude one is able to determine τ_q if the other parameters (i.e., m^* and T) are known. For an unknown system, m^* may be determined by varying the sample temperature T. For a further description of the analysis, referred to [49].

3.2.4 Length scales of electron transport: Different regimes

One characteristic length scale for an electronic device is the mean free path l_{mfp} that an electron is able to cover on average without being scattered. The ratio of l_{mfp} to the sample dimensions W and L provides a hint to which kind of electron transport dominates the resistivity. One way to increase l_{mfp} is to decrease the sample temperature. This decreases the phonon contribution to the scattering processes.

A conventional electronic device exhibits the property of l_{mfp} as being much smaller than any sample dimension. Thus, its electron transport is diffusive and incoherent, and does not show size quantization or spin effects.

The regime of mesoscopic electronic transport is reached if $l_{\text{mfp}} \approx L \approx W$. Within this regime, many phenomena that average out in the diffusive regime are observable.

Additionally, intrinsic lattice defects, imperfections, or interface roughness contribute to the scattering rate, which motivates research in the field of sample growth (see Subsection 2.3.1) to reach the mesoscopic regime of electron transport. Advancement in MBE growth enables mean free paths in the mm range at sub-Kelvin temperatures. Thus, the number of scattering events that occur between two voltage probes (distance in the range of 100 µm) is small and the mesoscopic regime is experimentally realizable.

Any effect of the mesoscopic regime that is explainable by classical collisions is called a ballistic effect. One example of a ballistic effect is the wire peak (see Subsection 3.2.5).

Another quantum mechanical effect that becomes measurable within the mesoscopic regime is size quantization. This effect may be reached by decreasing one sample dimension to the range of the electron's de Broglie wavelength $\lambda_F = h/\sqrt{2m^* E_F}$. For example, the confinement of electrons within the samples' z-directions is used to create a 2DEG (see Subsection 2.3.1). Confinement in another direction leads to the formation of quantum wires. [61]

Another characteristic parameter of a mesoscopic sample is the phase coherence length l_Φ, which is a measure of the average distance at which interference effects of partial electron waves can occur. For interference effects to be possible, l_Φ must exceed the Drude electron scattering length l_{mfp}. One example of an interference effect is weak localization. [62, 63]

The hydrodynamic regime was introduced by Alekseev [34]. Here, the mean free path of electron–electron collisions l_{ee} is the parameter that determines the occurrence of hydrodynamic effects and must be comparable to or greater than W. Electron–electron scattering is highly enhanced at the sample edges, such that the flow of electrons along the sample is comparable to the Poisson flow of a viscous fluid.

For any effect mentioned in this subsection, an applied magnetic field changes the measured magnetoresistivity by introducing another length scale through the cyclotron radius or a magnetic phase.

3.2.5 Diffusive boundary scattering (wire-peak)

The diffusive scattering of electrons at the walls of a Hall bar can make a major contribution to the magnetoresistance around zero magnetic field. This effect was first observed by Thornton et al. [64]. Within a ballistic quantum wire, a small contribution of diffusive scattering at the Hall bar boundaries leads to a peak that satisfies the following:

$$\frac{WeB_{\max}}{\hbar k_F} = \frac{W}{r_c} = 0.55 \tag{3.2.5.1}$$

where W is the Hall bar width, $B_{\max}$ is the position of the magnetoresistance peak, k_F is the Fermi wave vector, and r_c is the cyclotron radius, respectively. By means of an applied perpendicular magnetic field, the electron-wall scattering can be tuned.

At low fields, the trajectories do not differ much from the zero field case. Thus, in this regime the conductivity is dominated by scattering within the bulk Hall bar (case I in Fig. 3.4 (a)).

Another case is given at higher magnetic fields when the cyclotron orbit is smaller than the distance of two opposite Hall bar walls. An electron that is diffusively scattered along one wall is only able to reach the opposite wall through internal collisions. In this magnetic field regime, the overall conductivity is also dominated by scattering within the bulk of the Hall bar (case III in Fig. 3.4).

In between these two magnetic field regimes, there is an anomaly caused as follows. An electron exhibits a cyclotron radius of $r \approx 0.55\,W$ while its scattering at the Hall bar wall is mainly diffusive. This causes the trajectory to bend to the opposite Hall bar wall, thereby changing its direction of propagation. In Fig. 3.4 (a) (case II), such an event is depicted by the black trajectory, and opposite is a case of complete specular scattering along the sample rim, which is depicted by the red dotted line.

At magnetic fields that cause $W > r_c$, a diffusive scattering event does not change the direction of propagation (see the black trajectory in Fig. 3.4 (b)).

In the second case, the longitudinal resistance is increased at magnetic fields that fulfill $B_{\max} = 0.55 \cdot \hbar k_F/(We)$, as can be observed in the magnetoresistance trace of Fig. 3.4 (c). Thornton et al. compared the magnetoresistance of wires with boundaries formed by low energy ion implantation (which offers a diffusive contribution to the wall scattering) to a second set of identically shaped samples formed by split gate confinement. Here, the edge scattering is mainly specular. These measurements are presented in the inset of Fig. 3.4 (c). The amplitude of the magnetoresistance peak is a measure of the probability b that the electron is scattered at the Hall bar wall as opposed to within the bulk. The contribution of bulk scattering is the same for the same sample shape independent of the Hall bar boundary. The wall formed by ion implantation causes a higher diffusive contribution such that the peak amplitude is more pronounced compared to the sample set formed through split gate confinement.

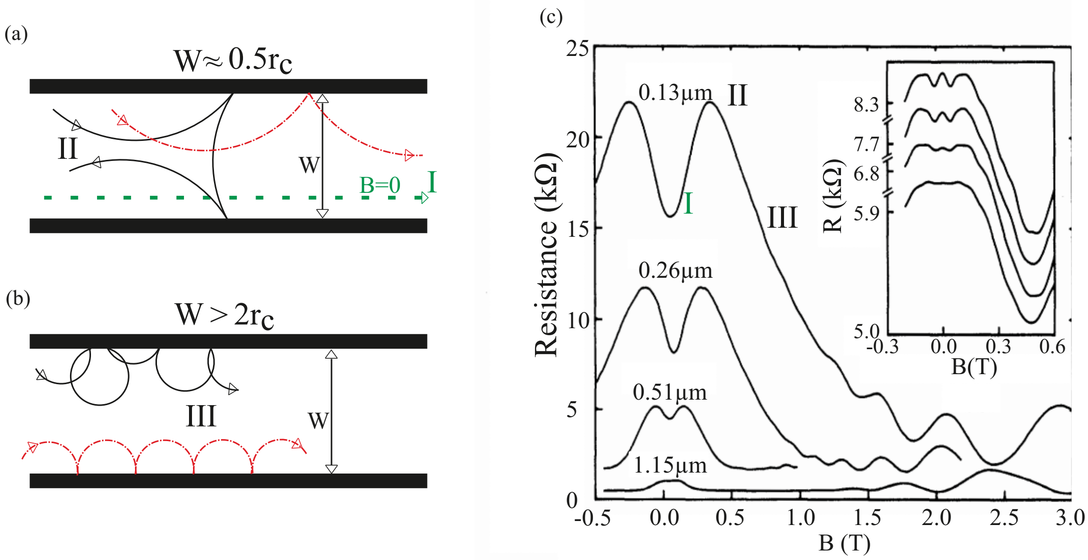

Figure 3.4: (a) Illustration of the classical effect causing the maximum in magnetoresistance. An electron is diffusively scattered at the Hall bar wall, turning its trajectory to the opposite direction (black trace). The dotted red trajectory corresponds to complete specular scattering, and the broken green line to the zero magnetic field case. (b) With increased B-field, the effect of diffusive boundary scattering (black trajectory) does not change the direction of propagation compared with complete specular scattering drawn in dotted red. (c) Measurement results and figure from citeThornton1989. The different classical effects described in parts (a) and (b) are denoted by I, II, and III, respectively; parts (a) and (b) are adapted from [61].

3.2.6 Giant negative magnetoresistance

In 2D materials of ultra-high quality, the mean free path of electrons can exceed hundreds of μm. At sub-Kelvin temperatures, pristine 2DEG samples exhibit *giant negative magnetoresistance* (GNMR). In most reports [31, 33, 65, 66], GNMR is composed of two peaks. The first is a narrow, approximately parabolic peak, which is centered around zero-magnetic field. Its width is in the range of tens of mT. This narrow peak is surrounded by a broader parabolic structure, which has its maximum at $B = 0$, too.

In some experimental reports, only the broader peak is reported and the smaller one is absent. [31, 66–68]

Many effects in 2D materials can lead to a decrease in resistivity once a magnetic field is exposed to the sample. Examples are weak localization [69, 70], memory effects (see Section 3.3), and ballistic effects such as the wire peak (see Subsection 3.2.5). These phenomena occur in similar magnetic field intervals, usually below 500 mT. The reported respective behavior under different, controlled experimental conditions can help to distinguish between the involved effects. The two parts of the GNMR show different behavior if the experimental conditions (temperature, in-plane magnetic field, sample width, electron density, or dc-electric field) are varied. This subsection aims to review the reported characteristics of the narrow and broad peaks of GNMR with respect to these different experimental parameters.

Dependency on temperature and the electron-electron interaction model

Fig. 3.5 (part (a)) depicts measurement results reported by Mani et al. [31]. As is visible from the magnetoresistivity of the plain 2DEG sample, its shape comprises a broad peak at the lowest temperature, which reduces with a temperature increase from 115 mK to 590 mK. The measurement results of Bockhorn et al. [65] presented in Fig. 3.5 (part (b)) show the same phenomenology in a similar temperature interval.

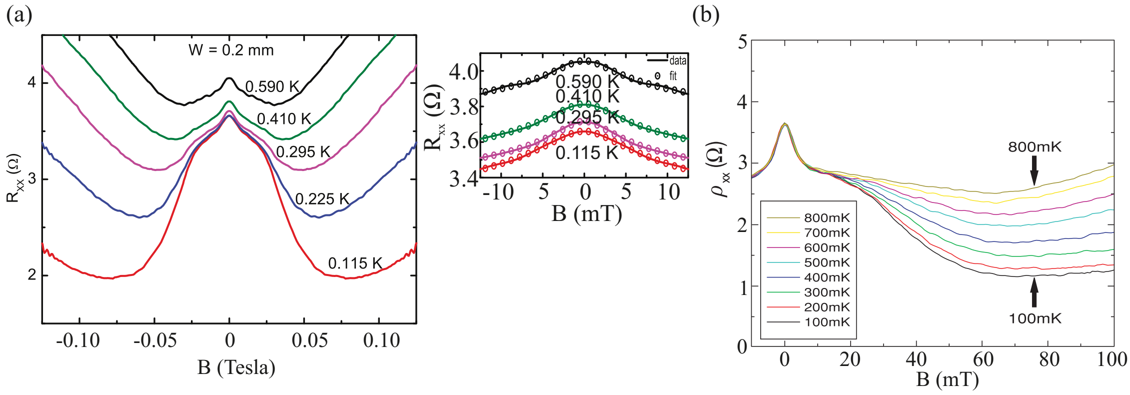

Figure 3.5: Temperature dependency of typical magnetoresistivity GNMR traces. (a) The small narrow peak is fitted to weak localization theory (upper right inset). The broad peak of GNMR reduces with temperature, and a shift of the complete trace to higher magnetoresistivity is observed (figure taken from [31]). (b) Evolution of the magnetoresistivity at sub-Kelvin temperatures. Just the broad GNMR peak exhibits a temperature dependency, while the narrow peak remains unchanged. The small peak was explained in this study by scattering at hard oval defect obstacles forming a 2DLG. Figure taken from [65].

In both measurements, a smaller peak on top of the broader one can be distinguished. In part (a) of the figure, the small peak can be identified in a B -field interval between -10 mT and 10 mT. It is not influenced in the temperature range up to 295 mK. At higher temperatures, the complete trace shifts upward to higher resistivity. The small peak shown in part (b) of the figure does not exhibit any dependency on temperatures below 800 mK.

Samaraweera et al. [69] suggested that the small temperature independent peak is caused by weak localization. The right-hand side of Fig. 3.5 (a) is a zoom-in of their data at magnetic fields below $B = \pm 10\,\mathrm{mT}$ with fits to the weak localization theory.

Another explanation for the small temperature-independent GNMR peak was provided by Bockhorn et al. [14, 32]. The peak is discussed in terms of a dilute 2D Lorentz gas, which is formed by residual hard core scattering centers (detailed in subsection 3.3.2).

The broader, temperature-dependent peak was interpreted by means of three models: the *quasiclassical disorder model* [71] of Mirlin et al., the *electron-electron interaction model* [72] of Gornyi et al., and a *hydrodynamic* description by Alekseev [34].

The Mirlin model explains that the magnetoresistance of a 2DEG is caused by interactions with long- and short- range disorder scatterers. Although it does not consider the influence of temperature on the system, it does provide an explanation for both GNMR peaks. A detailed presentation along the lines of the disorder model is given in Subsection 3.3.1. Bockhorn et al. were able to analyze their experimental data in accordance with the this model (see Subsection 3.3.2).

On the other hand, the hydrodynamic description by Alekseev provides a model for the temperature-dependent broad part of GNMR. After the hydrodynamic model, the electrons form a viscous flow of an electron fluid. [34] This model takes the influence of temperature into account, and this is further detailed in Subsection 3.2.7.

The third model, the electron–electron interaction model [72], predicts a parabolic negative magnetoresistance, which is highly temperature-dependent. Gornyi et al. [72] found a parabolic dependency of the broader GNMR peak with respect to B:

$$\frac{\rho_{xx}(B)}{\rho_0} = 1 - \beta B^2 \tag{3.2.6.1}$$

Through the opening factor β of the parabola, the temperature T is taken into account:

$$\beta = \mu^2 \frac{\rho_0}{R_K} \frac{c_0}{\pi} \left(\frac{\hbar/\tau}{k_B T} \right)^{1/2} \tag{3.2.6.2}$$

where $R_K = h/e^2$ is the Klitzing constant and $c_0 = 0.276$ is a numerical factor; furthermore, μ denotes the mobility; ρ_0 the zero-field resistivity; and τ the Drude scattering time.

Hatke et al. [66] and Bockhorn et al. [65] studied the temperature dependency of the broader peak in terms of this model. Results from [66] are depicted in Fig. 3.6. Part (a) presents the magnetoresistance of a sample that does not exhibit the small temperature-independent peak. To the broader temperature-dependent peak, parabolas with different opening factors β are fitted and thereby compared with the predictions of the electron–electron interaction model.

The full lines in Fig. 3.6 (part (a)) are measurement data from [66] and the dashed lines are fits to it with regard to equations 3.2.6.1 and 3.2.6.2. Part (b) of Fig. 3.6 presents β with respect to the temperature in a double logarithmic (left) and semilogarithmic representation (right). The dashed gray lines are the expected values (from equation 3.2.6.2), which deviate for all temperatures from the extracted experimental values.

Hatke et al. [66] stated that the electron–electron interaction model failed to describe the experimental findings despite a parabolic dependency with $\rho_{xx} \propto B^2$ being found. The deviations might be caused by the disorder potential of hard-core scatterers. For 1 K experimentally, $\beta = 1.1 \cdot 10^{-4}\,\mathrm{mT}^{-2}$ is found. This value is two orders of magnitude larger than the expected value of $\beta = 0.014 \cdot 10^{-4}\,\mathrm{mT}^{-2}$ from equations 3.2.6.1 and 3.2.6.2. [66]

Other studies by Bockhorn et al. [33] and Li et al. [73] reported β to be in the same order of magnitude as the model predicted. All reported experimental results show a parabolic dependency with regards to B in accordance with the electron–electron interaction model. In the temperature range below 1 K, the broader GNMR peak is strongly temperature dependent, whereas the smaller peak remains essentially unchanged.

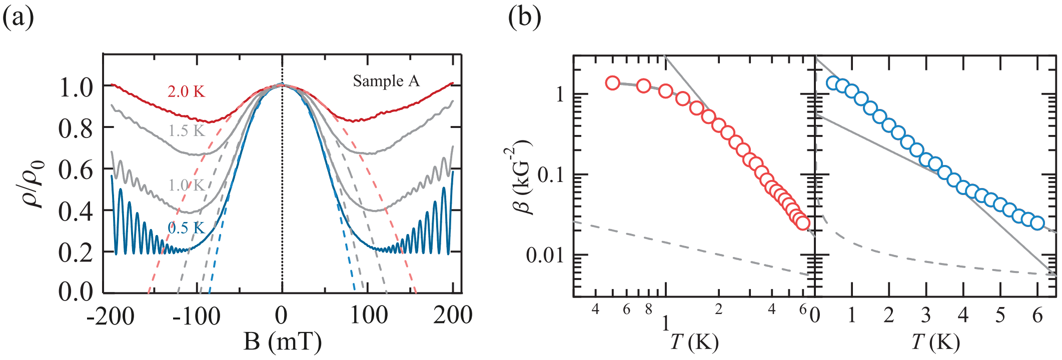

Figure 3.6: (a) Temperature evolution of the broad GNMR peak of a sample, where the small peak is absent in the magnetoresistivity. The dashed parabolas are fits to the measurement data (full lines) using the electron–electron interaction model. (b) The opening factor β is represented against temperature in a double logarithmic (left) and semilogarithmic representation (right). The dashed lines are predictions of the electron–electron interaction model, showing a discrepancy of two orders of magnitude from the experimentally extracted β. Figures taken from [66].

Dependency on in-plane magnetic fields

In-plane magnetic fields $B_{||}$ influence both GNMR peaks similarly to temperature, as reported in several experimental studies. [14, 66] The experimental findings from Hatke et al. [66] presented in Fig. 3.7 were obtained by measuring the magnetoresistivity of the sample in a tilted position with respect to the symmetry axis of the super conducting solenoid. By sweeping the magnetic field, both the in-plane $B_{||}$ and perpendicular component $B_{\perp}$ of the solenoid magnetic field B were varied. Therefore, determining the influence of $B_{||}$ on the small peak is difficult with this method because of the low total magnetic field B; however, the broad part of the GNMR can be quantified.

Indeed, as expected from the measurement results presented in part (a) of Fig. 3.7, the small peak is only slightly influenced in terms of shape by $B_{||}$.

Using another method, Dai et al. [74] investigated the influence of $B_{||}$ on the small GNMR peak.

Here, a two axis magnet was used allowing for variation of $B_\perp$ with a constant $B_{||}$. This measurement revealed the small peak to only be slightly influenced by $B_{||}$. The peak shape remained unchanged while the complete trace shifted to increased resistivity.

Both measurement methods convey a strong $B_{||}$ dependency of the broader GNMR peak. Returning to Fig. 2.7 (part (a)), with the tilt angle Θ, the negative slope of the broad part of the GNMR can be observed to change sign, which is because $B_{||}$ increases proportionally to $1/\cos(\Theta)$. The same is visible from the results presented in part (b), where the GNMR slope changes to be positive with $B_{||} \approx 800\,\mathrm{mT}$. In sum, it can be stated that the in-plane magnetic field has a pronounced influence on the broader GNMR peak, whereas the small temperature-independent peak is only slightly changed by $B_{||}$.

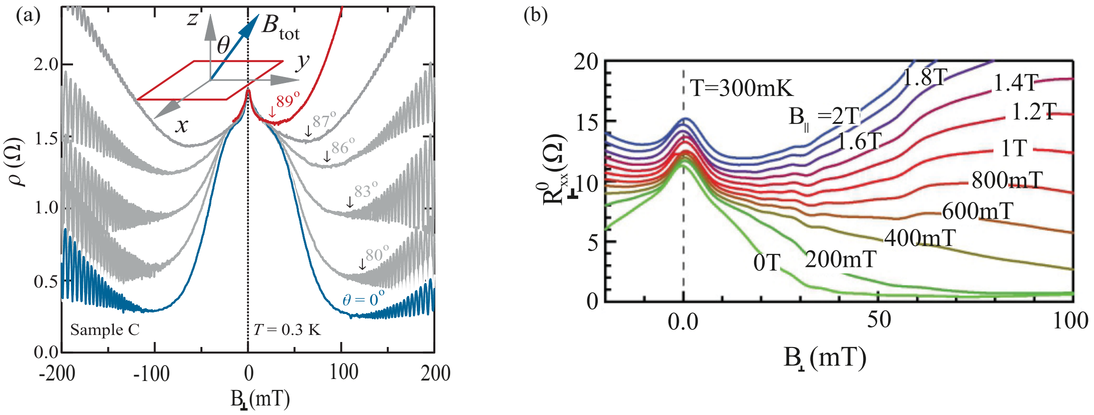

Figure 3.7: (a) Evolution of the magnetoresistivity with different tilt angles Θ represented against the magnetic field component $B_\perp$, which is perpendicular to the 2DEG plane. With increasing Θ, the in-plane magnetic field $B_{||}$ increases and the slope of the broad GNMR part changes from negative to positive. Figure taken from [66]]. (b) Here, different to (a), $B_{||}$ varies independently from $B_\perp$, showing a dramatic reduction of the negative slope of the broad GNMR peak as $B_{||}$ is increased. Figure taken from [74].

Dependency on the sample width

GNMR studies on the influence on the Hall bar width w have conveyed a strong enhancement of the broad GNMR peak if w is reduced. Bockhorn et al. [33] and Mani et al. [31] prepared samples with different w of adjacent measurement fields on the Hall bar. The aspect ratio of each field was maintained at one. An example geometry is provided in Fig. 3.8 (part (a)). [31]

The measurement fields ($w = 0.1$, $w = 0.1$, and $0.4\,\mathrm{mm}$) are marked with capital letters and the respective magnetoresistivity is presented in parts (b)-(d) of the figure. Part (e) presents the results from the three Hall bar widths at the lowest temperature of 1.4 K in one diagram. Both the small peak and the broad GNMR peak are more pronounced as w reduces.

The minima of the broad GNMR peak shift to lower resistivity and the peak width broadens when w reduces. From comparing the FWHM of the broad GNMR peak, Mani et al. [31] found the following empirical relationship:

$$\text{FWHM} \propto \frac{1}{\sqrt{w}} \tag{3.2.6.3}$$

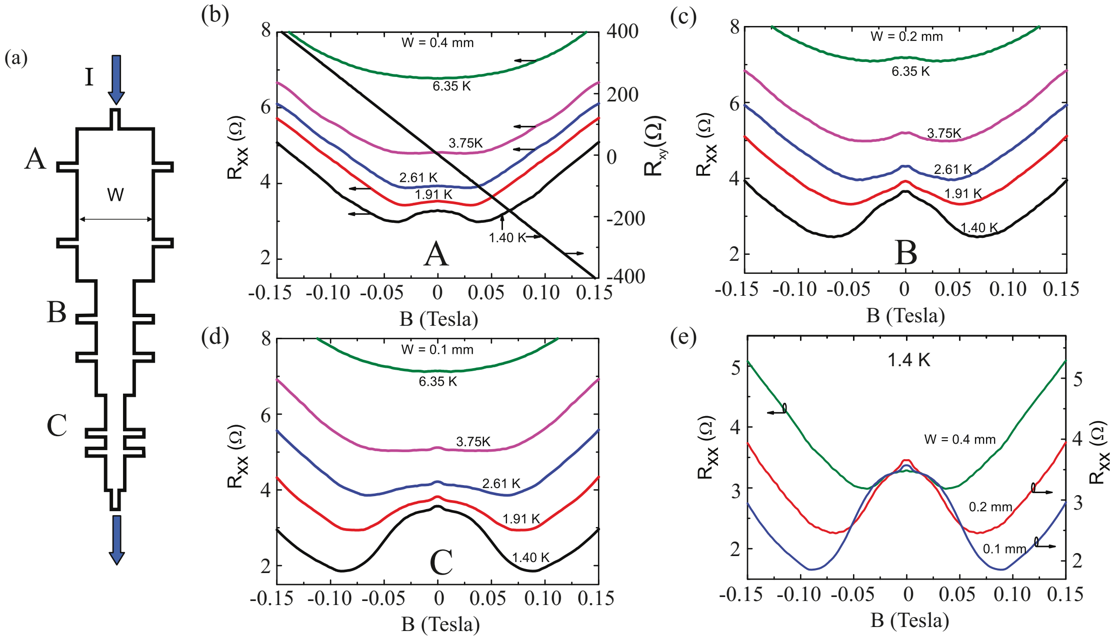

Figure 3.8: (a) Sketch of three Hall bar geometries in a row. The respective magnetoresistivities and their temperature evolutions from 1.4 K to 6.35 K are presented in parts (b)-(d). (e) Comparison of the three magnetoresistivities at 1.4 K for the three w. With decreasing w, both GNMR contributions are more pronounced. Figure taken from [31].

Parts (b)-(d) of Fig. 3.8 present the magnetoresistivities of the three w for different temperatures between 1.4 K and 6.35 K. The qualitative behavior is the same for all w:

With increasing temperature, the complete trace of the magnetoresistivity shifts to a higher magnitude, while the shape of the small peak remains essentially unchanged. The broad peak, on the other hand, reduces in amplitude and flattens with increasing temperature. This behavior is more pronounced for the $w = 0.4$ mm wide sample than it is for the narrower samples. To conclude, it can be stated that the broad GNMR part of a narrow Hall bar is more pronounced in amplitude and more temperature-stable than for a wider Hall bar.

In the hydrodynamic model by Alekseev [34], only the dependency on the Hall bar width is taken into account. The electron–electron interaction model [72] and quasiclassical disorder model [71] do not consider edges.

3.2.7 The hydrodynamic model of magnetoresistivity in 2DEG samples

A third model, which claims to describe the temperature evolution of the broad GNMR peak, is the hydrodynamic model proposed in 2016 by Alekseev. [34] This model is based on a range of hydrodynamic descriptions of electron transport in three [75–77] and two dimensions in metals [78–84], but here focuses on the electron transport in GaAs/AlGaAs quantum wells. Scaffidi et al. [85] extended this model by describing the transition from the ballistic to the hydrodynamic regime. The transition depends on the ratio of momentum-conserving scattering to nonmomentum-conserving scattering events.

In this hydrodynamic model, 2D electron transport is treated as in a viscous fluid. This description is justified because the electron elastic mean free path (i.e., the distance between collisions with phonons or static defects) exceeds the sample dimensions. This regime can be reached in modern high mobility samples, exhibiting mobilities in the range of $10^6 - 10^7\,\mathrm{cm}^2/(\mathrm{Vs})$. [34] The hydrodynamic model provides analytic expressions for the viscosity coefficients. These coefficients depend on the perpendicular magnetic field and temperature. The sample coordinates are described in a Cartesian coordinate system with x being the direction along the electron flow and y being that perpendicular to it. The main scattering contribution originates from the sample edges, where the electron's velocity is $v(y = \pm w/2) = 0$. Towards the Hall bar middle $(y = 0)$, $v(y)$ quadratically increases. Here, in accordance with the Poiseuille flow in conventional hydrodynamics, the electron velocity is maximal, that is, $v(y=0) = \max(v(y))$.

As detailed in Subsection 3.2.5 the scattering at the sample edges is either specular or diffusive or a mixture thereof. In the case of specular scattering and a long sample, the electron will scatter after several edge collisions with an impurity or a phonon in the bulk part of the channel, resulting in the Drude resistivity. [34] On the other hand, if the edge scattering is diffusive, the electron transport is determined by electron–electron collisions. The hydrodynamic regime is reached if the mean free path of electron–electron collisions l_{ee} is smaller than the sample width w (i.e., $l_{ee} \ll w$). Under these conditions, the electron transport is similar to the Poiseuille flow. The electrons exhibit different velocities along y, quadratically depending on the distance to the edges.

An additional magnetic field provides another length scale to the electron flow. In case the cyclotron radius R_c is smaller than the sample width, the hydrodynamic regime can be realized, although $l_{ee} > w$. The sketch provided in Fig. 3.9 (a) depicts the electron flow in the sample. With no magnetic field applied (left part), two neighboring layers of the electron fluid move with the velocities $v_x(y_1) > v_x(y_2)$. Electrons from one layer penetrate the other, causing viscous friction. With no magnetic field applied, a penetration length of l_2 can be defined. Under exposure to a magnetic field, the length l_2 in which the electrons are able to penetrate into the adjacent layer is limited by the cyclotron radius $R_c \ll l_2$. This reduces the viscous friction, resulting in a resistivity decrease as the magnetic field is increased, which is caused by the minimized penetration length.

The hydrodynamic model provides analytic expressions for the longitudinal magnetoresistivity and Hall resistivity. Both are derived from the viscosity η, which is direction-dependent if a magnetic

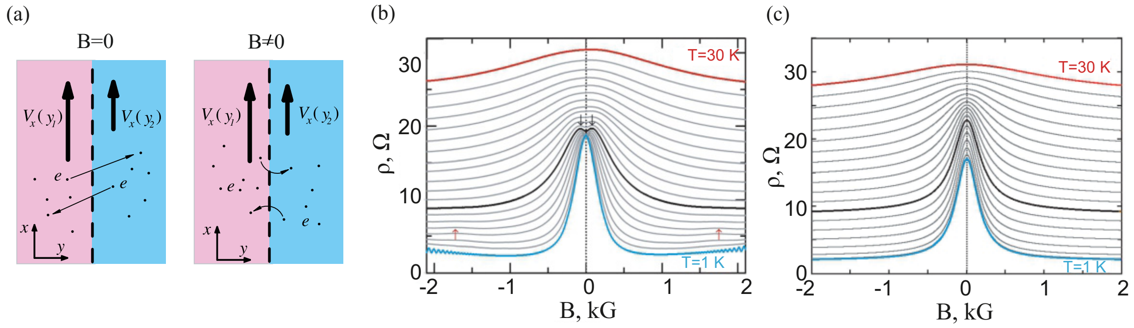

Figure 3.9: (a) Sketch illustrating the viscosity decrease caused by a perpendicular magnetic field. Left: When $B = 0$, electrons of a slower layer penetrate into adjacent layers and vice versa. This effect is reduced by $B \neq 0$ (right part) because the electron trajectories are bent and exhibit the cyclotron radius R_c. (b) Magnetoresistance of the sample studied in [68] for various temperatures. (c) Calculations from equations 3.2.7.5 and 3.2.7.7 of the hydrodynamic model [34] reproducing the data shown in (b). Figure taken from [34].

field is applied. The simplest case of the hydrodynamic model is if the magnetic field is absent. The velocity $v(y)$ then obeys:

$$\frac{\partial v(y)}{\partial t} = \eta \frac{\partial^2 v(y)}{\partial y^2} + \frac{e}{m^*} E_x \tag{3.2.7.1}$$

In this case $\eta = v_F l_{ee}/4$ is the viscosity of the 2DEG. $E_x = \vec{E} \cdot \vec{e}_x$ denotes the electric field applied along the x direction; m^* is the electron mass; and e is the electron charge. With help from the boundary condition $v(y = \pm w/2) = 0$ (required for diffusive scattering), the velocity profile can be derived. The current density $j_x(y)$ and velocity $v(y)$ are proportional to each other: $j_x(y) = en_e v(y)$. Therefore, the integration along y provides the resistivity:

$$\rho = \frac{m^*}{e^2 n_e \tau^*} \tag{3.2.7.2}$$

whereτ^* denotes the effective relaxation time and replaces the Drude scattering time τ in the hydrodynamic regime from $\rho_D = m^*/(e^2 n_e \tau)$. Furthermore, τ^* depends on the viscosity η and the 2DEG wire width:

$$\tau^* = \frac{w^2}{12\eta} \tag{3.2.7.3}$$

Equations 3.2.7.2 and 3.2.7.3 are not exact solutions. The second moment of the electron distribution function is not considered. Calculations for an ideal Fermi gas find the scattering time of the second moment to be $\tau_{2,ee}(T) = \hbar E_F/(A_{ee} T^2)$; that is, a temperature dependency on $\tau_{2,ee}(T)$ is considered [86]. Here, E_F is the Fermi energy and A_{ee} is a dimensionless value.

The scattering time τ_2 results from the temperature dependent $\tau_{e,ee}(T)$ and $\tau_{2,0}$ (a constant value). $\tau_{2,0}$ considers the contributions of scattering on residual disorder within the 2DEG contributing to the second moment. A more exact expression for η is therefore provided by

$$\eta = \frac{1}{4} v_F^2 \tau_2, \qquad \frac{1}{\tau_2(T)} = \frac{1}{\tau_{2,ee}(T)} + \frac{1}{\tau_{2,0}} \tag{3.2.7.4}$$

From these findings, the viscous flow of electrons is summed up as being inversely dependent on the sample width (i.e., $\rho_{xx} \propto 1/w^2$) as well as inversely dependent on the square of the temperature, $\rho \propto 1/T^2$.

Alekseev further provided the following expression for the resistivity ρ, which takes the bulk friction term $-v/\tau$ into account:

$$\rho = \frac{m^*}{e^2 n_e \tau} \frac{1}{1 - \tanh(\xi)/\xi}, \qquad \xi = \sqrt{\frac{3\tau^*}{\tau}} \tag{3.2.7.5}$$

Expressions 3.2.7.2-3.2.7.5 are descriptions for the zero-B case. Once a magnetic field acts on the 2DEG system, η is a tensor for which the diagonal elements are as follows:

$$\eta_{xx} = \frac{\eta}{1 + (2\omega_c \tau_2)^2}, \qquad \eta_{xy} = \frac{2\omega_c \tau_2 \eta}{1 + (2\omega_c \tau_2)^2} \tag{3.2.7.6}$$

where $\omega_c = eB/m^*$ is the cyclotron frequency. From this, and by solving the system of differential motion equations, a magnetic field-dependent expression for $\xi(\omega_c)$ can be derived, which is as follows:

$$\xi = \sqrt{\frac{3\tau^*}{\tau} \left[1 + (2\omega_c \tau_2)^2\right]} \tag{3.2.7.7}$$

Fig. 2.9 (c) presents the results of equations 3.9 and 3.2.7.7, with the numerical parameter chosen such that the measurement results from Shi et al. [68] are reproduced. These parameters are $\tau_0 = 4.5 \cdot 10^{-10}$ s, $\tau_{2,0} = 1.1 \cdot 10^{-11}$ s, $A_{ph} = 10^9\,\mathrm{s^{-1}K^{-1}}$, $A_{ee}^{FL} = 1.3 \cdot 10^9\,\mathrm{s^{-1}K^{-1}}$, and $w_{eff} = 10\,\mu$m. Alekseev found excellent agreement between the hydrodynamic model and measurements from [68].

In [68].Shi et al. claimed to report "colossal negative magnetoresistance." Here, different to other reports on GNMR, the magnetoresistance peak around zero magnetic field [31, 33, 65, 66] is a single peak rather than a double peak. Different to other samples exhibiting GNMR, the sample exhibits a moderate mobility of $\mu \approx 1.0 \cdot 10^6\,\mathrm{cm^2/Vs}$, which results in a relatively high zero-field resistivity of $\rho(B = 0) = 20\,\Omega$, whereas in other reports $\rho(B = 0)$ is in the range of a few ohms. Moreover, Shi et al. found an absent dependency on in-plane magnetic fields, whereas the broad part of GNMR is usually highly dependent on in-plane magnetic fields. [14, 87] Different to other reports is the temperature interval (1 K to 30 K) in which the peak remains. The broad GNMR part is usually only visible up to

1 K. [31]

Therefore, a theoretical description of the in-plane magnetic field dependency of GNMR is desirable to overcome the discrepancies within the experimental phenomenologies.

Gusev et al. [88] and Levin et al. [89] conducted experimental studies on 2DEG samples with relatively long wire lengths, and found reasonable consistency between the hydrodynamic model and measurements. Gusev et al. also measured the Hall viscosity and compared it with the hydrodynamic model [90]. In 2018, Alekseev [91] reported that the commonly found small temperature-independent peak of magnetoresistance [14, 31, 66] might be caused by specular scattering at the sample edges. This effect, sometimes called the “wire peak”, fits the required condition that $w \approx 0.55 R_c$ (see Subsection 3.2.5.1). Furthermore, Alekseev states that oval defects only slightly influence the hydrodynamic character of the electron flow through reducing the effective wire width.

3.3 The Lorentz gas in two dimensions

In 1905, Hendrik A. Lorentz proposed a 3D model system for describing the heat flux of electrons in metals. [1] Thus, heavier metal atoms are assumed to be fixed at random Poisson-distributed positions while electrons scatter elastically at them. Furthermore, the electrons do not interact with each other. The model was termed a “gas” because of the analogy of noninteracting particles within the model compared with ideal gases.

Much research has been conducted on Lorentz gases for the case of two dimensions [15, 19, 30, 35]. A magnetic field may be applied to this system to introduce another length scale. The perpendicular magnetic field bends the trajectory of an electron’s motion with $B \propto 1/r_c$. Moreover, the electron’s magnitude of velocity remains constant, but the direction changes with each specular collision at the Lorentz gas obstacles. Obstacles are allowed to mutually overlap.

The simple fact that the obstacles are static and their positions do not change is of strong physical relevance because it causes deviations from the Drude–Boltzmann model. The collisions are correlated to each other and therefore the Stoßzahlansatz is not valid anymore.

Within the static potential, it is possible that tracer particles probe the same sample area at least twice. The tracer’s further trajectory depends on prior collisions, which is why it is said to have a “memory”. [19, 23, 92]

The first memory effect to mention is the encircling of a void (see Fig. 3.10 (a)) or a single obstacle (Fig. 3.10 (b)) caused by a sufficiently high magnetic field. [19] This is also possible at an assembly of overlapping obstacles (see Fig. 3.10 (c)). This effect becomes more probable as the trajectory bending increases. These localized traces do not contribute to the conduction. The fraction of electrons maintained in undisturbed cyclotron orbits is [19] as follows:

$$P = \exp\left(\frac{-2\pi}{\omega_c \tau_0}\right) \tag{3.3.0.1}$$

where $\omega_c = eB/m^*$ is the cyclotron frequency of the electron; B denotes the magnetic field; and m^* is electron’s mass in GaAs. Furthermore, τ_0 is the average time between two collisions and related to the obstacle radius a and obstacle density n_s with: $\tau_0 = 1/(2n_s a v_F)$. The obstacle density n_s is the number of obstacles N per area A: $n_s = N/A$.

A high-mobility 2DEG with a mean free path in the range of a few tens of μm is a suitable host structure to experimentally realize a 2DLG. The obstacles are formed by reactive ion etched regions, which provide a hard-wall potential. [15, 93] The average distance l_{LG} that an electron can travel without being scattered at an obstacle is smaller than the 2DEG’s mean free path if the obstacle density is sufficiently high: $l_{LG} = (2n_s a)^{-1}$. Therefore the conductivity is dominated by the 2DLG embedded in the host structure.

The magnetoresistivity decreases with an increasing magnetic field, and is given using

$$\rho = \rho_0(1 - P) \tag{3.3.0.2}$$

where ρ_0 is the zero-field resistivity, which is: $\rho_0 = m^*/(e^2 n_e \tau_0)$.

There exists another type of memory effect, which is the backscattering of the tracer particle by the scattering angle π. The occurrence of this effect reduces with an applied magnetic field B. The trajectory marked with (d) in Fig. 3.10 illustrates a backscattering event of π at zero magnetic field. This effect is called the "corridor effect." Here, because the tracer particle was not scattered on the way to the obstacle, then it will not be scattered on the same path on its way back in the opposite direction. [22] At zero magnetic field, the conductance is reduced by the corridor effect. A sufficiently high applied magnetic field bends the tracer particle out of the corridor, which increases the conductivity. In Fig. 3.10 below, marked with (e), a tracer returns back to the initial obstacle at which it was scattered.

The probability of an electron exiting a corridor is low. This memory effect is enhanced by the fact that the electron's movement between the collisions with an obstacle lacks additional scattering; it is ballistic. A magnetic field breaks this effect by bending the electron trajectory out of the corridor region. A backscattering by π or 2π can be caused by scattering at more than two obstacles. The electron could scatter at an arbitrary constellation of obstacles, resulting in a trajectory resembling a polygon. The probability of this occurring increases with the obstacle density n_s.

All aforementioned memory effects share the fact that the tracer particle probes the same sample region at least twice. This is based on the static character of the scatterer landscape.

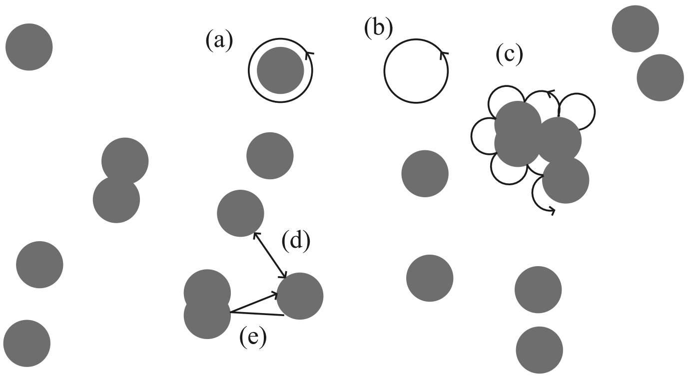

Figure 3.10: Different memory effects that may occur in a 2DLG: (a) An electron encircles a single obstacle or (b) a void space. The probability of this effect increases with the applied magnetic field such that the conductivity deceases exponentially with B. (c) The same effect as in (a) and (b) for a cluster of obstacles. (d) Backreflection by π. (e) A tracer particle returns back to the obstacle it started from. If a 2DLG is implemented within the 2DEG host material of GaAs/AlGaAs, then the intrinsic mean free path must be an order of magnitude larger than $l_{LG} = (2n_s a)^{-1}$ for the conductivity to be dominated by the 2DLG.

The system of the 2DLG is exotic in the first place, but a wide range of systems do exist in nature that are Lorentz gases or exhibit great similarity. Examples are the conduction of electronic conductors, the transport of cells in biological samples [94], the active motion of microswimmers in disordered arrays [95, 96], and localization phenomena in colloidal systems [97, 98]. The influence of a rotating magnetic field on cellular motion was investigated in [99]. Furthermore, in [10], the Brownian motion of biological microswimmers inhabiting a porous or crowded environment was studied in simulations of noninteracting Brownian particles in a Lorentz gas. Additionally, an analogy of bacterial 2D circular motion in the Lorentz model was found by Martens et al. [100].
This encourages further studies on the ideal 2DLG through experimental implementation in the 2DEG structure of GaAs/AlGaAs as well as in numerical molecular dynamics simulations.

3.3.1 Deviations from the Lorentz model by long-range scattering

Mirlin et al. [71] studied the quasiclassical magnetotransport of electrons moving in a 2DLG within the quasiclassical disorder model. This is formed by strong scatterers, such as antidots, impurities, or defects and is superimposed on the background of a smooth random potential. It was found that both mechanisms lead to a strong negative magnetoresistance, followed by a saturation of $\rho_{xx}(B)$, which is solely dependent on the smooth disorder potential. This approach is motivated by the fact that high-mobility 2DEGs are realized by a large separation distance between the donor layer and 2DEG plane. These remote donors provide a source of small angel scattering of electrons. Furthermore, residual disorder from impurities and interface roughness are additional limiting factors of mobility. Therefore, these impurities are considered to form a 2DLG with a momentum relaxation time τ_s (the integer s denotes short-range scattering). The magnetoresistivity of the 2DLG follows the Bobylev model [19, 101]:

$$\rho_{xx}(B) = \rho_0 \left(1 - \exp\left(-\frac{2\pi}{\omega_c \tau_s}\right)\right) \tag{3.3.1.1}$$

This relationship describes a dilute 2DLG, in which long-range scatterers are absent. As the long-range scattering contributions can be summed up in the momentum relaxation time τ_l, equation 3.3.1.1 is valid for $\tau_l = \infty$.
The Mirlin model assumes $\tau_l \gg \tau_s$, and thus it follows that the zero-B field resistivity ρ_0 is determined by hard-core scatterers: $\tau^{-1} = \tau_l^{-1} + \tau_s^{-1} \approx \tau_s^{-1}$.
In the Bobylev model, a finite magnetic field characterized by the cyclotron frequency ω_c reduces $\rho_{xx}(B)$ to exactly zero if electrons are only able to move in localized rosette-like trajectories around LG obstacles. This magnetic field of percolation is defined by the frequency: $\omega_{perc} = 1.67 v_F n_s^{0.5}$. This is modified by the smooth disorder potential because the guiding center of the electron can be shifted by δ, defined as follows:

$$\delta = \sqrt{4\pi v_F^3 / \omega_c^3 l_b} \tag{3.3.1.2}$$

With the image in mind of a tracer particle surrounded by a strip the width of an LG obstacle's diameter, a collision with an LG obstacle is possible if it is located within this strip. With a magnetic field applied, this strip area decreases and will not overlap with the strip area of the first revolution. This reduces memory effects because the tracer particle leaves its original ballistic corridor. For all finite magnetic fields the magnetoresistivity is modified compared with a plain 2DLG.
Mirlin distinguished two magnetic field intervals, where for low magnetic fields (i.e., $\omega_c \ll \omega_0$) the magnetoresistivity follows

$$\frac{\Delta\rho_{xx}}{\rho_0}(B) = -\left(\frac{\omega_c}{\omega_0}\right)^2 \tag{3.3.1.3}$$

where ω_0 is a parameter that takes the density n_s of short-range scatterers; the ratio of the short-range scattering length l_s; and the long-range scattering length l_l into account.

$$\omega_0 = \sqrt{2\pi n_j} \cdot v_F \cdot (2l_j/l_b)^{0.25} \tag{3.3.1.4}$$

where γ is a finite value between 0 and 1, which is a qualitative factor for the reflectivity of the obstacle.
For larger magnetic fields, the number of fulfilled cyclotron orbits increases per time interval, and therefore the time required to hit a new impurity increases. This yields a $1/B^4$ drop in resistivity:

$$\frac{\rho_{xx}}{\rho_0} \propto \left(\frac{\omega_0}{\omega_c}\right)^4 \tag{3.3.1.5}$$

Fig. 3.11 presents the magnetoresistivities of the simulation results presented in [71]. The momentum relaxation time of the short-range scatterers τ_s is fixed, while τ_l differs for the single traces. As the ratio τ_l/τ_s decreases, the results show that the traces broaden. This is in agreement with the analytical predictions of equations 3.3.1.3 and 3.3.1.5.
Usually the condition $\tau_l \gg \tau_s$ does not match experimental samples, where rather $\tau_l \approx \tau_s$ holds. There, a crossover can be found from the zero-field magnetoresistivity $\rho_{xx}(0) = (m^*/e^2 n_e)(\tau_l^{-1} + \tau_s^{-1})$ to a saturation at high magnetic fields of $\rho_{xx}(\omega_c \gg \omega_{perc}) = m/(e^2 n_e \tau_l)$. This was experimentally proven in [14, 65], as detailed in Subsection 3.2.6).
Although the Mirlin model does not satisfy the experimental conditions in general, it does provide an insightful picture of the influence of a random background potential on a true 2DLG. In particular, the investigations of a random background potential on a 2DLG presented in Chapter 5 are analyzed along the lines of the Mirlin model.

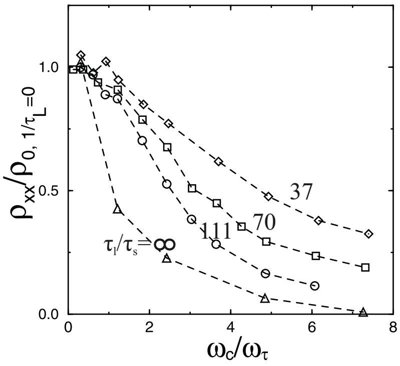

Figure 3.11: Magnetoresistivity from a simulation at fixed τ_s and different τ_l. A true 2DLG corresponds to $\tau_l/\tau_s = \infty$. As τ_l decreases (i.e., the smooth random scattering contribution is enlarged), the trace broadens and saturates later, which is determined solely by the background potential. Figure taken from [71].

3.3.2 The narrow peak of the GNMR - caused by a dilute 2DLG

Macroscopic growth defects [102–105] are well-known in the MBE crystal growth of GaAs/AlGaAs heterostructures. These defects occur in small numbers in all parts of the sample, are visible on the surface with an optical microscope, and are termed oval defects.

Bockhorn et al. [14, 32] found that the small peak of GNMR (see Subsection 3.2.6) is caused by oval defects, which are randomly distributed along the sample material. Furthermore, they observed samples comprising the highest number of oval defects to have the highest mobility and to show the most pronounced small magnetoresistance peaks with the strongest fall-off.

Because of the oval defects' random distribution and the hard potential at which electrons in the 2DEG sheet scatter, the system can be considered a 2DLG. The obstacle density n_s of such a 2DLG is in the dilute regime. Oval defects cause a similar hard wall potential to antidots. Here, the quasi-classical disorder model of Mirlin et al. [71] (see Subsection 3.3.1) is used for comparison with the measurement results because the density of the 2DLG is in the dilute limit, and long-range scattering is also considered. The source of the long-range scattering potential is the delta-doping layer, usually spaced from the 2DEG sheet in tens of nm. For low magnetic fields B at which $\omega_c < \omega_{perc}$, the magnetoresistivity is approximated to parabolically drop from zero-magnetic field. The parabolic shape is influenced by long- and short-ranged scattering events in this magnetic field interval.

For elevated B (i.e., $\omega_c > \omega_{perc}$), the magnetoresistivity approaches zero if the pristine 2DLG is not exposed to long-range scattering. Such exposure causes deviations from the pristine 2DLG case for all magnetic fields B. For ω_c above ω_{perc}, a saturation of magnetoresistivity $\rho_{xx}(B)$ is proposed, determined only by long-range scattering.

The small peak of GNMR is temperature-independent and can be differentiated from the broad part of GNMR by the temperature evolution. Fig. 3.12 depicts a measurement trace at 100 mK (in black) and at 800 mK (in grey). Marked with $\rho_{xx}(B_c)$ is the magnetoresistivity at the percolation magnetic field B_c. Above B_c $\rho_{xx}(B)$ increases with temperature.

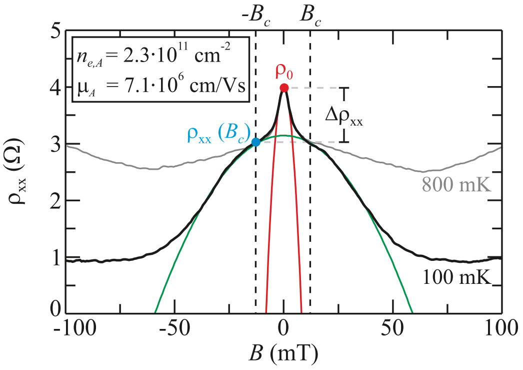

Figure 3.12: Magnetoresistivity of a pristine 2DEG showing the typical GNMR shape. The small inner peak is temperature-independent for the two temperatures of 100 mK and 800 mK. The red parabola is a fit to the measurement data in the temperature-independent interval $\pm B_c$. From the peak amplitude $\Delta\rho_{xx}$, the resistivity at the percolation magnetic field $\rho_{xx}(B_c)$, and the opening factor α of the fitted parabola, the density of oval defects can be determined from the quasiclassical disorder model. [71] Figure taken from [14].

Bockhorn et al. compared the small temperature-independent peak with the following approximated term from the quasiclassical disorder model [14, 32]:

(3.3.2.1)
$$\rho_{xx}(B) = \rho_{xx}(0)\left[1 - \frac{\omega_c^2 f(\tau_s/\tau_L)}{2\pi n_s v_F^2}\right]$$

where ω_c denotes the cyclotron frequency, τ_s the short-range scattering relaxation time, and τ_L the long-range scattering relaxation time. The long-range scattering time τ_L can be determined from $\rho_{xx}(B_c)$, which is the magnetoresistivity at the percolation magnetic field B_c (see Fig. 3.12 for an illustration):

(3.3.2.2)
$$\tau_L = \frac{m^*}{e^2 n_e \rho_{xx}(B_c)}$$

The short-range scattering time τ_s can be determined from the amplitude of the small peak: $\Delta\rho_{xx} = \rho_0 - \rho_{xx}(B_c)$. The amplitude is determined by both scattering types and the following expression holds for τ_s:

(3.3.2.3)
$$\tau_s = \frac{m^*}{e^2 n_e \Delta\rho_{xx}}$$

The term $f(x)$ in equation 3.3.2.1 is the following expression:

(3.3.2.4)
$$f(x) = \frac{2}{x+1}\int_0^\infty \frac{y J_1^2(y)}{x y^2 + 2(1 - J_0^2(y))} dy$$

where $x = \tau_s/\tau_L$. $J_{0,1}(y)$ are Bessel functions. Equations 3.3.2.1 and 3.3.2.4 are generalizations of Mirlin's quasiclassical disorder model [71], which are valid in the limit of$x \gg 1$. With the help of these approximation formulas, it is possible to determine the oval defect density n_s from the magnetoresistivity traces. In Fig. 3.12, the red parabola is a fit to the measurement data using equations 3.3.2.1 and 3.3.2.4.

Bockhorn et al. compared the results of n_s from the abovementioned procedure ($n_s = 1.3 \cdot 10^4\,\mathrm{cm}^{-2}$) with those from evaluations of the optical microscopy images ($n_s = 1.1 \cdot 10^4\,\mathrm{cm}^{-2}$), and found good agreement between the methods.

Macroscopic defects in the sample material can be identified by an optical microscope image of the sample surface (see Fig. 3.13 (b)), in which the back circles are oval defects that are unintentionally formed during MBE-crystal growth. Gallium droplets can form during the epitaxy, such that their location is random in height and position. The formation of oval defects is discussed in many reports. [102, 104, 105] The sketch in Fig. 3.13 (b) illustrates the gallium droplet and oval defect distribution within the crystal structure. The most agreed-upon explanation for the gallium droplet formation is that gallium oxides act as nucleation sides. Here, the crystal growth velocity is larger compared with plain areas of the crystal, and thus droplets form.

In addition, through comparing the magnetoresistivity of measurement fields with a typical oval defect density with areas with an increased number, Bockhorn et al. observed a characteristic influence on the shape and amplitude of the temperature-independent GNMR peak. Measurements at fields with higher oval defect densities indicate that the small peak is higher in amplitude as well as broader. Figure 3.13 compares the magnetoresistivity of a "giant peak" (red) and a "typical peak" (black).

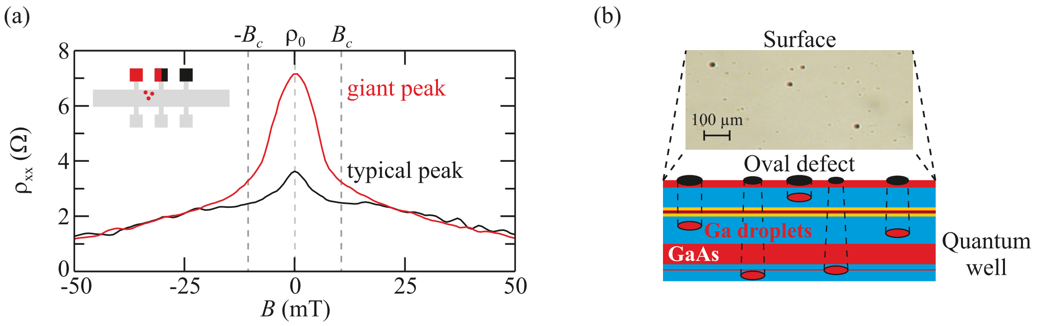

Figure 3.13: (a) Magnetoresistivity of two measurement fields. One contains a typical number of oval defects (black) and one a propagated number (red), showing that the peak amplitude and width increase with the oval defect density. (b) Optical microscope image of the sample surface and a sketch of a sample cross-section. Gallium droplets form during the MBE growth and fall on the sample during the growth procedure. Thus, oval defects form, which provide a source of hard scattering centers. Figure taken from [14].

Differences between the two peak types are attributed to the distribution of oval defects between the respective voltage probes. Both peaks exhibit the same phenomenologies with variations in

experimental conditions such as temperature and the dependency on in-plane magnetic fields.
To conclude, Bockhorn et al. [14, 32] suggested that the small temperature and in-plane magnetic field-independent GNMR peak are caused by oval defects, which are randomly distributed along the Hall bar. Because of this and their hard scattering potential, the measurement results can be explained by a dilute two-dimensional Lorentz gas formed by oval defects.

3.3.3 2DLG formed by circular obstacles in the dense limit

For the model system of a 2DLG comprising circular obstacles, Kuzmany and Spohn [18] found two percolation boundaries and proved their existence through numerical studies on the autocorrelation function. Above the first and below the second boundary, the system is insulating, whereas in between them the system is conducting. The magnetoconductivity of the system is determined by the elastic collisions of tracer particles with obstacles and also by the circular motion caused by the Lorentz force $\vec{F}_L = -e(\vec{v} \times \vec{B})$. Therefore the obstacle density n_s and the perpendicular magnetic field B are the two parameters that determine the conductivity and positions of the phase boundaries. To directly compare the parameters' obstacle density n_s and magnetic field B with the obstacle radius a, they are given in normalized units further on: for circular obstacles, the dimensionless density n^* is the area an obstacle covers (despite a factor of π):

$$n^* = \frac{N}{A} a^2 = n_s a^2 \tag{3.3.3.1}$$

The magnetic field is normalized to a magnetic field B_0 corresponding to the cyclotron radius, which is equal to the obstacle radius: $B_0 = m^* v_F/(ea)$.

$$\tilde{B} = \frac{B}{B_0} = \frac{a}{r_c}$$

where $r_c = m^* v_F/(eB)$ denotes the cyclotron radius. Fig. 3.14 (a) presents the phase-space of the 2DLG, where the parameters n^* and $\tilde{B}$ determine the conductivity.
The first boundary only depends on n^* (values of which were deduced in [106] for different obstacle shapes) and is independent of an applied magnetic field. For circular obstacles, the dimensionless obstacle density for which the system transits to the localized state is $n^*_{crit} = 0.359$. [30] Above n^*_{crit} a particle will not find free paths for diffusing further, which is independent of a trajectory bent by a magnetic field.
The second boundary does depend on the magnetic field for intermediate $n^* < n^*_{crit}$. Once for a given n^*, when a certain magnetic field $\tilde{B}_{ld,c}$ is reached, the dynamics of the tracer particles change from being conductive to being localized. Or, vice versa, for each magnetic field there exists a density $n^*_{ld,c}(\tilde{B}) < n^*_c$ that leads to the localization of all tracer particles. For the case of circular obstacles the position $\tilde{B}_{ld,c}$ can be analytically expressed as follows [30]:

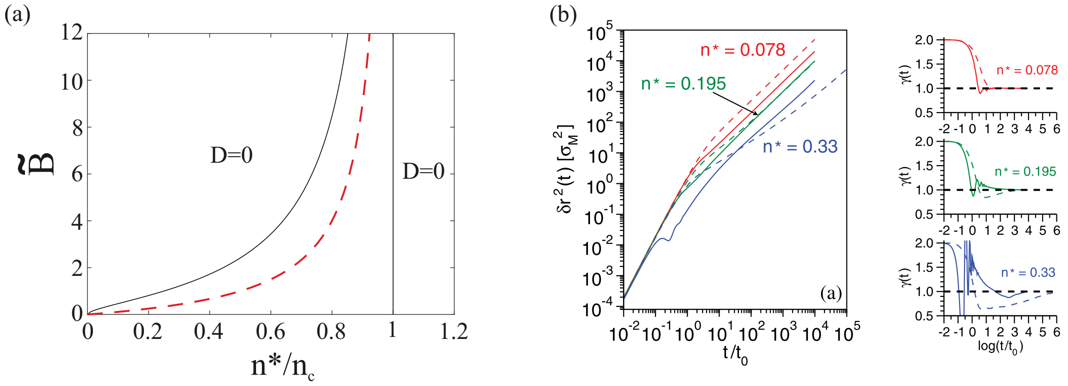

Figure 3.14: (a) Phase diagram of the 2DLG. A conducting phase is separated from insulation phases by two percolation boundaries. One occurs at $n^* < n^*_{crit}$ and depends on the applied $\tilde{B}$. The second one solely depends on n^*_{crit}. The red broken line corresponds to the maximal conductivity depending on $\tilde{B}$ and on n^*. Figure adapted from [15]. (b) Left: MSD for different n^*. The broken lines are the zero-field cases, the solid lines correspond to the respective $\tilde{B}$ of maximal conductivity. Right: For the three cases shown on the right-hand side the local exponent γ is presented vs. time. For $n^* = 0.195$ and $n^* = 0.33$, there are time intervals of several orders of magnitude where the transport is super-diffusive, causing the conductivity maximum. Figure from [15].

$$\tilde{B}_{ld,c} = \frac{1}{\sqrt{\frac{n_c^*}{n^*}} - 1} \tag{3.3.3.2}$$

As the gyration radius decreases with $\tilde{B}$, tracer particles are not able to reach a nearby obstacle and localize at the first obstacle they hit or a void space. In this state of the system, more complex localization scenarios are possible; for example, the electron is localized at a cluster formed by a number of obstacles.

In between the two phase boundaries, the system is conducting and it is possible to determine the diffusion matrix from molecular dynamics simulations. Furthermore, the conductivity can be measured under experimental conditions. Both methods are explained later in the paper.

A conductivity maximum between the phase boundaries was predicted by [18, 30], which was experimentally and numerically proven in by Siboni et al. [15]. Within the studies of [15], an empirical expression for the position of the conductivity maximum was found, which is as follows:

$$\tilde{B}_{max} = \frac{1}{n_c^*/n^* - 1} \tag{3.3.3.3}$$

$\tilde{B}_{max}$ is depicted by the broken red line in Fig. 3.14 (a).

From molecular dynamics (MD) event-driven simulations, the mean-squared displacement (MSD) can be determined for different n^* and $\tilde{B}$. The MSD is defined as $\delta r^2(t) = \langle [\vec{r}(t) - \vec{r}(0)]^2 \rangle$, where $\vec{r}(t)$ is the position of a single tracer at time t and $\langle ... \rangle$ denotes the ensemble average of all tracer particles.

From the long-time limit of the MSD, the diffusion constant can be determined using the Einstein relation:

$$D = \lim_{t\to\infty} \delta r^2(t)/4t \tag{3.3.3.4}$$

where D is directly proportional to the conductivity σ with: $\sigma = Dm^* e^2/(\pi\hbar^2)$. Therefore, results from simulations and experiments are directly comparable.

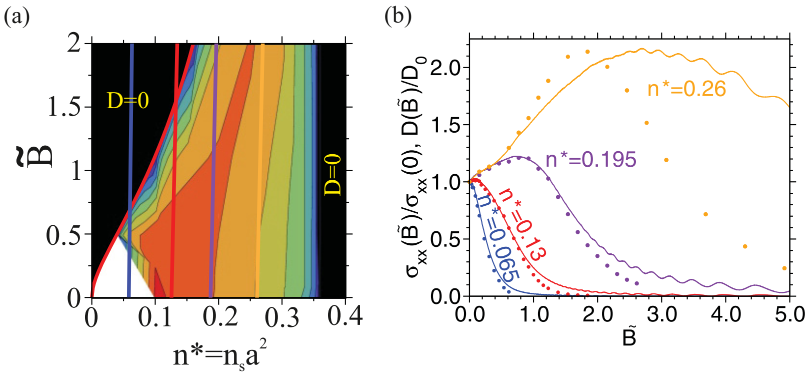

Figure 3.15: (a) Phase diagram of the 2DLG. The conductivity of the system is shown on a color scale (from black [insulating] to red [highly conductive]). At four n^*, indicated by vertical colored lines, samples were preprepared to measure the magnetoconductivity. Figure from [30]. (b) Magnetoconductivity (lines) with n^* ranging from $n^* = 0.065$ to 0.26 and the respective MD-simulation results (dots). As n^* increases, the magnetoconductivity maximum forms. For all four traces a deviation occurred between measurement and simulation at higher magnetic fields. Figure from [15].

Three examples of MSD are presented in Fig. 3.14 (right-hand side). The MSD at zero magnetic field is drawn with broken lines, whereas the MSD which corresponds to the $\tilde{B}_{max}$ of maximal conduction is presented by solid lines. The local exponent $\gamma(t) = d\log\left[\delta r^2(t)\right]/d\log(t)$ is a measure of the transport being sub- or superdiffusive; $\gamma = 1$ marks the case of diffusive behavior. As is visible from the right-hand side of Fig. 3.14 (b), where γ is presented for the three cases, there are time intervals of several orders of magnitude of super-diffusive motion of the tracer particles, followed by the approach to $\gamma = 1$ for long times. This behavior causes the maximum in conduction.

A comparison of experiment and simulation results is presented in Fig. 3.15 (b). As n^* increases, a maximum in conductivity develops. At higher magnetic fields a discrepancy exists between simulation and experiment. The values of the experimental conductivity are larger compared with the simulation. Most likely residual background impurities of the host structure prevent the electrons from localization along the 2DLG cluster contour, while the decreasing conductivity is caused by such localization. Unavoidable background impurities of the host structure and/or phonon contributions are reasons for the deviation between experiments and simulations. Chapter 5 provides a detailed experimental study on the influence of background impurities.

Part (a) of Fig. 3.15 is a phase-diagram of the 2DLG, where the conductivity is presented on a color scale ranging from absent (black) to the maximum conductivity (red). The vertical lines indicate the experimentally accessible parameters, presented in (b) and [15].

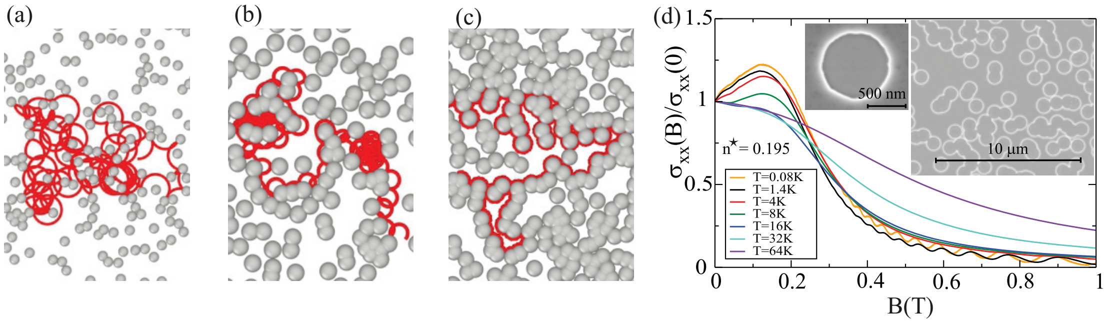

Figure 3.16: Example trajectories of an electron in a 2DLG with increasing n^* from (a)-(c). The trajectories are shown for $\tilde{B} = 0.35$, 1.0 , and 6.96. At these $\tilde{B}$, the max($D(n^*)$) is maximal, respectively. (d) The conduction maximum is a classical effect, as visible in the fact that the SdHo vanish at 4 K while the conduction maximum is temperature stable up to 16 K. Figures from [15].

As is visible in the local exponent presented in Fig. 3.14, transport in the 2DLG is super-diffusive at a certain n^* and the corresponding $\tilde{B}_{max}$. Exemplified trajectories at $\tilde{B}_{max}$ are provided in parts (a)-(c) of Fig. 3.16 for different n^*.

The maximum in $D(\tilde{B}_{max})$ can be explained on a microscopic scale by the electron's trajectory, which changes its character significantly with the applied magnetic field. Three magnetic field regimes can be identified in Fig. 3.16 (d), which is the experimental trace of the 2DLG with $n^* = 0.195$. At low magnetic fields the transport is mainly diffusive, which changes to a guided motion along the obstacle's contour at $\tilde{B}_{max}$, causing the maximum conductivity. A further increase of the magnetic field leads to the localization transition ($\tilde{B}_{ld,c}$), reducing the magnetoconductivity. Here, the tracer particle skips along a cluster of obstacles without being able to leave this assembly caused by the sufficiently small cyclotron radius. The different-colored traces depict the temperature evolution of the magnetoconductivity from 80 mK to 64 K. The SdHo vanish at 4 K, whereas the conductivity maximum is visible up to 16 K. This indicates that this effect is of a classical nature and quantum effects are-if present-only a small contribution.

3.3.4 The Ehrenfest windtree model

In 1911, Paul and Tatjana Ehrenfest published a special version of a Lorentz gas, where the obstacles are squares [27, 107]. The tracer particles are allowed to move in two dimensions in the void spaces of the random arrangement of nonoverlapping squares. Later in 1972, the model was extended by Gates for the case of overlapping squares [108]. Because of the flat obstacle boundaries, the corridor effect (see Section 3.3) becomes a dominant contribution to the tracer particles' trajectories. There are many retracing events in this system; for example, the tracer particle is reflected back and forth several times such that in short time intervals it travels along the same region. This is caused by the nonchaotic scattering of the tracer particles at the flat boundaries.

In particular, there is the case of retroreflection, which means the tracer particle exits an obstacle assembly in the same direction as it enters but in the opposite orientation. Obstacles can form a retroreflecting cone because the edges of obstacles that are overlapping or placed nearby form an angle of $\pi/4$ (see Fig. 3.17 (c)). Fig. 3.17 depicts possible example trajectories for the case of nonoverlapping (a)- (b) and overlapping obstacles (c).

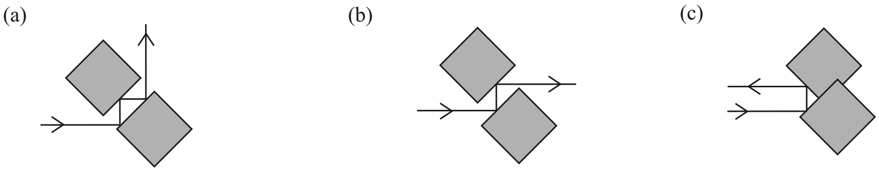

Figure 3.17: Examples of possible trajectory parts of nonoverlapping (a), (b) and overlapping (c) squared obstacles of the EWT. Figure adapted from [109].

For the case of overlapping square obstacles, theories in the low density limit have shown that the MSD does deviate from linear growth in a long-time limit. [109–111] Instead, it shows a sublinear growth with

$$\delta r^2(t) \propto t^{1-4n^*/3} \tag{3.3.4.1}$$

where n^* is defined as $n^* = n_s a^2$ (a is half of the length of a square's diagonal). Thus, the Ehrenfest wind-tree model (EWT) is predicted to be a system where the diffusion is anomalous, which was confirmed by an early computer simulation by Wood et al. [28].

3.4 Nonequilibrium phenomena at high Landau levels in 2DEGs

Usually, experimental conditions are chosen such that the 2DEG is in equilibrium as much as possible. One aspect involves keeping the Fermi level tilt as low as possible, thereby preventing heating caused by electric fields that are too high. Additionally, the temperature is kept in the mK range to minimize interactions with phonons, and any radiation is kept from the sample by means of radiation shields, filters, and shielded measurement cables. However, there are many nonequilibrium effects once the 2DEG system interacts with external forces by means of, for example, high electric fields, increased temperature, or irradiation. These phenomena include Hall induced resistance oscillations (HIRO) [112], phonon-induced resistance oscillations (PIRO) [113], and microwave-induced resistance oscillations (MIRO) [114]. Within the MIRO phenomenon, zero-resistance states were also observed [115]. In magnetotransport, all abovementioned types of nonequilibrium phenomena have a $1/B$ -periodicity where the period is determined by the commensurability of the exciting external force with LL spacing. For all oscillations, the magnetic field range of interest is below approximately 300 mT. At these fields, the SdHo are not yet fully evolved, and thus adjacent LL overlap (see subsection 3.2.2.1). On the other hand, the DOS experiences a modulation at these magnetic fields. The MIRO, HIRO, and PIRO mechanisms are all based on electronic transitions between these still-overlapping LLs, and the following three subsections are dedicated to their physical mechanisms.

3.4.1 Microwave-induced resistance oscillations

2DEG samples with sufficiently high mobility ($\approx 10^6\,\mathrm{cm}^2/\mathrm{Vs}$) show large oscillations in longitudinal magnetoresistance when subjected to weak magnetic fields and illuminated with microwave radiation. [114] These oscillations have been observed in many different measurement setups, including Corbino-disk-shaped 2DEGs [116], capacitively coupled 2DEGs [117], 2DEG structures with patterned triangular antidot lattices [118], and two-subband 2DEGs [119].
Fig. 3.18 shows the magnetoresistivity with (solid lines) and without microwave irradiation (broken line) for frequencies between 45 GHz and 94 GHz. This measurement was initially published in [114]. The oscillation maxima are marked with integer numbers. As the integer number j is represented against $1/B$, a linear dependence is observed (compare part (b) of 3.18). Within these experimental conditions the effect of magnetoplasmon resonance [118] also occurs, marked by arrows in the two upper traces. The MIRO periodicity is given by:

$$\epsilon_{ac} = \omega/\omega_c \tag{3.4.1.1}$$

where $\omega = 2\pi f$ denotes the irradiation frequency and ω_c the cyclotron frequency. Another aspect of the phenomenology of this effect is that the maxima (ϵ_{ac}^{+}) and minima (ϵ_{ac}^{-}) do not exactly fall on integer numbers j but are shifted by a phase φ_{ac} such that

$$\epsilon_{ac}^{\pm} \approx j \mp \varphi_{ac} \tag{3.4.1.2}$$

φ_{ac} was theoretically predicted to be 1/4 in the regime of overlapping LLs [17], which has been reported in many experiments. [120, 121] For experimental conditions with separated LL, φ_{ac} is reduced. [74, 122] The phase depends on the irradiated optical power; specifically, with higher irradiation power, φ_{ac} is reduced and the maxima positions shift toward harmonics of the cyclotron resonance. [123] At low magnetic fields and low irradiation power the difference in resistivity between irradiated and dark conditions $\delta\rho_\omega$ follows

$$\delta\rho_\omega = -A_\omega \epsilon_{ac} \sin(2\pi\epsilon_{ac}) \exp(-2\pi/\omega_c\tau_q) \tag{3.4.1.3}$$

where A_ω is the oscillation amplitude, $\delta\rho_\omega$ the varying part of the magnetoresistivity, and τ_q the quantum scattering time.

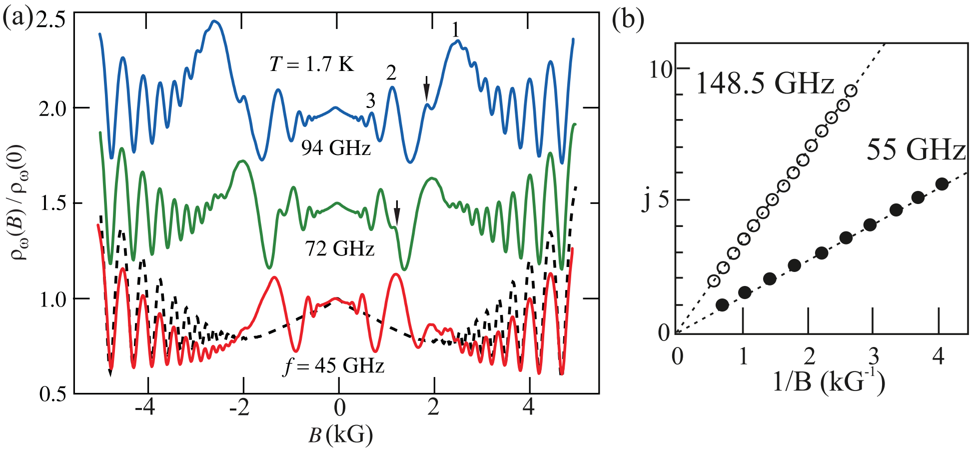

Figure 3.18: (a) MIRO measurements for three different irradiation frequencies. The magnetoresistivity measured in darkness is shown by the broken line. The traces have a vertical offset. The integer number denotes the order of the MIRO peak, and the arrows mark the magnetoplasmon resonance. Figure taken from [17]. (b) Index of the extremum vs. $1/B$. From the slope of this representation the electron effective mass $m^* \approx 0.068 m_e$ is determined. Figure from [114].

Additionally, MIRO show a decrease of A_ω as the irradiation frequency is increased while the optical output power is kept constant (see Fig. 3.19 (a)). This was systematically measured by Yang et. al [116]. The highest radiation frequencies at which MIRO were reported lay between 0.7 THz and 1.63 THz [124, 125]. As the LL spacing increases with increasing irradiation frequency, the reduced overlap of adjacent LL causes a less possible transition of electrons along several LL distances.

Within the MIRO mechanism, multiphoton processes under high-intensity microwave irradiation are possible. [126] The high number of photons cause electron transitions along j LL distances with m

photons being involved, and thus the periodicity follows $\epsilon_j^{(m)} = \frac{j}{m} + \varphi_j^{(m)}$. For example the electron's transition along $m = 3$ LL with $j = 2$ photons involved is illustrated by the first inset of Fig. 3.19 (b) occurring at ≈ 50 mT. [126]

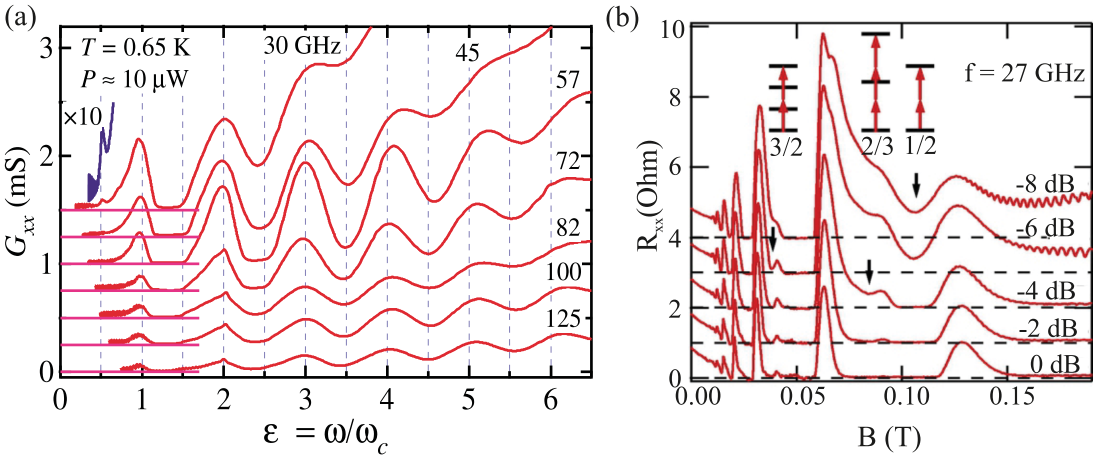

Figure 3.19: (a) Comparison of the MIRO for different irradiation frequencies. The irradiation intensity is constant with $P = 10\,\mu$W. As the frequency is increased from the upper to the lower trace, the oscillation amplitude reduces. Figure taken from [116]. (b) In the regime of high microwave irradiation power the minima of the MIRO evolve into ZRS. Marked by vertical arrows are multiple photon excitations along several LL occurring for example at 100 mT, two photons excite an electron along one LL distance. Each trace is offset. Figure taken from [126].

Another fascinating effect is that MIRO minima evolve into zero-resistance states if the sample has a high mobility $\mu \geq 10^7 \mathrm{cm}^2/\mathrm{Vs}$, low temperature ≤ 1.4 K, and is irradiated with sufficiently high irradiation power. [115] Different from the occurrence of zero-resistance states in the minima of SdHo, the accompanied Hall resistivity does not quantize within the MIRO mechanism.

There are two major explanations for the occurrence of MIRO: the inelastic mechanism [127] and the displacement mechanism [128]. The former explains MIRO through a change of the electron distribution function, which is induced by microwave radiation and is therefore more applicable at low temperatures. The latter explains the induced oscillations by radiation-induced additional currents, which are caused by scattering off disorder potentials. Fig. 3.20 (b) illustrates electrons absorbing photon energy and being excited by the energy $\hbar\omega$. This excitation is accompanied by a scattering event, and thus no selection rule is infringed. Hence, the jump of an electron along several LL leads to a shift of the guiding center either to the left or right by a distance ΔX. After this shift along the x-direction, the longitudinal current is either enhanced or decreased depending on the final density of states after excitation. If the number of states at the left part of the Hall bar exceeds the number of states at the right part, then the longitudinal current is enhanced, whereas it is decreased if the final density of states is the opposite. As this depends on the Landau-level spacing, the resistance oscillates $1/B$ periodically. [128]

The PIRO and HIRO mechanisms are explained in a similar way to MIRO, despite the excitation being different in the first place. For PIRO, the exciting particle is an acoustic phonon. For HIRO, the LLs are tilted by the high electric field such that the Hall drift is sufficient to cause scattering off disorder. Thus, the magnetoresistivity is periodically modulated.

Part (a) of Fig. 3.20 is an illustration of the guiding center shift comparing the position of the cyclotron orbit before and after excitation. [17]

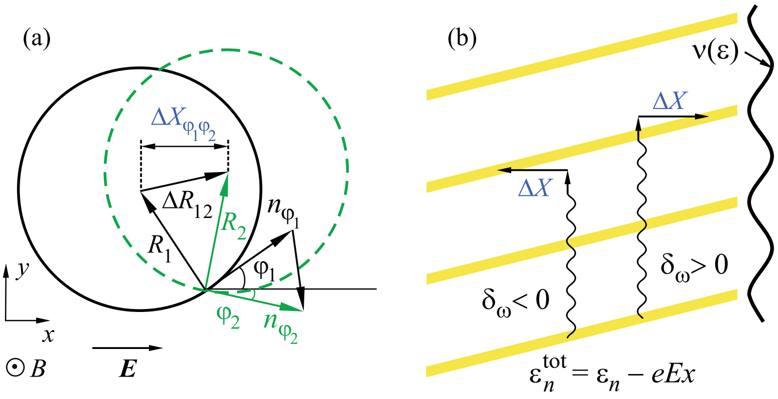

Figure 3.20: Illustration of the MIRO mechanism. (a) Guiding-center orbit before excitation (black) and shifted cyclotron orbit after excitation (green). The electron is quasi-elastically scattered at a source of disorder within the sample. (b) Tilted LL are drawn in yellow. As the electron is energetically shifted by the photon energy along two LL, it experiences a shift ΔX along the sample length. Figure taken from [17].

Different to other $1/B$ periodic oscillations, MIRO are independent of the carrier density n_e of the sample and depend only on the irradiation frequency and applied magnetic field.

3.4.2 Hall-induced resistance oscillations

HIRO, which were first observed in 2002 by Yang et al. [112], are another member of $1/B$ periodic magnetoresistance oscillations at high filling factors. Here, the 2DEG system is brought out of equilibrium by applying a high electric field along the sample's longitudinal direction. With the current density I_{DC} being in the range of 1 A/m a mechanism similar to Zener tunneling [129] becomes possible. Because of the large current density, the Hall electric field is high enough that the degeneracy of the Landau orbits along the y-direction is lifted. This allows for transitions between the occupied LL below the Fermi energy E_F and the empty orbits above E_F, which are separated at a distance of $2R_c$ ($R_c = m^* v_F/(eB)$ is the cyclotron radius).

Whenever the condition of

$$2R_c eE_y = \epsilon\hbar\omega_c \qquad (3.4.2.1)$$

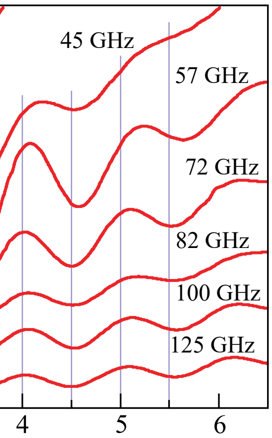

G_{xx} of a Corbino sample
0^7 cm^2/V s) as a function
, labeled according to f =
ted from Yang *et al.*, 2003.

RO [which produces
on the correlation prop-
d] may remain relevant

past decade MIRO have
iation frequencies, from
st, 2004) to 1.5 THz
the majority of experi-
30 to 150 GHz, which
typical 2DEG. At lower
weaker B and are there-
t higher frequencies, the
ll (Yang *et al.*, 2003;
, 2009), as illustrated in
sured in a Corbino disk
≥ 2 and the microwave
tent with $\delta\rho_\omega \propto \omega^{-4}$, in
and (99).

cerning MIRO can be
f Landau quantization
momentum relaxation
the energy distribution
dened LLs (inelastic
es both effects in terms

FIG. 10 (color online). (a) Shift of the guiding center of a cyclotron orbit due to quasielastic scattering off disorder. (b) Schematics of the correlations between the direction of the cyclotron-orbit shifts ΔX in the process of photon absorption and the sign of the detuning $\delta_\omega = \omega/\omega_c - 2$ for the second harmonic of the CR. The stripes mark the DOS maxima $\varepsilon_n = (n + 1/2)\omega_c$ in LLs tilted by a dc field.

1. Inelastic and displacement mechanisms

Initially MIRO were attributed (Durst *et al.*, 2003; Vavilov and Aleiner, 2004) to the displacement mechanism which accounts for spatial displacements of quasiclassical electron orbits due to radiation-assisted scattering off disorder. Because of Landau quantization, which leads to a periodic modulation in the DOS $\tilde{\nu}(\varepsilon) \simeq \tilde{\nu}(\varepsilon + \omega_c)$ (see Sec. II.C.1), the preferred direction of these displacements with respect to the symmetry-breaking dc field oscillates with ω/ω_c. This results in MIRO with a phase and a period which agree with those observed in experiment. Photoconductivity oscillations governed by the displacement mechanism were in fact predicted long ago (Ryzhii, 1970; Ryzhii, Suris, and Shchamkhalova, 1986) in the limit of separated LLs and a strong dc field. This mechanism was further studied using various approaches and approximations in a number of theoretical works (Anderson and Brinkman, 2003; Durst *et al.*, 2003; Lei and Liu, 2003; Ryzhii and Suris, 2003; Shi and Xie, 2003; Lee and Leinaas, 2004; Park, 2004; Ryzhii, Chaplik, and Suris, 2004; Vavilov and Aleiner, 2004; Torres and Kunold, 2005; Kashuba, 2006a, 2006b; Auerbach and Pai, 2007; Dmitriev, Mirlin, and Polyakov, 2007a; Volkov and Takhtamirov, 2007; Khodas and Vavilov, 2008; Dmitriev *et al.*, 2009). Soon after the experimental observations of MIRO, Dmitriev, Mirlin, and Polyakov (2003) proposed is satisfied, a transition of an electron along the tilted Landau-level potential is possible. $\epsilon_{DC} = 1, 2, 3, \ldots$ is an integer accounting for the harmonics of HIRO in accordance with the other $1/B$ periodic oscillations at high filling factors. The left-hand side of equation 3.4.2.1 is the energetic difference between the origins of two neighboring Landau orbits. The Hall electric field E_y depends on the applied magnetic field and the electron's drift velocity v_D:

$$E_y = v_D B = \frac{J_{DC}}{n_e e} \cdot B = \frac{I_{DC}}{w n_e e} \cdot B \tag{3.4.2.2}$$

Here, w denotes the Hall bar width, n_e the electron density, and I_{DC} the source drain current. From equations 3.4.2.1 and 3.4.2.2 the magnetic fields at which the HIRO amplitude is maximized follow to be

$$B_{\max} = \frac{2}{\epsilon_{DC}} \cdot \left(\frac{m^*}{e}\right)^2 \frac{v_F I_{DC}}{w n_e \hbar} \tag{3.4.2.3}$$

Experimentally, HIRO are measurable with standard lock-in technique, although their amplitude is better pronounced in the differential magnetoresistance $r_{xx} = (\partial V/\partial I)_{I_{DC}}$. The exact measurement principle is explained in Section 7.2.

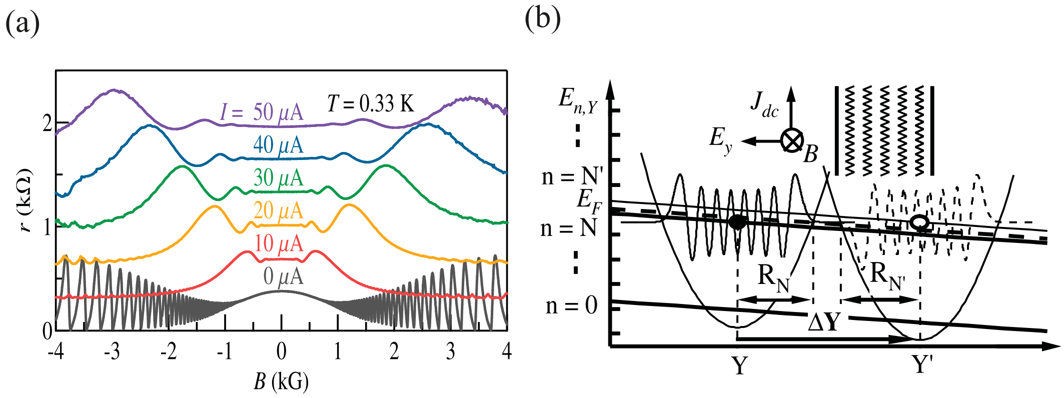

Figure 3.21: (a) Differential magnetoresistivity r_{xx} for different source-drain currents I_{DC} measured at a sample with $w = 50\,\mu\mathrm{m}$. Each HIRO maximum shifts linearly with I_{DC}. Traces are vertically offset by $0.3\,\mathrm{k}\Omega$. (b) The LLs are spatially tilted along the y -direction with the same slope as E_F. Elastic scattering provides a transition between different LLs, which is accompanied by a shift along the$y$-direction of $\Delta Y = Y' - Y = l\hbar\omega_c/eE_y$. The maximum distance for this transition is $\Delta Y \approx 2R_c$, that is, when the overlap between the wave function is minimized. Figure taken from [112].

A typical measurement of HIRO is shown in Fig. 3.21 (a). The extremal positions shift linearly with the applied source drain current and their position are $1/B$ periodic. Similar to PIRO (compare with Subsection 3.4.3), the HIRO extremal positions depend on the $n^{-1/2}$. Part (b) of Fig. 3.21 is an illustration of the HIRO mechanism. As a large current density J_{DC} is applied along the sample (see the upper-left inset), a Hall electric field builds up that is proportional to the applied magnetic field B and J_{DC}. Due to E_y, the LLs are not energetically degenerated anymore, and a transition of an electron from the highest filled LL below E_F to the next unfilled LL becomes possible. The position of the electrons along the y-direction changes by maximal $\Delta Y \approx 2R_c$, which is when the overlap of the electron wave functions is minimized.

The transition of an electron along more than one LL must be accompanied by a scattering process due to momentum conservation. For the HIRO mechanism to become possible, a sufficient amount of short-range scatterers must be present. This motivated the HIRO measurements accompanied by an increase of the bath temperature [130], such that another scattering channel was offered. Another possibility is increasing the random scattering potential by means of a dilute Lorentz gas, of which measurement results are presented in Section 7.2.

3.4.3 Phonon-induced resistance oscillations

PIRO are another class of magnetoresistance oscillations. Because the GaAs is a zincblende crystal with two basis atoms, six phonon branches exist: three optical and three acoustic. [131]

In 1961, resonant magneto–phonon interaction in a 2DEG system with optical phonons was predicted by Gurevich et al. [132] and measured in 1980 by Tsui et al. [133]. The experiments confirmed that oscillations in resistivity occur with a periodicity of ω_{LO}/ω_c, where ω_{LO} denotes the frequency of a longitudinal optical phonon and ω_c the electrons' cyclotron angular frequency. As optical phonons have an energy of approximately 30 meV, magnetoresistance oscillations from them are not measurable below 100 K because the vibrational energy of the crystal lattice is not sufficient. The required perpendicular magnetic field for the optical PIRO is in the range of 10 T.

In [132], the resonant interaction of 2DEG electrons with the acoustic phonon branch was also predicted. The first observation in 2001 [113] was possible because of the increased charge carrier mobility of $\mu \approx 10^6 \text{cm}^2/\text{Vs}$.

Both phonon resonances from optical and acoustic phonons are commonly called PIRO. In the following chapters, this term is only used for the resonant interaction with the acoustic phonon branch.

Resonances with acoustic phonons occur at weak magnetic fields ($B < 300\,\text{mT}$) and slightly elevated temperatures in the range of $2\,\text{K} < T < 9\,\text{K}$. A measurement of PIRO by Zudov et al. is depicted in Fig. 3.22. Four maxima are marked by integers l in the uppermost trace and their $1/B$ periodicity is conveyed by the linear dependency of the l vs. $1/B$ representation in the inset. The PIRO superimpose on the magnetoresistivity trace with their amplitude being below 10 % of the measurement signal.

Similar to HIRO and MIRO, PIRO originate from indirect transitions between LLs (either higher or lower), which means that in addition to the increase in energy, the direction of the electron changes. Here, the phonon is the energy-mediating particle. The dispersion of acoustic phonons near the Γ point of the GaAs crystal is linear to a good approximation, allowing the phonon's frequency to be defined by: $\omega_s = 2k_F s$, where s is the sound velocity of either the longitudinal or transversal

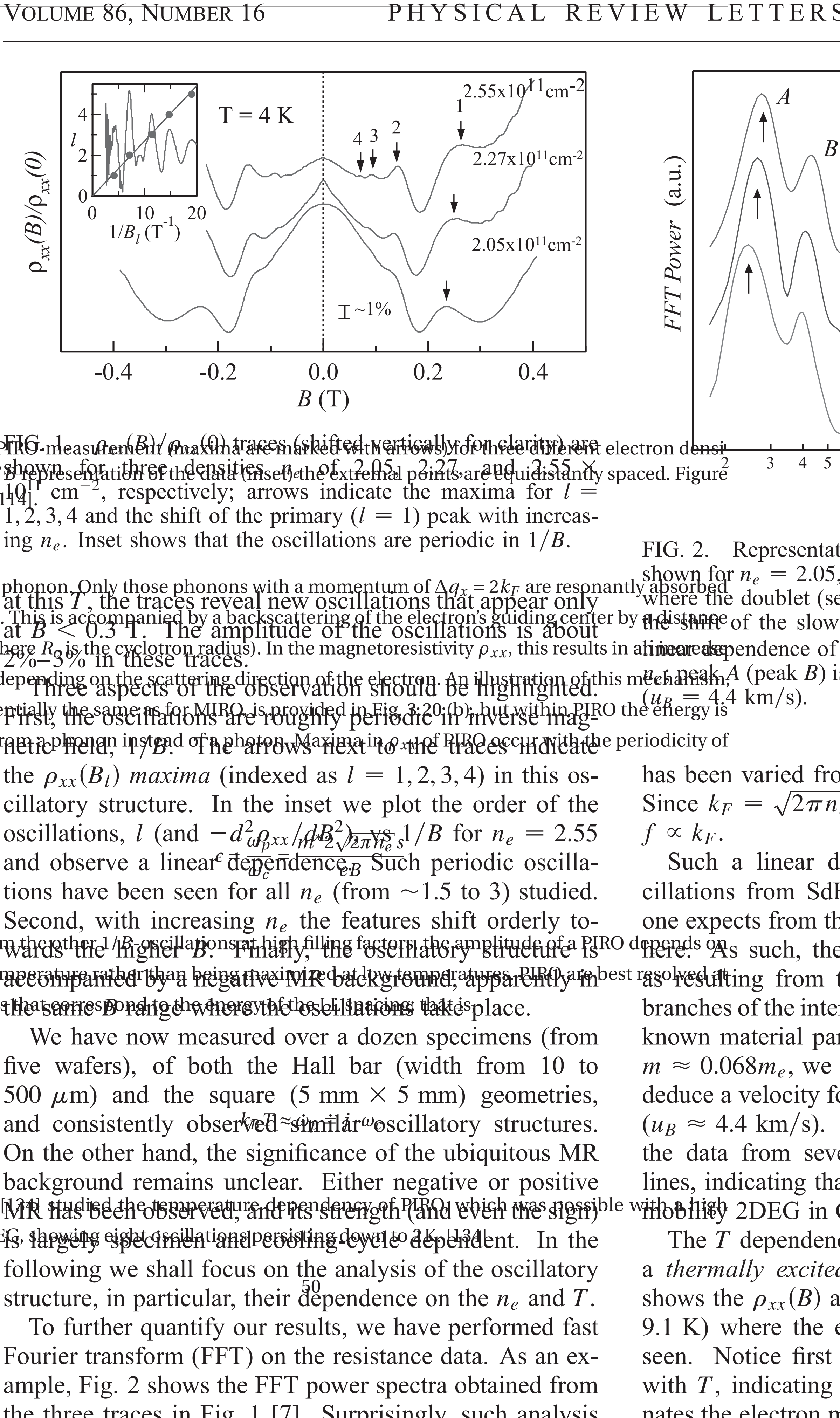

VOLUME 86, NUMBER 16 PHYSICAL REVIEW LETTERS

FIG. 1. $\rho_{xx}(B)/\rho_{xx}(0)$ traces (shifted vertically for clarity) are shown for three densities, n_e, of 2.05, 2.27, and 2.55 × 10^{11} cm^{-2}, respectively; arrows indicate the maxima for $l = 1, 2, 3, 4$ and the shift of the primary ($l = 1$) peak with increasing n_e. Inset shows that the oscillations are periodic in $1/B$.

at this T, the traces reveal new oscillations that appear only at $B < 0.3$ T. The amplitude of the oscillations is about 2%–3% in these traces.

Three aspects of the observation should be highlighted. First, the oscillations are roughly periodic in inverse magnetic field, $1/B$. The arrows next to the traces indicate the $\rho_{xx}(B_l)$ *maxima* (indexed as $l = 1, 2, 3, 4$) in this oscillatory structure. In the inset we plot the order of the oscillations, l (and $-d^2\rho_{xx}/dB^2$) vs $1/B$ for $n_e = 2.55$ and observe a linear dependence. Such periodic oscillations have been seen for all n_e (from ~1.5 to 3) studied. Second, with increasing n_e the features shift orderly towards the higher B. Finally, the oscillatory structure is accompanied by a negative MR background, apparently in the same B range where the oscillations take place.

We have now measured over a dozen specimens (from five wafers), of both the Hall bar (width from 10 to 500 μm) and the square (5 mm × 5 mm) geometries, and consistently observed similar oscillatory structures. On the other hand, the significance of the ubiquitous MR background remains unclear. Either negative or positive MR has been observed, and its strength (and even the sign) is largely specimen and cooling-cycle dependent. In the following we shall focus on the analysis of the oscillatory structure, in particular, their dependence on the n_e and T.

To further quantify our results, we have performed fast Fourier transform (FFT) on the resistance data. As an example, Fig. 2 shows the FFT power spectra obtained from the three traces in Fig. 1 [7]. Surprisingly, such analysis

FIG. 2. Representat
shown for n_e = 2.05,
where the doublet (se
the shift of the slow
linear dependence of
n_e; peak A (peak B) i
(u_B = 4.4 km/s).

has been varied fro
Since $k_F = \sqrt{2\pi n}$
$f \propto k_F$.
Such a linear d
cillations from SdH
one expects from th
here. As such, the
as resulting from t
branches of the inter
known material par
$m \approx 0.068m_e$, we
deduce a velocity fo
($u_B \approx 4.4$ km/s).
the data from seve
lines, indicating tha
mobility 2DEG in G
The T dependence
a *thermally excited*
shows the $\rho_{xx}(B)$ a
9.1 K) where the e
seen. Notice first
with T, indicating
nates the electron m

Figure 3.22: PIRO measurement (maxima are marked with arrows) for three different electron densities. In the $1/B$ representation of the data (inset) the extremal points are equidistantly spaced. Figure taken from [114].

propagating phonon. Only those phonons with a momentum of $\Delta q_x = 2k_F$ are resonantly absorbed by the 2DEG. This is accompanied by a backscattering of the electron's guiding center by a distance $\Delta Y = 2R_c$ (where R_c is the cyclotron radius). In the magnetoresistivity ρ_{xx}, this results in an increase or decrease depending on the scattering direction of the electron. An illustration of this mechanism, which is essentially the same as for MIRO, is provided in Fig. 3.20 (b); but within PIRO the energy is transferred from a phonon instead of a photon. Maxima in ρ_{xx} of PIRO occur with the periodicity of

$$\epsilon = \frac{\omega_p}{\omega_c} = \frac{m^* 2\sqrt{2\pi n_e}\, s}{eB} \tag{3.4.3.1}$$

Different from the other $1/B$-oscillations at high filling factors, the amplitude of a PIRO depends on the lattice temperature rather than being maximized at low temperatures. PIRO are best resolved at temperatures that correspond to the energy of the LL spacing; that is,

$$k_B T \approx \omega_p = l\,\omega_c \tag{3.4.3.2}$$

Hatke et al. [134] studied the temperature dependency of PIRO, which was possible with a high mobility 2DEG, showing eight oscillations persisting down to 2 K. [134]

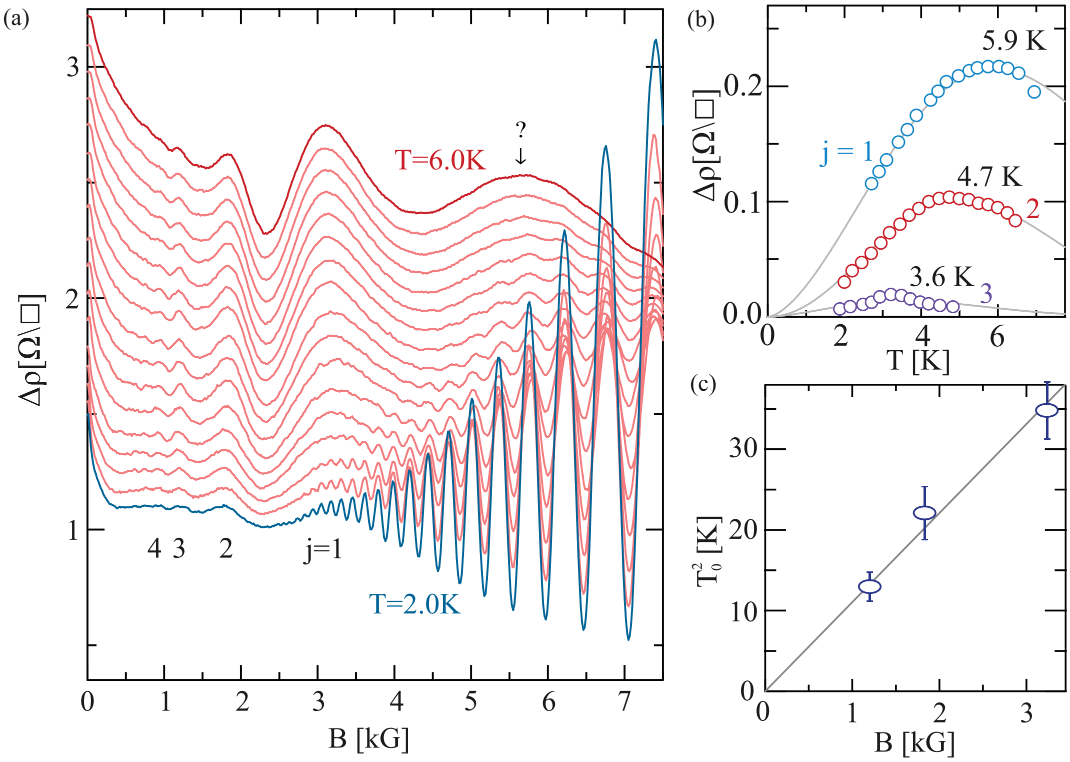

Figure 3.23: (a) PIRO superimposing the magnetoresistivity for temperatures between 2 K and 6 K. (b) The temperature evolution of the PIRO amplitude for $j = 1, 2, 3$. (c) The temperatures at which the respective maximum has the highest amplitude is depicted vs. the magnetic field at which the maximum occurs, conveying an interaction-induced broadening of the LLs. Figure taken from [134].

Fig. 3.23 (a) shows the magnetoresistivity traces performed at different sample temperatures between 2.0 K and 6.0 K. The first PIRO maximum occurs slightly before the onset of the SdHo at 300 mT. As the temperature is increased, the amplitude of each maximum increases but reduces with further increases in temperature, as shown for the first three PIRO maxima in part (b) of Fig. 3.23. The comparison of the amplitude of the first three maxima (see Fig. 3.23 (c)) with the respective temperature conveyed a $\sqrt{B}$ scaling [134, 135]. This suggests that the suppression of PIRO at high temperatures is caused by the interaction-induced broadening of LLs.

From the slope of the ρ_{xx} vs. $1/B$ representation, the sound velocity can be extracted if the effective mass m^* and the electron density n_e are known (see 3.4.3.1). In Fig. 3.24 (b), the number of the maximum is depicted with respect to the inverse magnetic field at 3.5 K. From the slope k of this linear fit, the sound velocity was determined to be $s = 3.4\,\mathrm{km/s}$ with the following relation:

$$s = k \cdot \frac{e}{2\sqrt{2n_e\pi}\,m^*} \tag{3.4.3.3}$$

Similar to MIRO, the PIRO exhibit a phase that is predicted to be $\varphi = -1/4$. [136] This was experimentally confirmed in 2011 [123] although the PIRO phase is not expected to be universal. Reasons for deviations from $\varphi = -1/4$ are dependencies on the relevant phonon mode, crystal plane, and the width of the sample. [136, 137] In Fig. 3.24 [123], an experimental analysis of PIRO is illustrated. The oscillatory part of the magnetoresistivity $\delta\rho$ is shown in part (b) of the figure (i.e., after the background is subtracted). Besides the determination of the sound velocity from the slope, φ can be found from the intercept of the linear fit. Hatke et al. found $\varphi = -1/4$ for different samples with different electron densities but the same sample geometry.

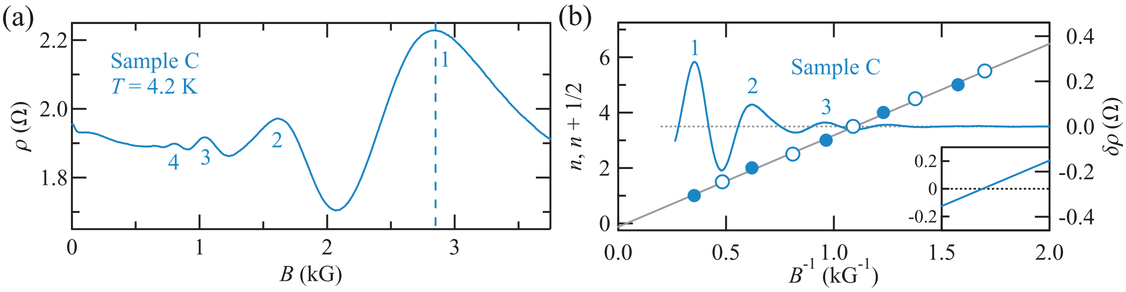

Figure 3.24: (a) Exemplary magnetoresistivity trace with the first four PIRO maxima marked by the respective integer. (b) The right y-axis shows the oscillatory part of the magnetoresistivity, and the left axis represents the maxima using even and minima using odd numbers vs. $1/B$. From the slope of the linear fit (in gray), s can be determined and φ from the intercept. Figure taken from [123].

CHAPTER 4

EXPERIMENTS AND SIMULATIONS ON DENSE RETROREFLECTIVE 2DLG

The results from the Ehrenfest wind-tree model (EWT), detailed in subsection 3.3.4 left many unsolved questions with regard to the anomalous transport in heterogeneous media.

As prior studies on the EWT focused on low obstacle densities, the question of how sub-diffusion evolves at intermediate and high obstacle densities remains open. Moreover, it is not clear how the sub-diffusive behavior changes if the obstacles are additionally randomly oriented. A insightful tool for investigating the diffusivity of the system is a perpendicular magnetic field. This changes the tracer particles' trajectories from straight lines to a circular shape as it holds for the cyclotron radius: $r_c \propto B^{-1}$. The main essential of the EWT is the configuration of the retroreflective cone (see Fig 3.17 (c)). Therefore, to study the retroreflectivity in the dense regime, the shape of an retroreflective cross (RC) was chosen in the MD simulation and experiment because the effects were expected to be more pronounced compared with square obstacles. One RC is formed by four retroreflective cones with a $\pi/4$-symmetry. The RC is composed of two rectangles, each measuring 450 nm × 2 µm.

An electron beam microscopy image of a 2DLG comprising equally oriented RCs is shown in Fig 4.1. The upper-right inset depicts an RC with its electronic dimensions, which means that a depletion length of 75 nm is taken into account (based on the estimations in [93]). The upper-left inset depicts a single RC at an angle of 45°, thereby providing etch depth information. Here, the lithographic dimensions are given. Two approaches exist to investigate the transport behavior of a retroreflective 2DLG, namely experiments and simulations.

The focus of the presented studies lies in intermediate and large RC densities. In this area, no investigations have thus far been conducted. Both implementations are discussed in the following two sections and the results thereof are presented and compared. The source code on which the results presented within this thesis are based was written and provided by Jürgen Horbach, René Lohman and Nima Siboni. The results presented in this chapter are under review for publication [25].

4.1 Experimental implementation of a 2DLG formed by retroreflective crosses

For both the experiment and implementation of the 2DLG in an MD simulation, the magnetotransport studied for randomly and equally oriented RCs at different obstacle densities.

Within the experimental implementation, the number of measurement fields comprising different obstacle densities is restricted to the sample dimensions. The host crystal of the sample is a GaAs/$Al_{0.3}Ga_{0.7}As$ heterostructure with a 2DEG 150 nm below the surface. After illumination with an infrared diode, the samples have a density of $2.5 \times 10^{15}\,\mathrm{m}^{-2}$ and a typical electron mobility of $340\,\mathrm{m}^2/\mathrm{Vs}$. This corresponds to a mean free path of $l_{\mathrm{mfp}} = 31\,\mu\mathrm{m}$. These values deviate slightly depending on the cooldown cycle. From the envelope of the SdHo, the quantum scattering time of $\tau_q = 2.5\,\mathrm{ps}$ is extracted, which corresponds to a length of $l_q = 530\,\mathrm{nm}$. The fact that $l_q < l_{\mathrm{mfp}}$ indicates that remote donors situated in the delta-doping layer are the main source of the scattering potential in the pristine sample.

In the experiment, the resistivity along the current direction ρ_{xx} and perpendicular to it ρ_{xy} are the accessible observables. From $\rho_{xx}(B)$ and $\rho_{xy}(B)$, the conductivity can be calculated with the following relation: $\sigma_{xx} = \rho_{xx}/(\rho_{xx}^2 + \rho_{xy}^2)$.

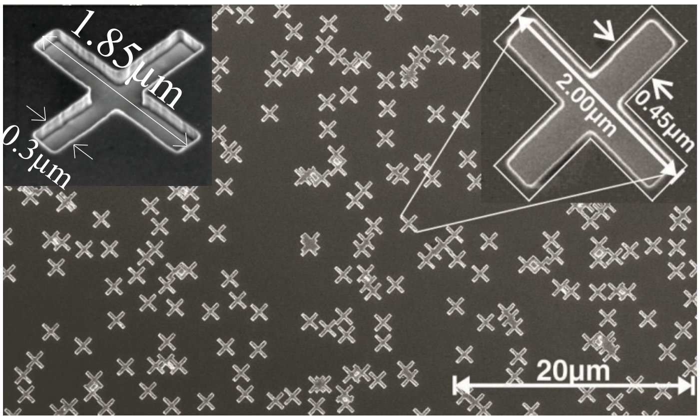

Figure 4.1: Electron scanning microscopy image of a sample with equally oriented RCs with $n^* = 0.2$. The upper-right inset is a zoom-in of a single RC with electronic dimensions (i.e., a lateral depletion length of 75 nm is assumed). The upper-left inset depicts a single RC scanned at an angle of 45°. Here the lithographic dimensions are given. Figure from [25].

Different to an MD simulation, the sample in the experiment has boundaries that offer another scattering channel, although this contribution is expected to be small compared with the scattering at the RC obstacles. Additionally, scattering at phonons and intrinsic defects may cause slight deviations of the measurement traces.

Details of the sample preparation were provided in Section 2.1, and the measurement principle was detailed in Section 2.2.

4.1.1 Sample designs

Four samples were prepared, on which 2DLGs comprising RCs were patterned. Each sample hosts five measurement fields with a Hall bar width of $w = 100\,\mu\mathrm{m}$. The voltage probes (width = $10\,\mu\mathrm{m}$) are spaced by $100\,\mu\mathrm{m}$ in the longitudinal and perpendicular direction with respect to the applied source-drain current. One measurement field is left unpatterned and is the reference, and the other four are patterned using electron beam lithography with 2DLGs composed of RCs. The obstacle densities increase from the left to the right measurement field. Values of n^* are summarized in the table below.

Thus, n^* is defined as the fraction of the area covered by the RCs in the absence of mutual overlap. As for the other 2DLGs measured within this thesis, mutual overlap of the obstacles is allowed.

Two of the four samples host a 2DLG with equally oriented RCs (i.e., the cone opening of the RC is in the direction of the source-drain current). The other two samples are patterned with RCs that have a random orientation. The RCs with equal and random orientation are prepared with a lithographic size of 300 nm (short edge) and 1850 nm (long edge), respectively. A depletion length of ≈ 75 nm is assumed, based on [93], and thus one rectangular of an RC has the electronic dimensions $450\,\mathrm{nm} \times 2000\,\mathrm{nm}$. Fig. 4.1 depicts a scanning electron microscopy (SEM) image of the equally oriented RCs with $n^* = 0.2$. The dimensions given in the upper right zoom-in of a single RC are the electronic lengths, taking the depletion length into account. The dimensions in the 45°-representation are the lithographic dimensions.

The randomly and equally oriented RCs were also prepared with smaller dimensions (the remaining two samples). This means they are lithographically patterned with rectangles of $150\,\mathrm{nm} \times 850\,\mathrm{nm}$, resulting in an electronic size of $300\,\mathrm{nm} \times 1000\,\mathrm{nm}$. The inset of Fig. 4.2 shows how the RC dimensions are defined. Because of the two different sizes, the number density n_s and dimensionless density n^* differ, values of which are summed up in table 4.1:

RC size (lithographic dimensions)	n_s ($10^{12}/\mathrm{m}^2$)	n^*
$d = 850\,\mathrm{nm}$, $b = 150\,\mathrm{nm}$	0.25	0.13
	0.5	0.26
	0.75	0.38
	1	0.51
$d = 1850\,\mathrm{nm}$, $b = 300\,\mathrm{nm}$	0.0625	0.1
	0.125	0.2
	0.1875	0.3
	0.25	0.4

Table 4.1: Sample parameters of the RC-2DLGs.

4.1.2 Experimental results

Fig. 4.2 depicts the experimental magnetoconductivity of the 2DLG comprising equally oriented RCs ($n^* = 0.3$, $d = 1850\,\mathrm{nm}$). As for the case of a 2DLG formed by circular obstacles, a conductivity maximum (here at approx. 80 mT) is observable. This maximum, which is marked with (2) in Fig. 4.2, is caused by the superdiffusive transport on short time scales, which originate from a guided transport of the tracer particles' trajectories along the contour of the Lorentz gas obstacles. The electron skips from one obstacle assembly to the next, which was detailed in Subsection 3.3.3.
Additionally, at low magnetic fields in the range of 0 to 50 mT at approximately 35 mT, a local maximum (marked with (1) in Fig. 4.2) is visible. As the temperature increases, this local maximum vanishes at 4 K, whereas the other maximum (2) remains up to 16 K. This indicates that the mechanism connected to (1) requires larger length scales at which the electron is able to move ballistically. One possible mechanism causing the local maximum (1) is that the electron trajectory is bent out of the area formed by two opposite RCs. At zero magnetic field, the electron is reflected back and forth between the two RCs, whereas for the trajectory bending at increased magnetic fields, the magnetic fields are high enough for the electron to leave this area.
The EWT predicts that the conductivity at $B = 0$ is determined by anomalous diffusion, because the mean-squared displacement does not grow linearly in the long-time limit. Although real 2DEG samples exhibit very long mean free paths in the range of tens of micrometers, there still exist many background scattering events. These cause the conductivity at zero magnetic field to be measurable because they superimpose on the zero-field case of the EWT. To observe the nonexistence of the conductivity, straight trajectories (seen in the simulation in Section 4.2) are required. This explains the regular behavior as B approaches zero.

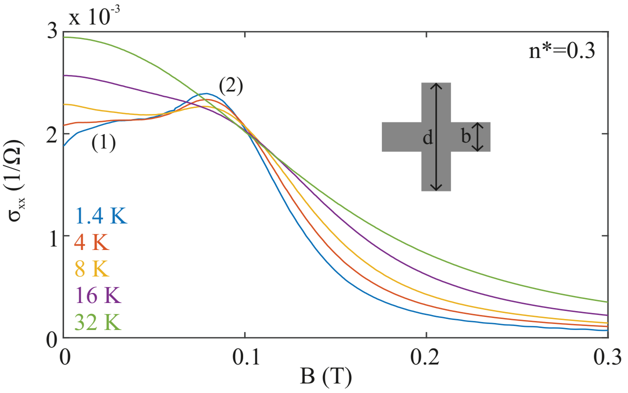

Figure 4.2: Magnetoconductivity of the equally oriented RC ($n^* = 0.3$, $d = 1850\,\mathrm{nm}$) for temperatures between 1.4 K and 32 K. (2) is the conductivity maximum caused by a guided transport along the 2DLG cluster contour as detailed in [15]. (1) is a local maximum caused by breaking of the corridor effect. As the temperature increases more dynamic scattering is introduced, which already affects (1) at 4 K, while (2) is still visible at 16 K. Figure from [25].

Fig. 4.3 shows the conductivity at $B = 0$ for the different obstacle densities of the equally oriented RCs with $d = 1850\,\mathrm{nm}$. The zero-field conductivity is multiplied with n^{*2} for better visibility of the differences in the traces, which correspond to different n^*. Furthermore, σ_{xx} increases with increasing temperatures. This effect is most pronounced for the highest n^*. This phenomenology indicates that the retroreflection is not only enhanced by the number of obstacles but also by a decreased temperature (which means a longer mean free path of the electron). Moreover, this indicates that background effects are less important as n^* is increased.

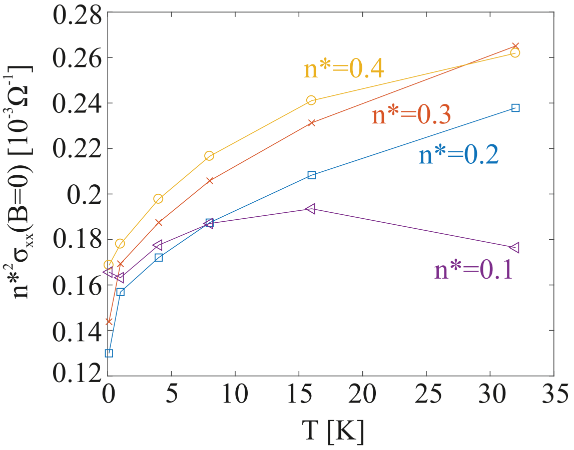

Figure 4.3: Temperature dependency of $n^{*2}\sigma_{xx}$ at $B = 0$ for the 2DLG formed by equally oriented RCs ($d = 1850\,\mathrm{nm}$) for the four n^*. As the temperature increases, σ_{xx} increases, indicating that background scattering caused by phonons superimposes on retroreflection.

Weak localization [62, 63] is an effect that reduces the conductivity at zero magnetic field. A decreasing temperature increases weak localization. Here, weak localization can be excluded to cause the described phenomenology. Fig. 4.4 depicts the evolution of the magnetoconductivity at temperatures below 1 K. From the SdHo (see the inset of Fig. 4.4) shown in the interval from 270 mT to 300 mT, the increased temperature can be observed to reduce the amplitude. At zero magnetic field, a slight modification of the magnetoconductivity exists, which is barely visible. On the other hand, the local maximum at 35 mT does not change its amplitude as the temperature is varied in the investigated temperature interval. This indicates that the effect causing the local maximum is not related to weak localization.

In addition to the equally oriented implementation of RC-2DLG, samples with randomly oriented RC-2DLG were also produced, the results of which are presented for $n^* = 0.3$, $d = 1850\,\mathrm{nm}$ in Fig. 4.5. The inset is an electron beam microscopy image of the sample. Here, the phenomenology resembles the case of equally oriented RC obstacles. The local maximum (marked with (1)) is less pronounced, indicating that the contribution of retroreflection decreases because the obstacle orientation is random.

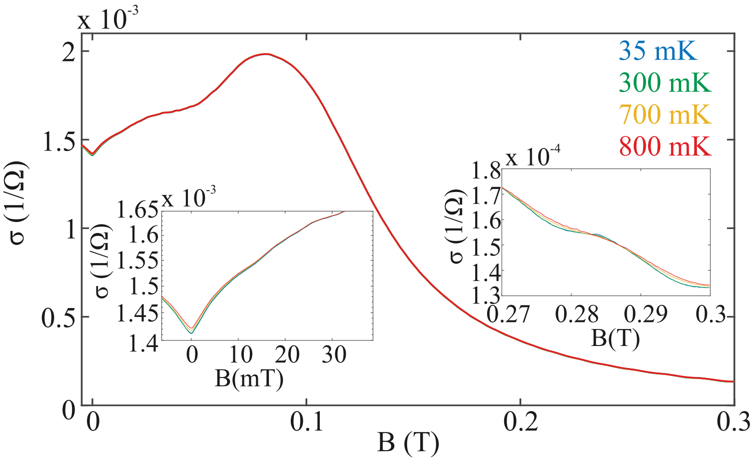

Figure 4.4: Temperature evolution of the equally oriented RC-2DLG ($n^* = 0.3$, $d = 1850\,\text{nm}$) at sub-Kelvin temperatures. The inset on the right reveals that the SdHo amplitude reduces with increasing temperature, while the trace around zero B and around the local maximum at 35 mT remains unchanged, proving that the described observations are not caused by weak localization. Figure from [25].

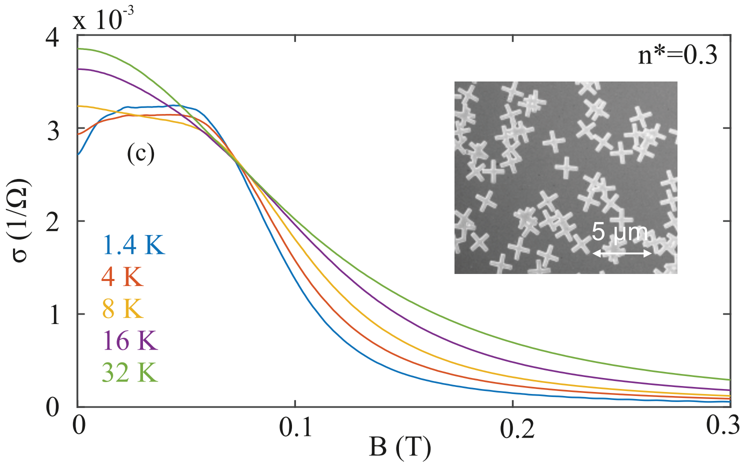

Figure 4.5: Magnetoconductivity of the randomly oriented RCs with $n^* = 0.3$ and $d = 1850\,\text{nm}$. The inset depicts an electron beam microscope image of the sample. Figure from [25].

The samples with $d = 850\,\text{nm}$ show the same phenomenology as the samples with larger obstacle size (i.e., $d = 1850\,\text{nm}$; see Fig. 4.6). However, one difference is that at low n^*, comparing $n^* = 0.13$ ($d = 850\,\text{nm}$) and $n^* = 0.1$ ($d = 1850\,\text{nm}$), the magnetoconductivity of the measurement field with smaller obstacles shows a decrease of the zero-field value as the temperature is increased, measurements of which are presented in Fig. 4.6 (a). This is the opposite behavior of the sample with $n^* = 0.1$, $d = 1850\,\text{nm}$ (see part (b) of Fig. 4.6). Here, the magnetoconductivity increases at zero magnetic field as the temperature increases, which is caused by the reduction of retroreflection caused by the

phonon contribution.
Therefore, it can be stated that larger RC obstacles show a larger contribution of retroreflection in magnetoconductivity.

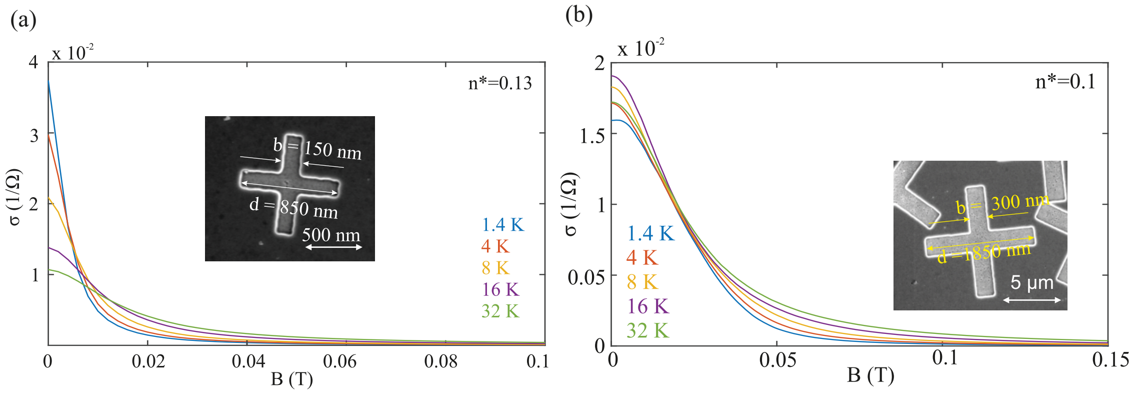

Figure 4.6: Magnetoconductivity of the RC-2DLG for the smaller obstacles (a) and larger obstacles (b) for similar $n^* \approx 0.1$. The lithographic dimensions are provided in the insets. At $B = 0$ the conductivity decreases in (a), contradicting the retroreflection contribution. By contrast, the 2DLG formed by the larger RCs (b) exhibits increasing conductivity at zero magnetic field with increasing temperature. This indicates that retroreflection becomes more pronounced with larger obstacles. Figure from [25].

The remaining measurement results on RC-2DLG are presented in the Appendix (Chapter 8).
Summarizing the experimental results on 2DLG comprising RCs, it can be stated that although the conductivity at zero magnetic field is measurable, the magnetoconductivity traces show signatures proving the retroreflection of electrons within the obstacle matrix. This effect is enhanced by increased obstacle densities and decreased temperatures. The samples with equally oriented RCs show a more pronounced local maximum, indicating that the orientation of the obstacles influences the extent of the retroreflective effect.

4.2 MD-simulation of a 2DLG formed by RCs

4.2.1 Simulation setup

The simulation and corresponding numerical implementation were provided by René Lohmann, Nima Siboni and Jürgen Horbach. For a detailed description of the simulation, the reader is referred to [138].
For each simulation run, RCs that are either equally or randomly oriented are arbitrarily distributed within the simulation box. Thus, they are allowed to overlap such that a 2DLG is formed. The simulation box has a size of $200\,k \times 100\,k$. In the simulation, lengths are scaled to $k = 1\,\mu\text{m}$. The conversion to other quantities from simulation to experiment is detailed in Subsection 4.2.2. The box boundaries are periodic, which means a particle that exits the box enters at the opposite side.

The tracer particles are randomly placed in the empty space between the obstacles. Each tracer starts its trajectory in a random direction, while the amount of velocity is maintained at a constant value. Usually 500 tracer particles are simulated for one 2DLG configuration. This is repeated and calculated for 2000 LG-host structures of different configurations but with the same n^*. This approach improves the ensemble average. The trajectories of the 500 tracer particles are calculated one after the other following their ballistic motion between collisions. Here, an event-driven type of implementation is used: particles are moved according to their cyclotron motion until they approach an obstacle. The change in the particle's direction is evaluated at each elastic collision until the tracer particle collides the next time. This is more advantageous with regard to the calculation time compared with evolving the system through discretized equations of motions with fixed timesteps Δt.

Another parameter is the bending of the tracer particle's trajectory, determined by its cyclotron radius R_c. In the simulation, the magnetic field is defined as $\tilde{B} = 1/R_c$.

At the end of each simulation run, the average of the mean square displacement (MSD) is calculated, defined as follows:

$$\delta r^2(t) = \left\langle (\vec{r}(t) - \vec{r}(0))^2 \right\rangle \tag{4.2.1.1}$$

that is, averaged over the number of particles and 2000 independent configurations for each $\tilde{B}$ (indicated by $\langle ... \rangle$). If the transport is diffusive in its asymptotic behavior, the diffusion coefficient D can be determined from the long-time limit of the MSD:

$$D = \lim_{t \leftarrow \infty} \frac{4d\delta r^2(t)}{dt} \tag{4.2.1.2}$$

The experimental conductivity σ_{xx} and the numerically determined D are proportional to each other and thus directly comparable (see Subsection 4.2.2).

For comparability with the experimental system, the dimensions in the simulation are chosen such that they correspond to the experimental conditions. The RCs in the simulation have the same geometry and dimension as those in the experiment. The RCs with $d = 1850\,\text{nm}$ are chosen for the simulation because they showed the highest contribution of retroreflection in the experimental magnetoconductance (Subsection 4.1.2). One of the two rectangles that an RC is composed of has the dimensions $2k \times 0.45k$. Here, the experimental lateral depletion length of 75 nm is taken into account. Both configurations of equally and randomly oriented RCs are implemented in the simulation.

4.2.2 Conversion from simulation to experiment

For comparability, it is important to know the conversion factors from simulation to experimental units. The simulation lengths of any object such as the RCs or simulation box are scaled to $k = 1\,\mu\text{m}$. The velocity of each tracer particle $\vec{v}$ has a random direction, while its magnitude is constant, fixed to the Fermi velocity, and set to one in the simulation: $v_F = |\vec{v}| = 1$. Quantities that do not directly enter the simulation are set to one for simplicity. These are the electron density n_e, the elementary charge e, and the effective mass m^*. All other conversions follow from these specifications and are summarized in table 4.2:

quantity	relation	conversion simulation → experiment
length Δs	$\Delta s_{\text{exp}} = k\Delta s_{\text{sim}}$	$\Delta s_{\text{exp}} = 10^{-6}\Delta s_{\text{sim}}$
time Δt	$\Delta t_{\text{exp}} = \frac{k}{\vert v_F\vert}\Delta t_{\text{sim}}$	$\Delta t_{\text{exp}} = 4.63\cdot 10^{-12}\Delta t_{\text{sim}}$
velocity v	$v_{\text{exp}} = \vert v_F\vert \cdot v_{\text{sim}}$	$v_{\text{exp}} = 2.16\cdot 10^{5}\cdot v_{\text{sim}}$
mass m	$m_{\text{exp}} = \vert m^*\vert m_{\text{sim}}$	$m_{\text{exp}} = 6.10\cdot 10^{-32}\cdot m_{\text{sim}}$
charge q	$q_{\text{exp}} = \vert e\vert q_{\text{sim}}$	$q_{\text{exp}} = 1.602\cdot 10^{-19}\cdot q_{\text{sim}}$
magnetic field B	$B_{\text{exp}} = k\cdot\frac{\vert m^*\vert}{\vert e\vert}\cdot B_{\text{sim}} = k\cdot\frac{\vert m^*\vert}{\vert e\vert}\cdot\tilde{B}$	$B_{\text{exp}} = 8.23\cdot 10^{-2}\cdot B_{\text{sim}} = 8.23\cdot 10^{-2}\cdot\tilde{B}$
diffusion coefficient D	$D_{\text{exp}} = \frac{\vert v_F\vert}{k}D_{\text{sim}}$	$D_{\text{exp}} = 2.1\cdot 10^{-1}\cdot D_{\text{sim}}$
conductivity σ	$\sigma_{\text{exp}} = \frac{\vert v_F\vert\vert n_e\vert e\vert^2\vert}{k\vert m^*\vert}\sigma_{\text{sim}}$	$\sigma_{\text{exp}} = 2.26\cdot 10^{8}\cdot\sigma_{\text{sim}}$

Table 4.2: Conversion constants from simulation to experiment.

The constants that appear here are: $|v_F| = 2.1\cdot 10^5\,\text{m/s}$, $|m^*| = 6.1\cdot 10^{-32}\,\text{kg}$, $|e| = 1.602\cdot 10^{-19}\,\text{C}$. A dimensionless magnetic field $\tilde{B} = B/B_0$ is used to present the results from the simulation. It is scaled to $B_0 = m^* v_F/(ek) \approx 0.0823\,\text{T}$. The diffusion coefficient D_{sim} is directly proportional to the experimental conductivity σ_{exp}:

$$\sigma_{\text{exp}} = \frac{n_e e^2}{m^* {v_F}^2} D_{\text{sim}} = (0.486\cdot 10^{-2}\Omega^{-1}) D_{\text{sim}} \tag{4.2.2.1}$$

Therefore, it is possible to quantitatively compare the simulation and experimental results.

4.2.3 Result of MD simulations

Fig. 4.7 (b)-(f) depicts typical trajectories of an electron in a RC-2DLG, obtained from the simulation. The first panel (a) depicts the dimensions of a single RC, which is consistent with the dimensions under experimental conditions. For the case of $\tilde{B} = 0$, the retroreflective character (i.e., many returns to an original position) is observed for equally (b) and randomly oriented RCs (c). For both cases it is visible that the tracer particle experiences many backreflections caused by the retroreflective shape of the obstacles. Because of this, the particle travels for a longer time in the area formed by two opposite RCs.

The lower part of Fig. 4.7 depicts trajectories for the equally oriented RCs at different $\tilde{B}$. For $\tilde{B} = 0.125$

or $r_c = 8$ (d), the retroreflectivity is still observable, although it is disturbed by the bending of the trajectory. As $\tilde{B}$ is increased to $\tilde{B} = 1$ (part (e) of Fig. 3.7), the tracer is guided along the obstacle edges, skipping from one assembly to the next, which leads to a maximum in conductivity. The system approaches a localized state with further increasing magnetic fields, depicted in part (f) for $\tilde{B} = 2.5$. Here the tracer particle's cyclotron radius is small and thus it skips around an accumulation of RCs. Both cases (e) and (f) are discussed in Subsection 3.3.3.

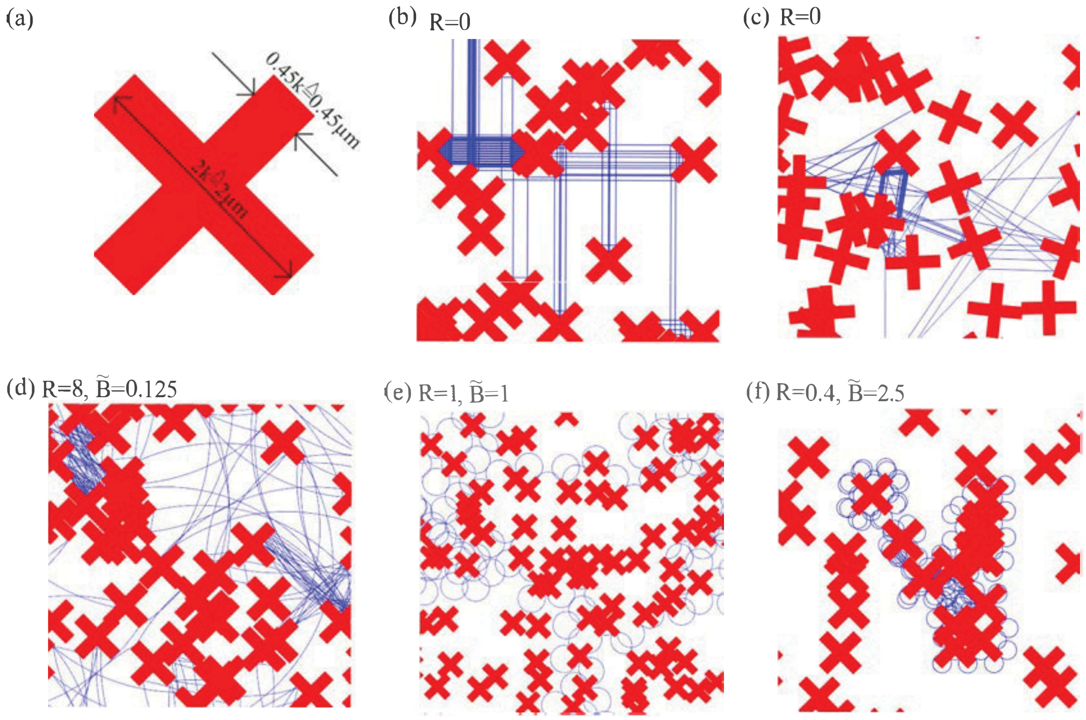

Figure 4.7: (a) Dimensions of a single RC in experimental and simulation units. (b)-(f) Trajectories (blue) of a tracer particle in local configurations of 2DLGs comprising RCs. For (b) showing equally oriented RCs at $\tilde{B} = 0$ and (c) showing randomly oriented RCs at $\tilde{B} = 0$ many retracing parts of the trajectories are visible. For low-magnetic fields ($\tilde{B} = 0.125$) and equally oriented RCs depicted in (d) this character remains. (e), (f) Trajectories for higher $\tilde{B}$ (the phenomenology of which is discussed in chapter 3.3.3).

Here, the focus lies in the subdiffusive transport in the long-time limit of the cases (b)-(f). Therefore, the MSD (eq. 4.2.1.1) is analyzed. Fig. 4.8 depicts the simulation results of the conductivity obtained from the long-time limit of the derivative of the MSD (eq. 4.2.1.2 and eq. 4.2.2.1). The conductivities are presented vs. the magnetic field $\tilde{B}$ in a double logarithmic plot.

Comparing the n^* traces, σ can be seen to reduce as the obstacle density increases. There is a regime with $\tilde{B} < 0.01$ for all traces, in which a power law qualifies the dependency of the conductivity on the magnetic field; that is, $\sigma_{xx} \propto \tilde{B}^{\delta}$. This behavior was found for three to four orders of magnitude in $\tilde{B}$. The solid lines are linear fits to the data, where the slope is δ, that is represented against the dimensionless obstacle density n^* for both cases of orientation in the inset. From this, for the randomly oriented RCs, one finds a slightly decreasing, almost constant, exponent with respect to n^* with a value of $\delta \approx 0.09$. By contrast, for the equally oriented RCs, δ increases with n^* from 0.15 to 0.21. This behavior is caused by trajectories dominated by backreflection. The zero-field case, discussed later, is thus of a special nature and inflects on the behavior at low magnetic fields.

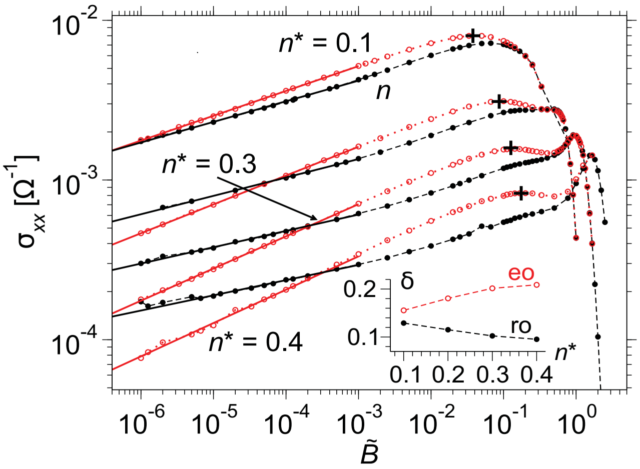

Figure 4.8: Conductivity $\sigma(\tilde{B})$ for equally oriented (red open circles) and randomly oriented RCs (black closed circles) for different n^*. Marked by black crosses are the positions of a local maximum in σ_{xx} (also visible in experiment). The linear fits (solid lines) prove a power law of $\sigma \propto \tilde{B}^{\delta}$. The exponent δ of each fit is depicted in the inset vs. the corresponding n^*. While δ increases with n^* for the equally oriented configuration, it is almost constant for the case of randomly oriented RCs. Figure from [25].

For all n^*, a local maximum for equally oriented RCs and a shoulder for randomly oriented RCs marked by black crosses can be identified. At this magnetic field, a qualitative change in tracer particle transport occurs. $\tilde{B}_m$ is in the range of 0.1, corresponding to a cyclotron radius of 10 k. At this magnetic field, the retroreflective character of the trajectories gets lost because the trajectory bending is sufficient for the tracer particles to exit a retroreflective corridor formed by two or several RCs.

The as-described local maximum is different to the maximum following at higher magnetic field values, such as at $\tilde{B} = 1$ for the $n^* = 0.3$ trace (valid for both configurations). Here, maximal diffusion is caused by the guided transport along the edges of the 2DLG; see Subsection 3.3.3 and [15] for a detailed explanation.

Most pronounced is the retroreflective influence on the tracer particles' transport properties for the zero-$\tilde{B}$ case. For the zero-$\tilde{B}$ case, Fig. 4.9 (a) depicts the MSD in units of k^2 for all dimensionless densities and both orientations. In part (b) of the figure, the local exponent γ is defined as follows:

$$\gamma = \frac{d \log(\delta r^2(t))}{d \log(t)} \tag{4.2.3.1}$$

which is presented against $\log(t/t_0)$. Here $t_0 = 4.6\,\mathrm{ps}$, which corresponds to the time a tracer particle requires to walk the distance k in the simulation. In case γ approaches 1 for the long-time limit, it is possible to determine a diffusion coefficient. Here, for the case of randomly oriented RCs, all n^* saturate to approx. 0.73, which means that the transport is subdiffusive and D_{sim} cannot be determined. The MSD grows in time with the relation $\delta r^2(t) \propto t^\gamma$. Part (c) of Fig. 4.9 depicts γ against $\log(t/t_0)$ for the equally oriented RCs. Here γ is below 1 for all n^*, showing again that the transport is subdiffusive for long times and no diffusion constant can be determined. Moreover, γ depends on n^*. It decreases with increasing n^*, which is consistent with the predictions from [111].

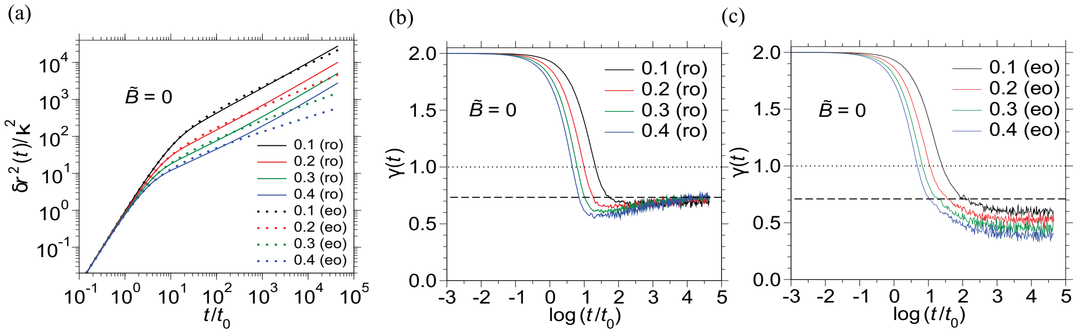

Figure 4.9: (a) MSD for $\tilde{B} = 0$ for all n^* and both orientations in units of k^2. (b) The exponent $\gamma(t)$ vs. $\log(t/t_0)$, showing that for the random orientation γ saturates to approx. 0.7 and thus D cannot be defined. (c) The same representation as (b) but for the equally oriented RCs; γ decreases with increasing n^* and is in the subdiffusive regime for all densities. Figure from [25].

Fig. 4.10 shows the exponent γ for all densities n^* in the long-time limit for $\tilde{B} = 0$. For high n^*, γ saturates to approximately 0.73 for the case of randomly oriented RCs. Equally oriented RCs show that the exponent γ decreases with increasing n^*. Only if the local exponent reaches $\gamma = 1$ in the long-time limit can a diffusion coefficient be determined, which is not valid for any of the $\tilde{B} = 0$ cases. This indicates that a diffusion constant $D(\tilde{B} = 0)$ does not exist and the transport is anomalous. Figure 4.11 depicts the derivative of the MSD $(d\delta r^2(t)/dt)$ against time (t/t_0) for $n^* = 0.2$, from which the diffusion constant can be determined (see eq. 4.2.1.2). The case for $\tilde{B} = 0$ is special because for long time scales the trace does not saturate to a constant value from which D could be determined. This is visible for both orientations (zero-field case drawn in black) for (a) randomly and (b) equally oriented RCs.

The trace shows a maximum at time τ_m for all n^* and all orientations. Fig. 4.12 (b) presents τ_m/t_0 against $1/n^*$ for equally (red) and randomly oriented RCs (black). From this representation it is clear that the time at which the maximum in the derivative of the MSD occurs scales inversely with the dimensionless obstacle density n^*.

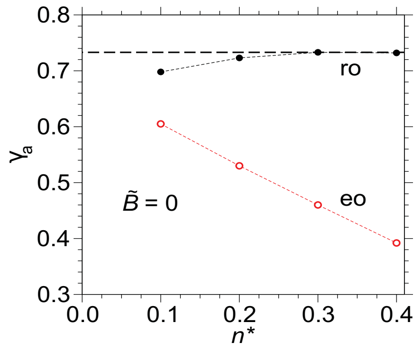

Figure 4.10: Asymptotic exponent γ i.e. $\gamma = \lim_{t\leftarrow\infty}\gamma(t)$ vs. n^* for both orientations and $\tilde{B} = 0$. For randomly oriented RCs, γ saturates to approx. 0.73, whereas it monotonously decreases for equally oriented RCs as n^* increases. Figure from [25].

Once a magnetic field is introduced to the simulation, D can be determined. All traces follow up to a time τ_B exactly the trace of the zero-field case, where τ_B decreases with increasing $\tilde{B}$. After τ_B all traces quickly reach a constant value, which corresponds to $4D/(kv_F)$.

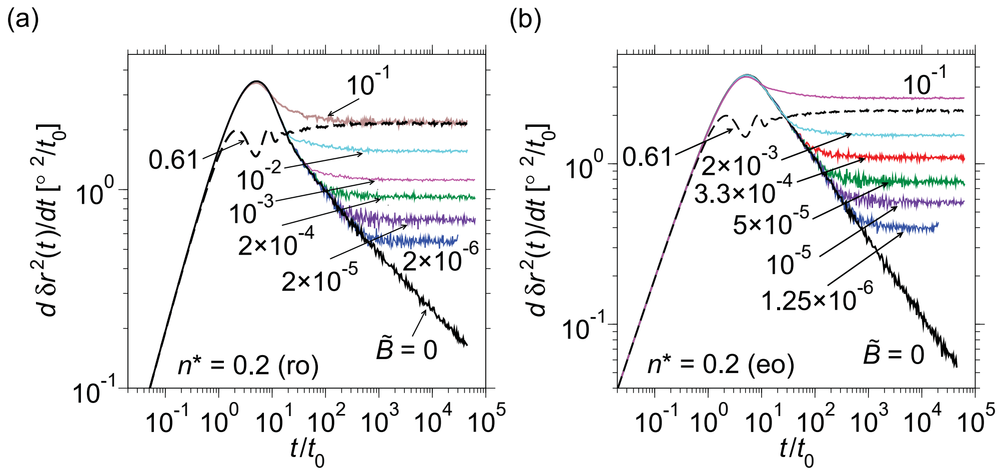

Figure 4.11: (a) Derivative of the MSD for the randomly oriented RCs vs. t/t_0 for $n^* = 0.2$ for different $\tilde{B}$. In black, the case for $\tilde{B} = 0$ shows that no diffusion coefficient can be defined. Up to $\tilde{B} \approx 0.1$, the traces follow the $\tilde{B} = 0$ trace. After the time τ_B the traces deviate from the $B = 0$ trace. τ_B reduces with $\tilde{B}$. (b) The same representation as (a) but for the case of equally oriented RCs. The qualitative behavior is the same as in (a). Figure from [25].

Once $\tilde{B}$ increases to a level such that $\tau_m < \tau_B$ does not hold anymore, the behavior of the derivative of the MSD changes qualitatively. For $n^* = 0.2$, this occurs at $\tilde{B} \approx 0.09$. In Fig. 4.11 this is exemplified for $\tilde{B} = 0.1$. For low times $t/t_0 < 1$, the traces are on top of each other, and once this regime elapses at approximately $t/t_0 = 1$, oscillations occur in the derivative of the MSD for three orders of magnitude in time. This indicates that the increased $\tilde{B}$ causes superlinear transport in this time interval. This behavior is observed for both orientations (see parts (a) and (b), black broken lines).

To summarize the results of the simulation, it was found that for the magnetotransport of tracer particles in a random 2D arrangement of randomly overlapping RCs, anomalous transport is caused by retroreflective trajectories. At zero magnetic field, the conductivity (or the diffusion coefficient) does not exist at any density, which is valid for the equally oriented and randomly oriented RCs. In the long-time limit of the derivative of the MSD, subdiffusive transport is seen. The exponent of the randomly oriented RCs approaches a value of $\gamma \approx 0.73$ at high densities. For equally oriented RCs, γ depends on n^*, and specifically it increases with n^*. Thus, the results suggest that for the equally oriented RCs, γ approaches a constant value for very low densities. This is one major difference to the EWT, where the obstacles are formed by squared obstacles. Here, γ is only slightly dependent on n^*.

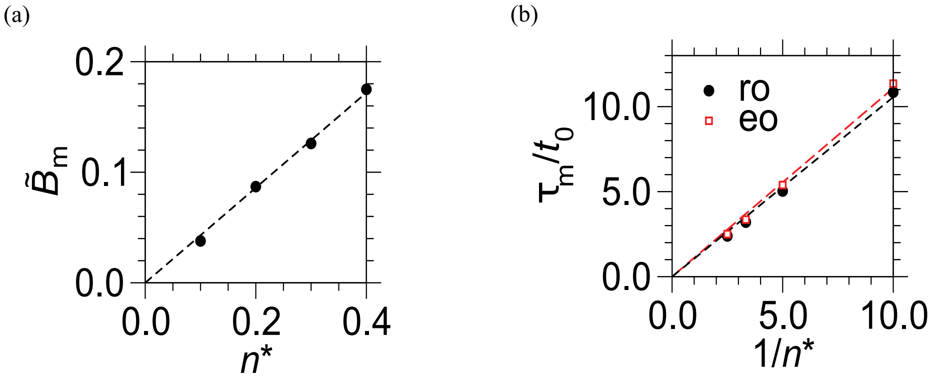

Figure 4.12: (a) $\tilde{B}_m$, which is the magnetic field at which $\sigma_{xx} \propto \tilde{B}^{\delta}$ loses its validity vs. n^* for the equally oriented RCs. (b) τ_m/t_0, which is the time at which the derivative of the MSD is maximal vs. $1/n^*$ for both orientations. Figure from [25].

4.3 Comparison between MD simulations and experiments

Two systems were realized, namely the experimental implementation of a 2DLG with RCs and the implementation in the simulation. The results of both are compared in this section.

Between the two systems exist systematic differences: in experiments there are always scattering channels caused by intrinsic impurities or phonons, and moreover, the system has boundaries. The main condition for the anomalous transport observed in the simulation at $\tilde{B} = 0$ is that the tracer particle is able to move for long time intervals without being scattered from its straight trajectory. Its direction is only changed by colliding with an obstacle. Slight deviations prevent the occurrence of anomalous transport. This is why the conductivity is measurable and a finite value at $\tilde{B} = 0$ in the experiment.

Fig. 4.13 compares the experimental and simulation results for the different n^* for equally oriented RCs. The experimental data are measured at a temperature of $T = 0.1\,\mathrm{K}$. The amplitudes in σ_{xx} of both implementations become more similar with increasing n^*. Part (a) of Fig. 4.13 compares the magnetoconductivities of $n^* = 0.1$ and $n^* = 0.2$ between the simulation and experiment. Part (c) provides the same comparison but for two higher densities of $n^* = 0.3$ and $n^* = 0.4$. For $n^* = 0.4$, the discrepancy between the experiment and simulation is smaller than 14 % in the interval $0.1 < \tilde{B} < 2.4$. The better agreement between simulation and experiment is based on the influence of background impurities in the host crystal decreasing as the obstacle density increases, and furthermore, the magnetotransport is more dominated by the 2DLG than by other scattering channels.

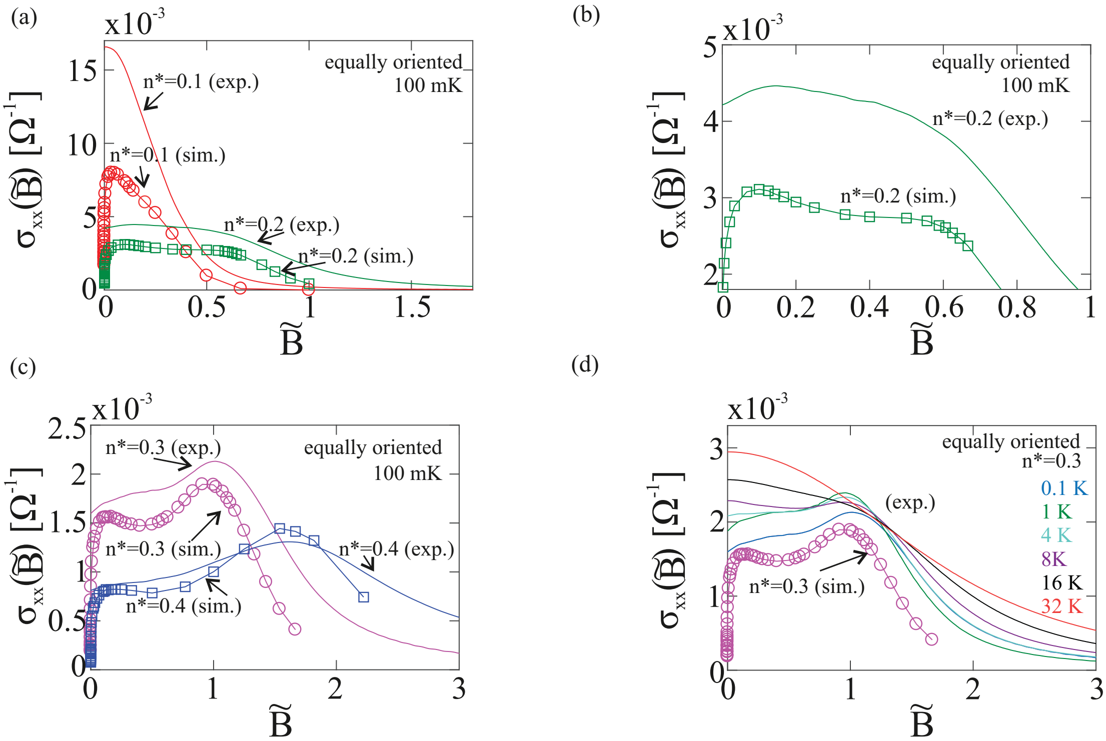

Figure 4.13: Comparison between the experiment and simulation for equally oriented RCs. (a) σ_{xx} vs. $\tilde{B}$ for the equally oriented RCs for $n^* = 0.1$ and $n^* = 0.2$. (b) Zoom-in of the trace for $n^* = 0.2$, which clearly shows the agreement of the experimental and simulation local maximum at $\tilde{B} \approx 0.1$. (c) The same representation as in (a) for the densities $n^* = 0.3$ and $n^* = 0.4$. Comparing the absolute values of σ_{xx} in (a) and (c) it can be inferred that with increasing obstacle density the agreement between the simulation and experiment intensifies. (d) Temperature dependence of the 2DLG with $n^* = 0.3$ and the results from the simulation. The local maximum at approx. $\tilde{B} = 0.1$ vanishes at 4 K, whereas the maximum at $\tilde{B} = 1$ is temperature stable up to 16 K, indicating different length scales of the two mechanisms involved.

At very low magnetic fields, the experiment and simulation deviate strongly from each other. In the simulation, σ_{xx} exhibits a power law, as detailed in Subsection 4.2.3. The experimental trace saturates to a finite value as $\tilde{B}$ approaches zero. In the simulation, no scattering of tracer particles occurs other than at the RCs. At zero magnetic field, the trajectories do not deviate from straight lines. This leads to the nonexistence of $\sigma_{xx}(0)$ in the simulation.

On the other hand, in the regime of magnetic fields below the conductivity maximum caused by the directed motion along the obstacle edges, the experimental traces show clear signatures of anomalous transport. For example the trace of $n^* = 0.3$ shows a clear local maximum around $\tilde{B} = 0.1$, which can be attributed to the same effect underlying the local maximum in that regime of the simulation trace. All four dimensionless densities n^* under study show this behavior, and the lowest density $n^* = 0.1$, where the conductivity maximum caused by the guided tracer particle motion is not evolved. In Fig. 4.13 (b), a pronounced maximum in σ_{xx} is visible in agreement with the simulation.

Part (d) of Fig. 4.13 shows the results of the equally oriented RCs from the simulation and all measured temperatures. As the sample temperature is increased, scattering contributions from phonons increase and superimpose 2DLG characteristics. The conductivity maximum caused by the guided transport along the obstacle edges remains temperature stable up to 16 K. The local maximum caused by the anomalous transport at lower magnetic fields loses its characteristic shape at approximately 4 K, a temperature at which quantum effects can be excluded. Because of this large difference in temperature dependence, it can be stated that the effect behind the local maximum at low magnetic fields demands longer length scales at which the electron is not scattered off its trajectory, compared with the maximum at higher magnetic fields.

Moreover, the conductivity at $\tilde{B} = 0$ increases with increasing temperatures, indicating that retroreflective trajectories are reduced by increasing temperature, which is consistent with the other obtained results.

In sum, at low temperatures and high obstacle densities, the highest contributions of the anomalous transport caused by retroreflectivity are observed. For all configurations, the anomalous transport caused by RCs can be seen in the simulation. For finite values of$\tilde{B}$, the experiment and simulation deliver consistent results.

CHAPTER 5

EXPERIMENTS ON BIMODAL CIRCULAR LORENTZ GASES

In the GaAs/AlGaAs host structure, inevitable background scattering exists. This causes deviations between theoretical predictions, MD simulations, and experimental results. Scattering can be caused by impurities, phonons, and the potential of the delta-doping layer. Deviations attributed to background scattering occur between the experimental and simulation results of magneto- conductivity. Deviating results are especially observed at elevated magnetic fields (see Section 3.3 and Chapter 4). Moreover, theoretical considerations predicted a decreasing conductance for dilute 2DLGs at small magnetic fields and an increasing conductance at larger magnetic fields. This is caused by the depinning of electrons from encircling a single or a cluster of LG obstacles. [23, 35] The classical simulations presented in [15], which reproduce the measured magnetoconductance maximum with high accuracy, show significant deviations for large magnetic fields. Therefore, another mechanism besides the initiation of Landau-quantization influences the magnetoconductivity in this interval.

This motivates an experimental investigation into the influence of background scattering on the magnetoconductance and magnetoresistivity of 2DLGs. Of course, the background scattering from the GaAs/AlGaAs host structure itself cannot be reduced or modified, but it is possible to add additional scattering channels in a controlled way. Therefore, two types of additional scattering are systematically varied and superimposed on the reference 2DLG matrix.

One additional dynamic scattering channel is provided by temperature. By increasing the population of the phonon branch, statistically independent scattering reduces the mean free path of the electrons. Because the scattering events caused by temperature are uncorrelated to each other, this type of scattering is hereinafter termed “dynamic scattering.”

The second scattering channel is provided by the static potential of a secondary 2DLG comprising small obstacles at low densities. This is superimposed on the primary 2DLG, as both are introduced in one measurement field. Because of this static background potential, memory effects are expected

to be amplified. This type of controlled addition of scattering is hereinafter referred to as “static” scattering.
The results from the present chapter were published in [29].

5.1 Sample design and experimental details

The GaAs/$Al_{0.3}Ga_{0.7}As$ heterostructure with a 2DEG situated 150 nm below its surface is used as the host material (for a detailed description see Subsection 2.3.1). At 4.2 K, all samples had an electron density of $n_e = 2.5 \cdot 10^{15}\,\mathrm{m}^{-2}$ and an electron mobility of $734\,\mathrm{m}^2/\mathrm{Vs}$, which corresponds to an intrinsic mean free path of $l_{\mathrm{mfp}} = 60.5\,\mu\mathrm{m}$. The quantum scattering time τ_q, determined from the envelope of the SdHo along the lines of Ando [139], is determined to be $\tau_q = 2.4\,\mathrm{ps}$. This corresponds to a quantum scattering length of $l_q = v_F \cdot \tau_q = 530\,\mathrm{nm}$. From the ratio $l_{\mathrm{mfp}}/l_q \approx 114$ it can be expected that the intrinsic disorder from the host crystal is relatively weak and most scattering contributions originate from remote donor ions in the delta-doping layer.
Through optical lithography and wet chemical etching, a Hall bar is defined (detailed in Section 2.1). The Hall bar has a width of $w = 100\,\mu\mathrm{m}$ and contains five measurement fields, each with four voltage probes of 10 µm in width. Two adjacent voltage probes of a measurement field are separated by 100 µm. The measurements were conducted in an ^{4}He-gas flow cryostat allowing for temperatures between 1.4 K and room temperature. Furthermore, the resistance in the direction of the Hall bar R_{xx} and perpendicular to it R_{xy} was recorded as detailed in Section 2.2.
To investigate the influence of static background scattering on the magnetoconductivity of 2DLGs the following sample layout was designed:
The 2DLGs were defined by a random number generator, generating values for the obstacle’s center coordinate (x,y). In the electron beam lithography at each center coordinate, a circle with a lithographic radius r_{litho} was defined. A numerical Voronoi tessellation followed by a fit to the cell area distribution proved the LG-obstacles to be Poisson distributed with mutual overlap allowed. [93]
2DLGs arrays, which are composed only of circular obstacles with a lithographic radius $r_{\mathrm{p,litho}} = 925\,\mathrm{nm}$, are called “primary 2DLGs” hereinafter. Additionally, “secondary Lorentz gases,” which are composed of obstacles with a lithographic radius of $r_{\mathrm{s,litho}} = 75\,\mathrm{nm}$ and exhibit a lower dimensionless obstacle density n^*, were patterned on a separated measurement field.
Four primary and seven secondary 2DLGs are experimentally implemented. Mixtures of one primary and one secondary 2DLGs are patterned as well and are called “bimodal” hereinafter. Bimodal arrays are prepared by subsequently illuminating one primary and one secondary array.
Each 2DLGs is characterized by the conventional dimensionless number density:

$$n_j{}^* = n_j r_j{}^2 \tag{5.1.0.1}$$

Here, j denotes either $j = p$ for the primary 2DLG or $j = s$ for secondary 2DLG; $n = N/A$is the number of obstacles N per area A; and $n_j{}^*$ corresponds to the area of the obstacles, divided by π, that would

be covered if no overlap is allowed.
From the geometric specifications, the mean free path induced by the 2DLG array is as follows [17]:

$$l_j = \frac{1}{2n_j r_j} \tag{5.1.0.2}$$

All densities are chosen such that $l_p < l_s < l_{\text{mfp}}$ holds for all combinations.
Fig. 5.1 (a) depicts the schematic sample setup. The left measurement field contains a primary 2DLG. The measurement field in the middle is filled with a secondary 2DLG with obstacles of smaller size and lower n_s^*. The right measurement field is the superposition of the left and middle measurement fields. For the real sample, two more measurement fields follow: one plain secondary 2DLG of larger n_s^* and finally the mixture of this with the first primary 2DLG. Parts (b) and (c) of Fig. 5.1 are scanning electron microscopy images of sample sections; (b) shows a unimodal secondary array and (c) is an image of a bimodal 2DLG.
The respective geometries are transferred to the sample by electron beam lithography and reactive ion etching. The etch depth is chosen as 150 nm, which guarantees the depletion of the 2DEG at the respective positions. Each etching process leads to a lateral depletion of approximately 20 nm, which is detailed in the discussion of the measurement results.
Considering the lateral depletion, the effective radius for the primary obstacles is $r_p = 945\,\text{nm}$ and for the secondary obstacles it is $r_s = 95\,\text{nm}$.

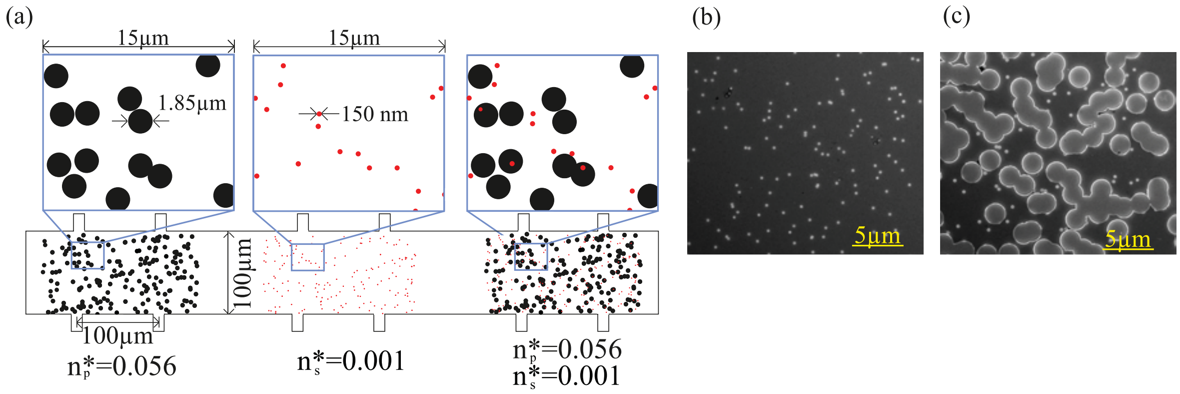

Figure 5.1: (a) Schematic representation of the sample design. The first measurement field, which consists of a primary 2DLG with $n_p{}^* = 0.056$, is followed by the middle measurement field, which contains a secondary 2DLG with $n_s{}^* = 0.001$. The right measurement field is the superposition of the primary and secondary 2DLGs. The dimensions given in the figure are the lithographic specifications. (b) Scanning electron microscopy (SEM) image of a section of a secondary 2DLG. (c) SEM image of a bimodal section of a 2DLG. Figure from [29].

The sample parameters are summarized in table 5.1:

primary LG	$r_p = 945\,\mathrm{nm}$		secondary LG	$r_s = 95\,\mathrm{nm}$	
n_p/m^{-2}	$n_p^* = n_p r_p^2$	$l_p/\mu\mathrm{m}$	n_s/m^{-2}	$n_s^* = n_s r_s^2$	$l_s/\mu\mathrm{m}$
$6.26 \cdot 10^{10}$	0.056	8.5	$1.11 \cdot 10^{11}$	$1.0 \cdot 10^{-3}$	47.4
$1.25 \cdot 10^{11}$	0.112	4.23	$1.75 \cdot 10^{11}$	$1.6 \cdot 10^{-3}$	30
$1.875 \cdot 10^{11}$	0.167	2.82	$2.57 \cdot 10^{11}$	$2.3 \cdot 10^{-3}$	20.5
$2.5 \cdot 10^{11}$	0.223	2.12	$2.66 \cdot 10^{11}$	$2.4 \cdot 10^{-3}$	19.7
			$4.17 \cdot 10^{11}$	$3.76 \cdot 10^{-3}$	12.6
			$5.56 \cdot 10^{11}$	$5.02 \cdot 10^{-3}$	9.5
			$12.5 \cdot 10^{11}$	$11.3 \cdot 10^{-3}$	4.2

Table 5.1: Sample parameters of the primary and secondary 2DLGs.

5.2 Effect of dynamic and static background scattering

Figure 5.2 depicts the magnetoresistivities $\rho_{xx}(B)$ for the unimodal secondary (part (a)) and unimodal primary (part (b)) of all seven secondary and four primary 2DLGs.

As ${n_s}^*$ increases, a characteristic smooth peak evolves, which systematically broadens and becomes larger in amplitude. In accordance with the model presented by Bobylev et al. [19], this negative magnetoresistivity is caused by the localization of electrons in undisturbed cyclotron orbits around LG obstacles or voids (further detailed in Section 3.3). These electrons do not contribute to the conductivity.

The traces with higher n_s^* show that SdHo set in at higher magnetic fields. The inset in the upper-right side of Fig. 5.2 (part (a)) depicts the zero-field resistivity $\rho_{xx}(B=0)$ against the obstacle density n_s. As the figure shows, it is possible to fit the data linearly. From the slope of this linear fit, it is possible to determine the effective obstacle radius r_s because the resistivity values are expected to be as follows [35]:

$$\rho^s_{xx}(0) = \frac{m^*}{n_e e \tau_s} \tag{5.2.0.1}$$

where $m^* = 0.067 m_e$ denotes the effective mass in GaAs and τ_s the momentum relaxation time of the 2DLG, which is defined as:

$$\tau_s = \frac{1}{2 n_s r_s v_F} \tag{5.2.0.2}$$

The electronic radius of the secondary obstacles was determined from $\mathrm{d}\rho^s_{xx}(0)/\mathrm{d}n_s = 3.85 \cdot 10^{-11}\,\Omega\mathrm{m}^2$ to be $r_s \approx 95\,\mathrm{nm}$. Since the lithographic radius of the secondary obstacles was set as $r_{\mathrm{g,litho}} = 75\,\mathrm{nm}$, the lateral depletion length can be assumed to be 20 nm. This value is also assumed for larger obstacles of the primary 2DLGs. The intersection of the linear fit for $n_s = 0$ gives a value of $\rho_{xx}(B = 0, n_s = 0) = 3.3\,\Omega$. This agrees well with the zero-field resistivity measured for the pristine 2DEG of

$\rho_{xx}(0) = 3.4\,\Omega$.
For the primary 2DLGs, as shown in the inset of Fig. 5.2 (b), the relationship between n_p^* and $\rho_{xx}^p(0)$ is superlinear. Here, n_p^* is far away from the dilute limit where equation 5.2.0.1 does not hold because memory contributions other than the localization of electrons in cyclotron orbits contribute to the magnetoresistivity.

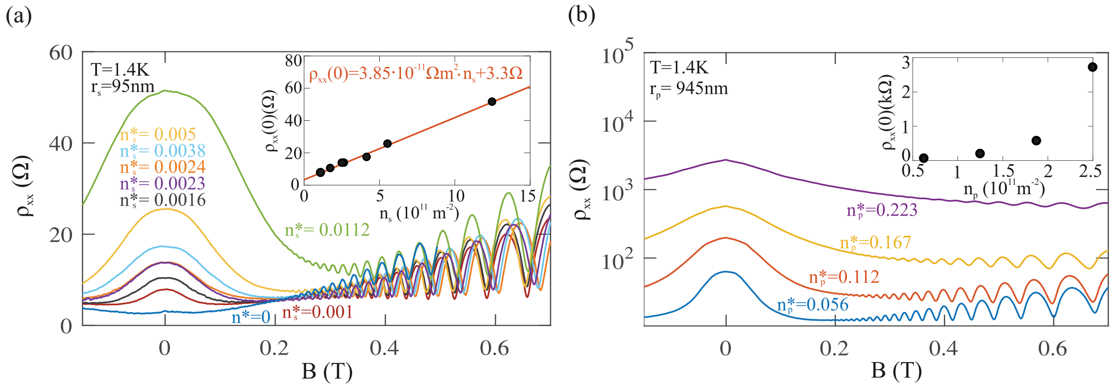

Figure 5.2: (a) Longitudinal magnetoresistivities of the secondary 2DLGs. The width and height of the bell shaped trace increase with n_s^*. The inset proves a linear relationship between the zero-field resistivity $\rho_{xx}^s(0)$ and obstacle density n_s. (b) The same representation as for (a) but for primary 2DLGs. The magnetoresistivity exhibits a broader bell shape, with the same characteristic of increasing width and amplitude as n_p^* increases. From the inset, a superlinear relationship between n_p and $\rho_{xx}^s(0)$ can be inferred. Figure from [29].

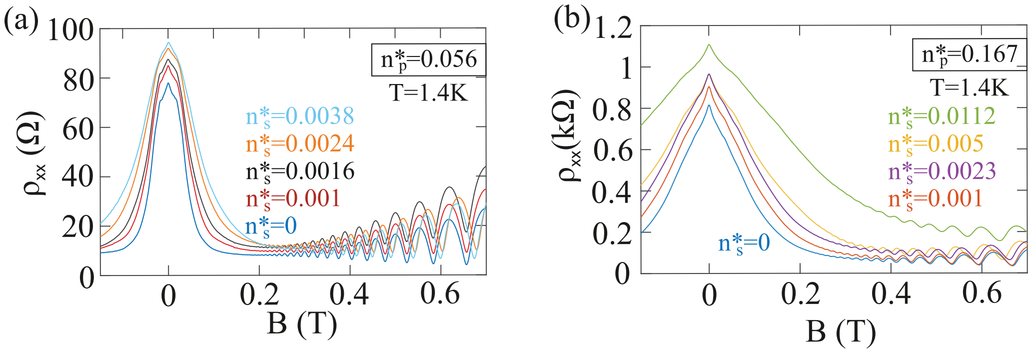

Figure 5.3: Magnetoresistivities of (a) $n_p^* = 0.056$ and (b) $n_p^* = 0.167$ with additional superposition of secondary 2DLGs, with the corresponding values of n_s^* being denoted in the figure. All traces were measured at 1.4 K. Figure from [29].

The effect of the secondary arrays on magnetotransport is detailed as follows starting with the magnetoresistivity, which is presented in Fig. 5.3. Bimodal arrays of $n_p^* = 0.056$ and $n_p^* = 0.167$ are combined with seven values of n_s^* ranging from 10^{-3} to $1.1 \cdot 10^{-2}$. The addition of the secondary 2DLGs leads to a broadening of the magnetoresistivity trace for both values of n_p^*. The amplitude of the zero-field resistivity increases, and SdHo set in at higher magnetic fields. This is a monotonic evolution with respect to n_s^*.

These data can be transferred to the longitudinal conductivity with: $\sigma_{xx}(B) = \rho_{xx}(B)/(\rho_{xx}^2(B) + \rho_{xy}^2(B))$. The data of Hall resistivity $\rho_{xy}(B)$ are presented in the Appendix (Chapter 8). In the following subsection the data in $\sigma_{xx}(B)$ are presented, which allows for a comparison with earlier experimental and theoretical work (detailed in Section 3.3). [15, 19, 30]

5.2.1 Influence of additional static scattering centers

The conductivity $\sigma_{xx}(B)$ of the $n_p^* = 0.056$ primary 2DLG is presented in Fig. 5.4 by the dark blue trace. The other colors distinguish the $\sigma_{xx}(B)$ traces of the bimodal arrays. Part (b) of Fig. 5.4 is the same representation but for $n_p^* = 0.167$. For all traces, a conductivity maximum can be observed. Comparing the cases of the unimodal $n_p^* = 0.056$ and $n_p^* = 0.167$, one finds the maximum to be broader and at a larger magnetic field for the denser 2DLG. This is in agreement with the findings of [15].

The addition of secondary 2DLG fields changes the magnetoconductivity in a qualitative way. Three regimes can be distinguished: regime A at low magnetic fields, which means below the magnetic field where the conductivity maximum occurs $B < B_{\max}$; regime B, which is localized around the position of maximal conductivity $B_{\max}$; and regime C, which is at magnetic fields larger than $B_{\max}$. Here the transport transits to localization. Following the model system of magnetotransport of a unimodal 2DLG, the influence of the secondary 2DLG on it (comparable to a static impurity landscape such as the inevitable impurity background) is discussed with the measurements in Fig. 5.4.

Considering regime B (i.e., the evolution of the conductivity maximum), it is found that increasing the addition of n_s^* at a constant n_p^* shifts the position of the maximum to larger B-field values and the magnetoconductivity trace broadens. Additionally, the amplitude of the maximum decreases as n_s^* increases. These observations qualitatively agree for both n_p^*. The shift of the position of maximal conductivity is caused by the effectively higher number of obstacles. The electrons are in a superdiffusive regime of $\vec{E} \times \vec{B}$-drift along the cluster edges, combined with jumps from one cluster to an adjacent one. The admixture of smaller-sized obstacles in the 2DLG landscape of the primary array does not change this phenomenology. If an electron hits a smaller LG obstacle, its direction is microscopically changed but the increased diffusion remains.

In regime A of small magnetic fields, the magnetoconductivity $\sigma_{xx}(B)$ is reduced as n_s^* increases. For the primary 2DLG with $n_p^* = 0.056$, this regime can be distinguished to be lower than $B_c = 29\,\mathrm{mT}$. At B_c, the conductivity σ_{xx} is independent of n_s^*. Such a fixed point does not exist for $n_p^* = 0.167$ (see part (b) of Fig. 5.4), but the general phenomenology is the same as that for the primary 2DLG with lower density.

The phenomenology of regime A can be explained in terms of a memory-effect dominated conductance. The additional secondary 2DLG opens more retroreflecting corridors. Thus, electrons probe the same area several times leading to a reduction of σ_{xx}. As the magnetic field is increased, the ballistic area in which the electron is known not to be scattered on its way to an obstacle reduces due to the bending of its trajectory. On its way back, the bending is in the opposite direction. This is illustrated in Fig. 5.6 (b): the darker gray shaded area corresponds to the ballistic corridor, in which the electron will not be scattered the second time it passes because it was not scattered before and the obstacle position is static. The right-hand side of Fig. 5.6 (b) depicts the reduction of this area by an introduced magnetic field with $B > 0$. The middle part of the figure shows an additional corridor, which opens due to an LG obstacle of the secondary 2DLGs. Therefore, it can be stated that for low magnetic fields, the corridor effect increases with additional smaller obstacles, reducing the longitudinal conductivity σ_{xx}.

Regime C, starting above the position of maximal conductivity, is caused by an elevated magnetic field. The cyclotron diameter decreases with increasing B. Once it is smaller than the distance of the gap width between adjacent clusters, the localization caused by $\vec{E} \times \vec{B}$-drift along the contour of an LG assembly increases. From the measurements it is visible that the conductivity increases as the density of secondary scattering centers increases (see Fig. 5.4). This is valid for both values of n_p^* and fits excellently with the image of localization at high magnetic fields: the secondary LG obstacles will also be positioned along the trajectory of localization. This causes a detachment of the electron from the cluster edges and the obstacle of the secondary 2DLG thus offers a connecting path between the edge channels of adjacent primary clusters. This behavior was explained along the lines by Mirlin et al. [35]. The secondary array also provides further $\vec{E} \times \vec{B}$ drift along the cluster edges at larger magnetic fields. Fig. 5.6 (a) illustrates this behavior using two trajectories in a unimodal 2DLG (left) and a bimodal 2DLG (right) for $B > 0$.

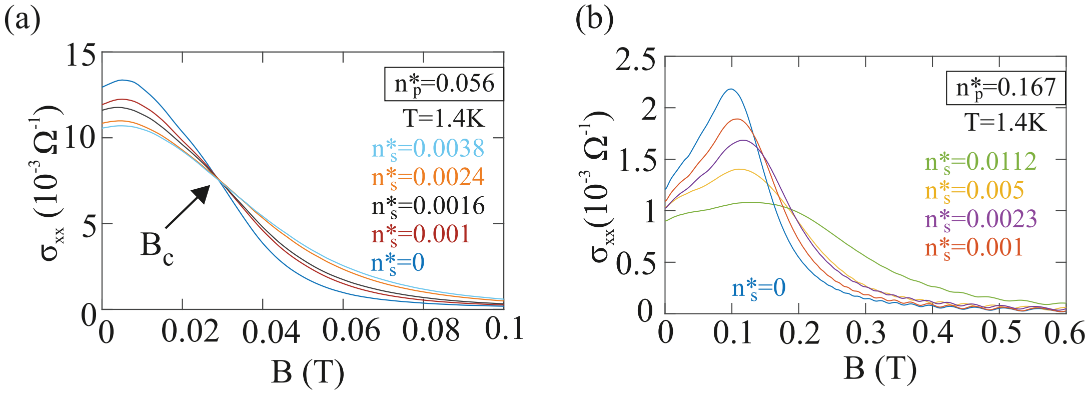

Figure 5.4: Magnetoconductivity $\sigma_{xx}(B)$ for the unimodal and bimodal 2DLGs for $n_p^* = 0.056$ shown in part (a) and $n_p^* = 0.167$ shown in part (b). The qualitative behavior in (a) and (b) is the same and can be distinguished in three regimes, as detailed in the main text. Figure from [29].

5.2.2 Influence of additional dynamic scattering centers

After the influence of a static additional scattering potential on the magnetoconductivity of the primary 2DLG was discussed, it is interesting to compare this behavior with the influence of elevated temperatures on the magnetoconductivity of the primary 2DLGs. An increase in temperature causes dynamic background scattering; that is, the scattering processes are independent of each other as demanded by the Drude-Boltzmann model. Measurement results are presented in Fig. 5.5 for the $n_p^* = 0.056$ (part (a)) and $n_p^* = 0.167$ (part (b)) primary 2DLGs at temperatures between 1.4 K and 32 K. The blue traces are measured at the lowest temperature of 1.4 K and are the same as the data presented in blue in Fig. 5.4, which aims for the investigation of additional static background scattering. Therefore, it is possible to analyze the differences caused by either dynamic or static additional scattering on the magnetotransport of the primary 2DLG.

Within the temperature evolution of the magnetoconductivity depicted in Fig. 5.5, one finds for regime C (i.e., at magnetic fields above the position of the conductivity maximum) that $\sigma_{xx}(B)$ increases as the temperature increases. The elevated temperatures cause the same behavior as would increasing the static background by a secondary 2DLG. This can be explained as follows [35]: the electron is prevented from localizing along the cluster contour because a dynamic scattering event caused by a phonon detaches the electron from the undisturbed trajectory, which increases the conductivity. Therefore, it can be stated that for regime C it does not matter whether the detaching scattering event is of a static or dynamic origin. By contrast, for regime A, at low magnetic fields, the additional dynamic scattering increases σ_{xx} as the temperature increases. This is the opposite behavior to static background scattering. σ_{xx} increases monotonously for the array with $n_p^* = 0.167$ up to the highest temperature of 32 K. The primary array with $n_p^* = 0.056$ shows the same behavior but stops and reverses at 16 K. For this array and under these conditions, there exists a fixed point at a lower magnetic field of $B_c \approx 26\,\mathrm{mT}$ as also exists for the static scattering background.

It can be stated that within magnetic fields of regime A, the character of the background scattering (dynamic or static) influences the conductivity with either a positive or negative contribution. The static secondary 2DLGs increase the memory effects while dynamic scattering decreases them. Dynamic scattering delocalizes an electron by detaching it from a ballistic corridor. The static scattering centers, on the other hand, open up additional retroreflective paths. Here additional results from MD simulations, such as those performed in [15, 18], would help to manifest this image.

Moreover, the cyclotron motion and the rosette-type orbits, which increase with magnetic field (detailed in [19, 21]) and reduce the conductivity, are disturbed by dynamic scattering.

Regime B is highly pronounced for the primary 2DLG with $n^* = 0.167$. Here, two fixed points at $B_c \approx 45\,\mathrm{mT}$ and $\approx 128\,\mathrm{mT}$ exist. In the interval between them the conductivity decreases as the temperature increases. The dynamic scattering disturbs the guided motion of the electrons along the 2DLG cluster edges and increases the diffusive scattering part such that the σ_{xx} reduces. The elevated temperatures do not change the position in B at which the conductivity maximum occurs. The same phenomenology can be found for the primary 2DLG with $n_p^* = 0.056$, although no second fixed point at low magnetic fields exists.

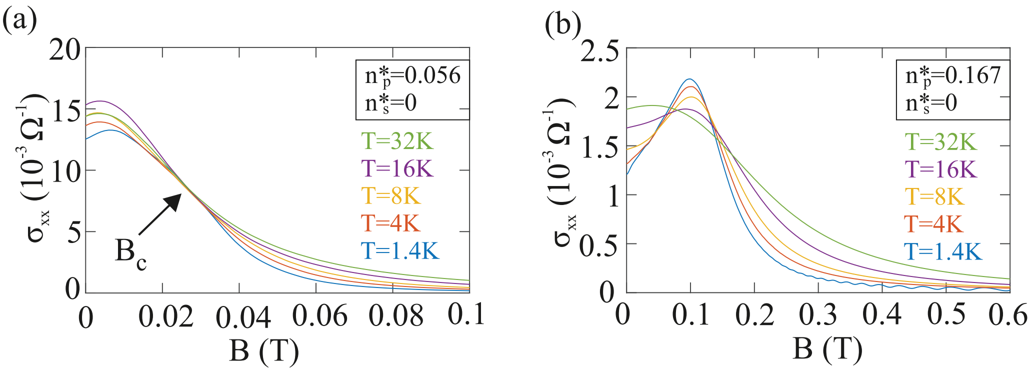

Figure 5.5: Temperature dependency of the unimodal primary 2DLG with $n_p^* = 0.056$ (a) and $n_p^* = 0.167$ (b). Temperature elevation adds dynamic scattering to the system. Regimes A, B, and C are also distinguishable under these experimental conditions. In strong contrast to static scattering is that at low magnetic fields $\sigma_{xx}(B)$ increases as the temperature increases (regime A). This indicates that dynamic scattering causes depinning of electrons from retroreflective corridors, while static scatterers open up additional corridors of retroreflection. Figure from [29].

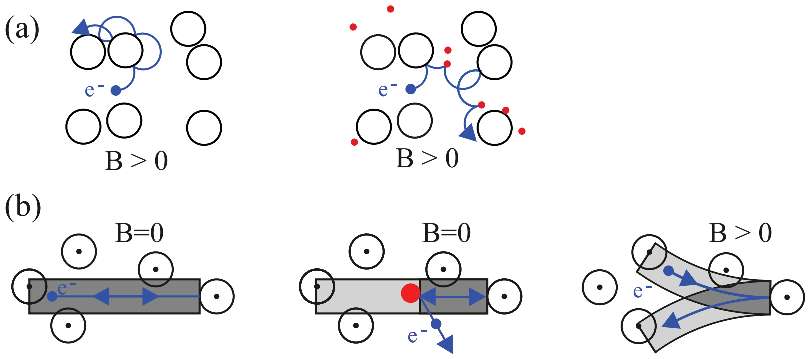

Figure 5.6: (a) For a finite magnetic field in regime C, $\sigma_{xx}(B)$ was found to be reduced in the unimodal 2DLGs compared with the value $\sigma_{xx}(B)$ at the same B, but for the bimodal 2DLG with the same n_p^*. By scattering an electron at additional LG obstacles, the localization transition is less probable, which causes increased $\sigma_{xx}(B)$ compared with the unimodal array. (b) Left: The electron is reflected back and forth in a retroreflective corridor at $B = 0$. Middle: The addition of a secondary 2DLG leads to further corridors, which decreases $\sigma_{xx}(0)$. Right: A perpendicular magnetic field reduces the retroreflective area, which is depicted here in darker gray. Figure from [29].

5.2.3 Comparison with existing models of background scattering in 2DLGs

For a clean and dilute 2DLG, Bobylev et al. [19, 22] predicted an exponential decay of ρ_{xx}, follow

$$\rho_{xx}(B) = \rho_0 \left(1 - \exp\left(-\frac{2\pi}{\omega_c \tau}\right)\right) \tag{5.2.3.1}$$

where τ denotes the momentum relaxation time of the 2DLG. Fig. 5.7 shows the data of the unimodal secondary 2DLG with $n_s^* = 0.0038$ and $n_s^* = 0.001$, with the traces predicted by the model of Bobylev. The background resistivity of 3.4 Ω was taken into account. The amplitudes of the resistivity peaks do fit well, but the measured traces are broader and more parabolic. As this was found for all unimodal secondary arrays, a significant influence of the intrinsic disorder of the host material on the peak shape can be deduced.

Figure 5.7: Magnetoresistivity of the unimodal secondary 2DLGs with $n_s^* = 0.001$ and $n_s^* = 0.0038$ (full lines) compared with the predictions of the Bobylev model (broken lines). The high discrepancy of the peak shapes infers influences of intrinsic background scattering. Figure from [29].

Earlier work on the dilute 2DLG under the influence of random and weak background scattering was performed by means of analytical and numerical methods [23, 71]. Within these works from Mirlin et al., an unconventional interplay between the scattering mechanisms at different length scales was found.

The magnetoresistivity was predicted to reduce close to $B = 0$ following a parabola, while at higher B a characteristic B^-4 decrease of ρ_{xx} was found. This model was applied in the work of [65] and [66] to analyze the parabolic part of GNMR (see Subsection 3.2.6). Those results lead to the interpretation of the background scattering occurring from sparse oval defects forming a dilute 2DLG.

Therefore, the presented magnetoresistivity is analyzed along the lines of the Mirlin model [71] (see a detailed presentation in Subsection 3.3.1). The analysis begins with the unimodal secondary 2DLG, which should fulfil the required conditions most suitably of all samples. As stated, a parabolic magnetoresistivity is expected for small magnetic fields, following

$$\frac{\Delta\rho_{xx}}{\rho_0}(B) = -\left(\frac{\omega_c}{\omega_0}\right)^2 \tag{5.2.3.2}$$

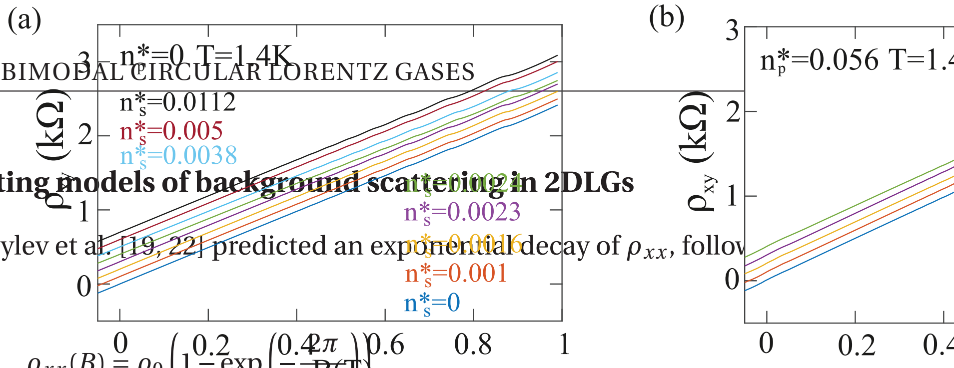

Fig. 1: (Colour on-line) Hall resistivities of (a) the secondary
the bimodal 2DLGs with $n_p^* = 0.167$. In (b) and (c), the corre
figures, subsequent traces are offset for clarity by 100 Ω.

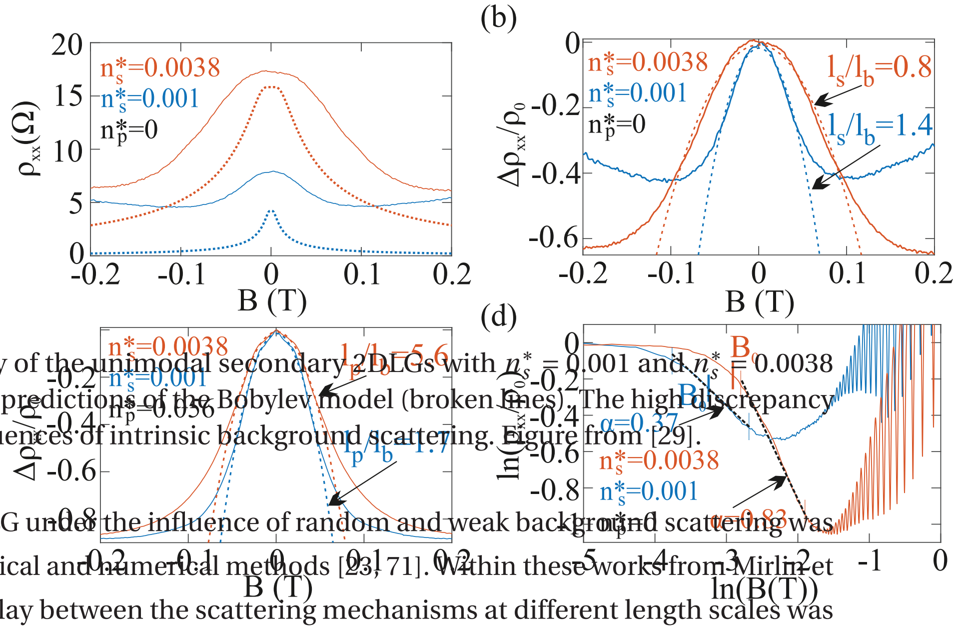

Fig. 2: (Colour on-line) (a) Comparison of $\rho_{xx}(B)$ (full lines) for two of the unimodal secondary arrays to the Bobylev expression (dashed lines, following eq. 1) in the absence of background disorder. (b) Parabolic fits of the normalized magnetoresistivity of these arrays, using ℓ_s/ℓ_b as the fit parameter. (c) Parabolic fits to two the magnetoresistivity of two bimodal arrays. Here, the fit parameter is ℓ_p/ℓ_b, where ℓ_b combines the scattering at the secondary array and at the intrinsic disorder. (d) Double logarithmic plot of $\rho_{xx}(B)$ for the two arrays shown in (a) and (b), and the corresponding fit values for the exponent α in the tails. The fit window is indicated by the dashed vertical lines, and B_0, marked by the bold vertical lines, denotes the magnetic field where $\omega_0 = \omega_c$ (eqns. 2, 3). In all measurements, the temperature was 1.4 K.

This analytic expression is predicted to be valid in the interval $\omega_c < \omega_0$, with $\omega_0 = \sqrt{2\pi n_j} \times v_F \times (2l_j/l_b)^{0.25}$. The integer j distinguishes the 2DLG to be $j = p$ from a primary 2DLG or to be $j = s$ from a secondary 2DLG. The length l_b is the average length an electron moves freely in the sample until it experiences a displacement of its guiding center, which is $\delta = \sqrt{4\pi v_F^3/(\omega_c^3 l_b)}$. Fig. 5.8 (a) shows (in dotted lines) fits to the magnetoresistivities of the secondary 2DLG with $n_s^* = 0.0038$ and $n_s^* = 0.001$ (full lines correspond to the measurement). The ratio l_s/l_b, (i.e., the ratio of the mean free paths of the dominant source of scattering to the host crystal's background scattering) is used as the fit parameter. For the array with $n_s^* = 0.001$, a value of $l_s/l_b = 1.42$ is determined. For $n_s^* = 0.0038$ a value of $l_s/l_b = 0.80$ is found. From the geometric specifications, one might expect a mean free path of the 2DLG of $l_s = (2n_s r_s)^{-1} = 47.5\,\mu\text{m}$ for $n_s^* = 0.001$ and $l_s = 12.6\,\mu\text{m}$ for $n_s^* = 0.0038$. From the background resistivity of $3.4\,\Omega$, the mean free path is expected to be $l_b = 60.5\,\mu\text{m}$. Thus, the corresponding values of l_s/l_b are expected to be 0.79 and 0.21. Therefore, it can be said that the fit results have the correct order of magnitude but deviate significantly from the expected value.

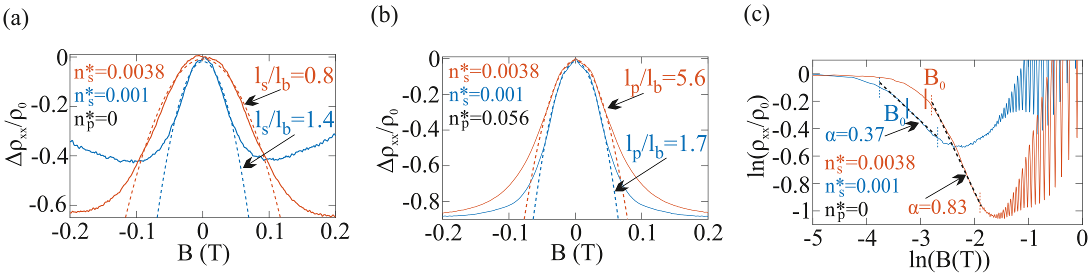

Figure 5.8: (a) Normalized magnetoresistivities of the unimodal secondary 2DLG (full lines) and parabolic fits to them (broken lines) with l_s/l_b as the fit parameter. (b) The same representation as in (a) but for two bimodal primary 2DLGs ($n_p^* = 0.056$), showing that l_p/l_b deviates significantly from the Mirlin model. l_b is determined by the intrinsic background and the secondary 2DLG. (c) Double logarithmic representation of the normalized magnetoresistivity for the two arrays shown in (a). The fit values for α show that $\rho_{xx}(B)$ does not decay with $\alpha = 4$ as predicted by the Mirlin model. The fit window is indicated by the vertical lines, where B_0 denotes the magnetic field for which $\omega_0 = \omega_c$ is valid. Figure from [29].

Reasons for these deviations could be that the pattern transfer of the 2DLGs to the host crystal might have generated additional disorder. Therefore, l_b was estimated to be too long. Another possibility is that the true background potential contains components originating from sparse but strong scatterers such as impurities or oval defects. This is disagrees with the background potential in the Mirlin model, where it is expected to be weak.

The bimodal 2DLG allows for another interpretation of the data along the lines of Mirlin: the primary array determines the main scattering (i.e., $j = p$; in equation 3.3.1.4), whereas the secondary array forms the background potential together with the intrinsic disorder. Part (b) of Fig. 5.8 presents parabolic fits for the bimodal 2DLGs with $n_p^* = 0.056$, $n_s^* = 0.001$, $n_p^* = 0.056$, and $n^* = 0.0038$. The

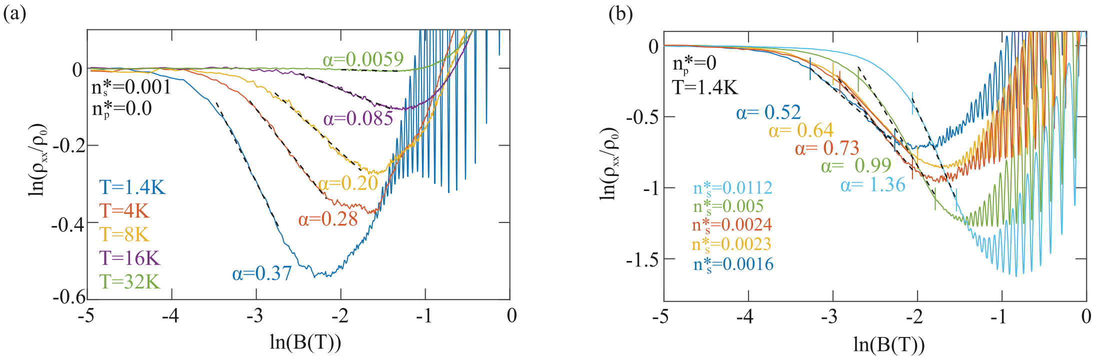

Figure 5.9: (a) Double logarithmic representation of the normalized resistivities presented against the magnetic field for the unimodal secondary 2DLG with $n_s^* = 0.001$ at different temperatures. (b) The same representation as in part (a) but for five different unimodal secondary 2DLGs at a constant temperature of 1.4 K. Figure from [29].

corresponding fit values are $l_p/l_b = 1.7$ and 5.6, respectively. Expected from the geometries are ratios of 0.18 and 0.67. This supports the hypothesis that the background scattering was assumed to be smaller than it is in reality for the unimodal secondary 2DLGs.

For magnetic field values corresponding to $\omega_c > \omega_0$, the Mirlin model predicts a $\rho_{xx} \propto B^{-\alpha}$ dependency with $\alpha = 4$. Therefore the exponent α was determined from the double-logarithmic plot (see part (c) of Fig. 5.8). This analysis is presented for the unimodal secondary 2DLGs with $n_s^* = 0.001$ and $n_s^* = 0.0038$. The fit interval was chosen in between B_0 (corresponding to ω_0) and the set-in of the SdHo. The experimental value for α was found to be a factor of 5 to 20 smaller with $\alpha = 0.37$ (for $n_s^* = 0.001$) and $\alpha = 0.83$ (for $n_s^* = 0.0038$).

These deviations are in agreement with the numerical simulation presented in [71]. There, a stronger background disorder with l_b being not too large compared with l_s causes a slower decay in magnetoresistivity. In our measurements, the interval in which α can be extracted corresponds to an interval of $\omega_c \approx \omega_0$ rather than as demanded $\omega_c \gg \omega_0$.

Phonon contributions might as well be a source of the deviations between the Mirlin model and experimental results. Therefore, the temperature dependency of α on the unimodal secondary 2DLGs with $n_s^* = 0.001$ and $n^* = 0.0038$ is determined (see Fig. 5.9 (a)); α decreases as the temperature increases by two orders of magnitude.

Comparing α at 1.4 K for different unimodal secondary 2DLGs, one finds it to increase as n_s^* increases. These data are presented in Fig. 5.9 (b). To summarize the influence of the secondary 2DLG as a source of static, random disorder on the magnetoresistivity of a primary 2DLG, the influences are significant. The conductivity changes with the magnetic field depending on the type of additional scattering:

At low magnetic fields (regime A), the secondary 2DLG adds retroreflective corridors such that the conductivity decreases with n_s^*. In the regime B of guided electron transport along the edges of

the 2DLG clusters, a reduction of $\sigma_{xx}(B)$ is found, while $\sigma_{xx}(B)$ increases in regime C. Here the localization transition caused by elevated magnetic fields is shifted to higher magnetic fields.
Comparing this behavior with a dynamic scattering contribution induced by a sufficient increase in temperature, similar results are found for regimes B and C. Therefore, it seems that the type of scattering that prevents the electron from localization or superdiffusive transport is independent of the correlation of the scattering events. For regime A, on the other hand, an increasing magnetoresistivity was found for an increased dynamic scattering contribution. Here, it seems that the additional scattering depins the electron from the scattering corridor and reduces retroreflectivity.
The character of the background scattering leads to qualitative different modifications of the magnetoconductance, where the sign of the modification depends on the magnetic field.
Further theoretical studies of the background scattering are desirable for completing the presented picture.

CHAPTER 6

EXPERIMENTS ON 2DLGS FORMED BY CIRCULAR OBSTACLES IN THE DILUTE LIMIT

Many theoretical publications on 2DLGs concentrate on systems with low dimensionless obstacle densities. [19, 23, 71, 127] Experimental studies by Bockhorn et al. interpreted the arbitrary distributed oval defects in high mobility samples as a dilute 2DLG [14, 33, 65].

Recent transport experiments on pristine high mobility GaAs/AlGaAs samples have shown giant negative magnetoresistance (GNMR), comprising a narrow peak on top of a broader structure, which is also centered around $B = 0$. [31, 66–68] The broader contribution depends highly on the temperature and additional in-plane magnetic fields.

Therefore, the aim of the present chapter is to systematically investigate the influence of low number of LG obstacles, forming a 2DLG, on the magnetoresistance. The 2DLG is lithographically defined with a specified density n^* and each circular obstacle exhibiting the same constant radius r. Thus, a controlled scattering potential is introduced. The term “low number of LG obstacles” means that n^* is in a regime in which the typical signatures occurring in high mobility 2DEG samples, such as GNMR, are still distinguishable from the 2DLG contributions. As detailed later, the dimensionless obstacle density lays in this regime below $n^* = 25 \cdot 10^{-3}$. The motivation behind this experimental study is to distinguish magnetoresistivity contributions originating from the 2DLG and pristine 2DEG. Therefore, different parameters such as two sample width w, four different n^*, different temperatures (between 80 mK to 32 K), and the in-plane magnetic fields $B_{||}$ are varied.

6.1 Sample design and experimental setups

Two samples were prepared to investigate the influence of dilute 2DLGs on magnetoresistivity. The sample widths were $w = 100\,\mu\mathrm{m}$ and $w = 20\,\mu\mathrm{m}$, whereas all other parameters were chosen to be the same. Each sample had five measurement fields with dimensionless obstacle densities n^* of:
$n^* = 0, 0.0031, 0.00625, 0.0125$ and 0.025. The sequence and values of n^* were the same for both samples. Each obstacle was defined by an etched circle (patterned with electron beam lithography) with a lithographic specification of 425 nm for its radius, resulting in an effective radius of $r = 500\,\mathrm{nm}$ with the lateral depletion length of 75 nm taken into account.
The mean-free paths ($l_{\mathrm{mfp}} = 1/(2r\,n_s)$) of the lithographically defined 2DLGs were as follows: l$l_{\mathrm{mfp}} = 80\,\mu\mathrm{m}$ ($n^* = 0.0031$), $l_{\mathrm{mfp}} = 40\,\mu\mathrm{m}$ ($n^* = 0.00625$), $l_{\mathrm{mfp}} = 20\,\mu\mathrm{m}$ ($n^* = 0.0125$) and $l_{\mathrm{mfp}} = 10\,\mu\mathrm{m}$ ($n^* = 0.025$), respectively. The plain field with $n^* = 0.00$ served as a reference. The two samples had different sample widths. The voltage probes in the longitudinal direction were spaced by $100\,\mu\mathrm{m}$ for both samples. The general definition of a 2DLG was applied to design the sample (i.e., a random distribution of the obstacle's center coordinates) with mutual obstacle overlap allowed. The random distribution of the obstacles was verified by a Voronoi tessellation of the cell areas. [140, 141]
The sample's host material was a GaAs/Al$_{0.3}$Ga$_{0.7}$As heterostructure, with the 2DEG situated 150 nm below the surface (see Subsection 2.3.1). After illumination with an infrared emitting diode, the electron density was $n_e = 2.5 \cdot 10^{15}\,\mathrm{m}^{-2}$. From the reference field a mobility of $\mu = 960\,\mathrm{m}^2/\mathrm{Vs}$ could be determined at liquid helium temperatures. This corresponds to a mean free path of $l_{\mathrm{mfp}} = 78\,\mu\mathrm{m}$. No electrodes were defined on the sample surface to avoid strain effects and reduced mobility. Therefore, the electron density was fixed to the value of $n_e = 2.5 \cdot 10^{15}\,\mathrm{m}^{-2}$. The left inset of figure 6.1 (d) depicts an electron beam microscopy image of a single LG-obstacle (with lithographic dimensions given). The right inset is an optical microscope image showing the complete structure of a typical sample.
The measurements were performed for temperatures below 1 K in a dilution refrigerator. Here, the minimum electron temperature was estimated to be 80 mK. Measurements performed at temperatures higher than 1 K were conducted in a variable temperature cryostat, where the sample was cooled by ^{4}He vapor (see Section 2.2 for further details of the measurement setup).
Because both cryostats were equipped with rotatable sample stages, it was possible to vary the in-plane magnetic field component. Measurement results of this experiment are further detailed in Section 6.3.

6.2 Interplay between GNMR and a dilute 2DLG

In Fig. 51, the magnetoresistivities of all samples are presented for temperatures between 80 mK and 800 mK. The results from the two dilute 2DLG samples are shown in part (a) ($w = 100\,\mu\mathrm{m}$) and part (b) ($w = 20\,\mu\mathrm{m}$). Part (c) of the figure depicts the magnetoresistivity of a sample with $w = 100\,\mu\mathrm{m}$, but with higher n^*, as indicated in the presentation.
For the $w = 100\,\mu\mathrm{m}$-wide sample and $n^* = 0$ (part (a), blue trace) the typical GNMR structure was

observed. A short review of GNMR in the literature can be found in Subsection 3.2.6. Very similar to the reports of Bockhorn et al. [14, 33] and Hatke et al. [66] a narrow peak, centered at $B = 0$ with a weak temperature dependency (see left inset in the upper right corner of Fig. 6.1 (a)) is observed. It is surrounded by a broader peak with a width of approximately ±80 mT. This peak is highly temperature dependent, as observed through comparing the 80 mK and 800 mK measurement traces. The other traces in the diagram are obtained from the 2DLG measurement fields. Fig. 6.2 (a) depicts the same data for $n^* = 0$, but shows the traces of $T = 200\,\mathrm{mK}$, 400 mK and 600 mK as well. As the temperature increases, the magnetoresistivity of the broader peak increases. After a drop in resistivity up to approximately 80 mT, the resistivity increases with the magnetic field.

Comparing this behavior to the magnetoresistivity of the dilute 2DLGs, a systematic evolution is observed.

As shown in Fig. 6.1 (part (a)), the temperature-independent interval of magnetoresistivity increases with n^*. The respective peak broadens with n^* and its amplitude increases linearly. The vertical lines mark the transition magnetic fields B_t, at which the magnetoresistivity traces of 80 mK and 800 mK do not fall onto each other anymore.

Therefore, one correlates the increase of the temperature-independent interval to the 2DLGs, which are patterned on the measurement arrays. This is in qualitative agreement with the studies of Bockhorn et al. [14], who stated that the small temperature independent peak of the plain 2DEG are caused by several oval defects. The oval defect assembly forms a 2DLG with low density, where the effective average diameter of a single obstacle is estimated to be in the range of 20 μm.

Besides residual oval defects that occur due to the growth process of the host material through the formation of Gallium droplets, boundary scattering at the Hall bar edges might contribute to the magnetoresistivity, which was also stated by Alekseev et al. [91]. From the measurement this becomes plausible as one compares the magnetoresistivity traces of the $w = 20\,\mu\mathrm{m}$-wide sample with no additional 2DLG (blue trace in 6.1 (b)) to the plain measurement field of the $w = 100\,\mu\mathrm{m}$-wide sample. For the narrower sample, the temperature-independent part of the magnetoresistivity has the shape of a double peak, with the minimum centered at $B = 0$.

The maxima positions are located at $B_{\mathrm{max}} = \pm 2.3\,\mathrm{mT}$ with a peak height of approximately 1 Ω. This feature is most likely caused by diffusive boundary scattering at the Hall bar edges. A zoom-in of the data is provided in the lower inset of Fig. 6.1 (b). As detailed in Subsection 3.2.5, the ballistic effect of the "wire-peak," first described by Thornton et al. [64], exhibits a maximum located at $w/r_c = 0.55$. With the experimental finding of the maxima location to be situated at $B_{\mathrm{max}} = \pm 2.3\,\mathrm{mT}$, one estimates the wire width w to be $w = 19.1\,\mu\mathrm{m}$. This is in agreement with the lithographic specification of $w = 20\,\mu\mathrm{m}$. The structure of the wire peak remains as the obstacle density n^* increases up to $n^* = 0.0125$, but its amplitude (i.e., the difference between the zero-field value and the value of the maximum) decreases. The phenomenon of the wire-peak is based on the fact that the dominant part of the diffusive electron scattering is at the Hall bar edges. With increasing n^* the scattering contribution from LG-obstacles located within the Hall bar bulk dominates over edge scattering.

etation and discussion in Section 4. The pa-
n a summary and our conclusions (Section

PARATION OF THE SAMPLES AND EXPERIMENTAL SETUP

l$_{0.3}$Ga$_{0.7}$As heterostructure with a 2DEG
the surface is prepared by molecular beam
r a brief illumination with an infrared light-
e, an electron density of $n_e = 2.5\times10^{15}\,\mathrm{m}^{-2}$
y of $\mu = 960\,\mathrm{m}^2/\mathrm{Vs}$ of the pristine 2DEG is
at liquid helium temperatures, correspond-
ctronic mean free path of $\ell_e = 78\,\mu\mathrm{m}$. In
d strain and hysteresis effects which can de-
bility, Schottky-type electrodes on the sam-
re avoided.

cle arrays are patterned by electron beam
and subsequent reactive ion etching. Each
esponds to an etched circle with a geometric
nm, Fig. 1 (d). Random distribution is en-
erating the center coordinates of the circles
n number generator, and the correct distri-
fied by a Voronoi tesselation of the array and
check of the distribution function for the
areas.[20,21]. Here, we allow mutual overlap
es, in accordance with the assumptions un-
widely used theoretical results for the mag-
t of 2DLGs.[15,22–24] A picture of a typical
ell as a close-up of one individual obstacle
the inset of Fig. 1 (d). Since the analysis of
hm oscillations at large magnetic fields in-
al electronic depletion length of ≈ 75 nm,[25]
electronic obstacle radius is $r_s \approx 500nm$.
magnetoresistivity experiments on antidot
ared from this wafer by the same method
hat the electrostatic potential at the obsta-
steep,[26] and can be approximated by hard
imensionless number density of a 2DLG is
$\equiv n_s r_s^2$. It measures the fraction of the
covered by the obstacles in the absence of
ap. The corresponding mean free path of
LG is $\ell_s \equiv (2n_s r_s^{-1})$.[17]
of the Hall bar between the voltage probes
width w was 100 μm. Since the GNMR
depend on the width w of 2DEG as well,
rrays up to $n^\star = 25\times10^{-3}$ have also been
in Hall bars of 20 μm width, with otherwise
ameters.
ments were carried out in a dilution refrig-
base temperature of 8 mK. The minimum
erature is estimated to ≈ 80 mK which can
up to ≈ 800 mK without destabilizing the
it. For larger temperatures, a ^{4}He gas flow
a variable temperature insert and a base
of 1.4 K is used. For the data presented be-
urrent (500 nA, 17.7 Hz) is injected into the

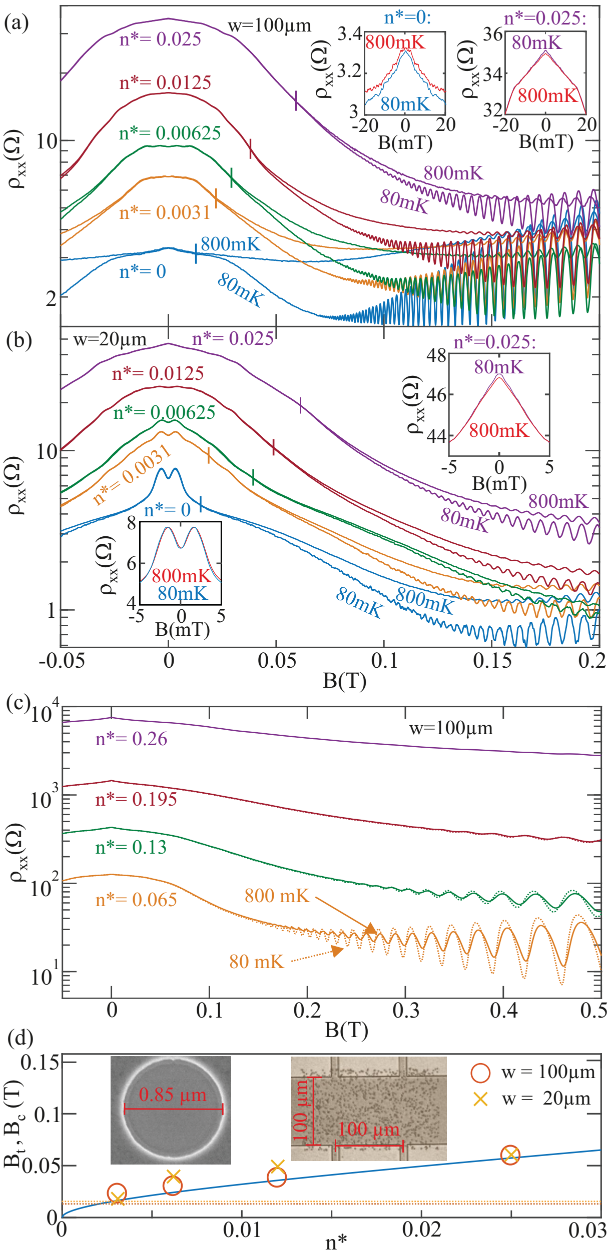

FIG. 1. (color online) Magnetoresistivities of the arrays for different values of $n^\star$ and for two Hall bar widths w, in particular small $n^\star$, $w = 100\,\mu m$ (a), small $n^\star$, $w = 20\,\mu m$ (b) and large $n^\star$, $w = 100\,\mu m$ (c). Insets: zoom-ins of $\rho_{xx}(B)$, the magnetoresistance close to B=0 and its temperature dependence for selected samples. The traces are measured at base temperature (≈ 80 mK) and at 800 mK are shown for each case. The short vertical lines in (a) and (b) indicate the magnetic field B_t above which a temperature dependence can be resolved. (d) The measured values for B_t as a function of $n^\star$, in comparison to the lower percolation threshold $B_c(n^\star)$ of the 2DLG (full line). The inset shows a scanning electron microscope picture of a single etched circle of 425 nm nominal radius (left) and an optical microscope picture of one exemplifying Lorentz array with density $n^\star = 1.25\times10^{-2}$ (right).

Figure 6.1: Magnetoresistivities of the three samples (a) $w = 100\,\mu\mathrm{m}$ (low n^*), (b) $w = 20\,\mu\mathrm{m}$ (low n^*), and (c) $w = 100\,\mu\mathrm{m}$ (high n^*), with n^* as indicated in the figure. The insets are zoom-ins of selected traces for a narrow interval centered at $B = 0$. For each n^* and w, $\rho_{xx}(B)$ is presented for the lowest temperature of ≈ 80 mK and for 800 mK. The vertical lines mark the magnetic field B_t after which the magnetoresistivity increases with temperature. For high n^*, presented in (c), the difference is almost unresolvable within this temperature interval. Part (d) presents the measured values of B_t against n^* for both Hall bar widths. The blue trace is the analytical expression from [18], which is in good agreement with the experimentally obtained values. The horizontal lines mark B_t of the plain 2DEG samples of both Hall bar widths. The insets depict a single LG-obstacle with its lithographic dimensions (left) and an optical microscope picture of the sample with $n^* = 1.25\cdot10^{-2}$, $w = 100\,\mu\mathrm{m}$.

At a dimensionless obstacle density of $n^* = 0.025$, the magnetoresistivity trace has a shape similar to the $w = 100\,\mu\text{m}$-wide sample with the same n^*. This is reasonable considering that the 2DLG mean free path is $l_{\text{mfp}} = 10\,\mu\text{m}$ for $n^* = 0.025$ (i.e., below the Hall bar width). The small peak around zero-magnetic field of the 2DEG sample with $w = 100\,\mu\text{m}$ might, with these findings in mind, also be caused by edge scattering. The wire peak position is inversely proportional to w: $B_{\text{max}} \propto 1/w$. Therefore, B_{max} shifts toward $B = 0$ and might not be resolved for the $w = 100\,\mu\text{m}$ sample, in contrast to the $w = 20\,\mu\text{m}$ sample.

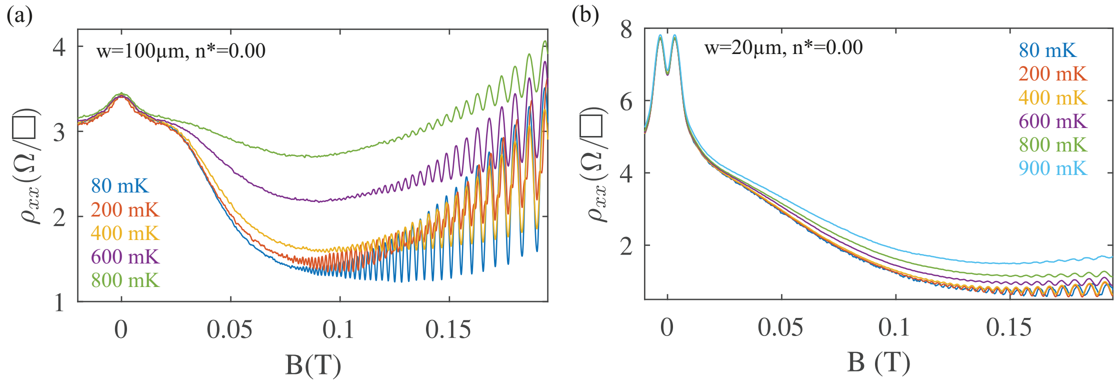

Figure 6.2: Temperature dependency on the magnetoresistivity of the pristine 2DEG measurement-fields for (a) $w = 100\,\mu\text{m}$ and (b) $w = 20\,\mu\text{m}$. Close to $B = 0$, a temperature-independent interval caused by scattering at the Hall bar walls and at residual background impurities such as oval defects is observed. At higher magnetic fields, GNMR with its characteristic bell shape and its characteristic reduction is observed with increasing temperature.

The temperature evolution of the $w = 20\,\mu\text{m}$-sized sample is similar to that of the $w = 100\,\mu\text{m}$-wide sample. The vertical lines in Fig. 6.1 (b) mark B_t. B_t shifts for the same n^* to slightly higher magnetic fields for the narrower sample compared with the broader sample. For comparison, these B_t are presented against n^* for both Hall bar widths in part (d) of Fig. 6.1. The solid blue line marks the classical lower percolation threshold field $B_c(n^*)$ of a clean 2DLG (for a detailed explanation, see Section 3.3). $B_c(n^*)$ can be understood in terms of an effective B-dependent obstacle radius, outlined by Kutzmany and Sphon [18], and is given by

$$B_c(n^*) = \frac{\hbar}{e}\sqrt{2\pi n_e}\cdot\frac{1}{r}\cdot\frac{\sqrt{n^*}}{\sqrt{0.359}-\sqrt{n^*}} \tag{6.2.0.1}$$

A remarkable agreement between the analytical expression of equation 6.2.0.1 and the experimental data is found. The slight variations for the $w = 20\,\mu\text{m}$-wide sample might be caused by the scattering at the Hall bar edges. The horizontal lines in the figure mark B_t of the plain 2DEG-measurement fields obtained from the experimental traces. From the points of intersection with the curve of equation 6.2.0.1, the dimensionless obstacle density of oval defects is estimated to be $n^* \approx 0.005$, which is in the same order of magnitude as the experimental findings of Bockhorn et al. [14].

The above described phenomenology suggests that the narrow component of the GNMR with its weak temperature dependency is dominated by strong scattering processes. It is possible to extend the magnetic field range in which the temperature-independent part of the magnetoresistivity exists using the corresponding increase in scattering potential. In this study, it is formed by the 2DLG-array in combination with edge scattering and unknown intrinsic contributions.

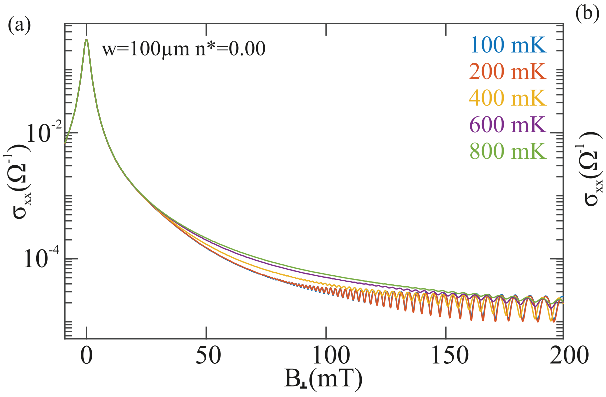

Figure 6.3: (a) Magnetoconductivity of the sample with $w = 100\,\mu\mathrm{m}$, $n^* = 0.00$ for different temperatures below 1 K. (b) The same representation as in (a) but for the sample with $w = 100\,\mu\mathrm{m}$ and $n^* = 0.025$. Because $\sigma_{xx}(B)$ exhibits a negative slope around $B = 0$ for both samples, weak localization contributions to the magnetotransport can be excluded. With $B > 50\,\mathrm{mT}$, σ_{xx} increases with T for both samples, indicating activated transport in this regime.

Above the transition magnetic field B_t, the magnetoresistivity depends strongly on the temperature. B_t was found to be similar to the percolation magnetic field B_c. For magnetic fields above B_c, the magnetotransport is in the regime of localized electron orbits encircling a single hard-core scattering center or an assembly of them.

In a clean 2DLG without additional scattering, all electrons are localized if they are exposed to a magnetic field higher than B_c. Their trajectories are skipping orbits around a single obstacle or a cluster thereof. If the system is under these conditions, the electron transport exhibits an activated character in experiments. An additional scattering event disturbs the localized trajectory and the electron is depinned from its undisturbed motion. This is experimentally proven by the fact that the magnetoconductivity σ_{xx} increases as the temperature is increased. The data from Fig. 6.1 (a) are thus transformed by $\sigma_{xx}(B) = \rho_{xx}(B)/(\rho_{xx}^2(B) + \rho_{xy}^2(B))$. This is presented in Fig. 6.3. $\sigma_{xx}(B)$ decreases as a magnetic field is applied. Weak localization should cause an increase of $\sigma_{xx}(B)$ as B increases because the magnetic field reduces coherent backscattering. [142] Therefore, weak localization contributions in the magnetotransport can be excluded. Moreover, the representation of σ_{xx} against B proves that the electron transport is activated by temperature because the conductivity increases at elevated B with higher T.

The small temperature-independent part of the GNMR

The small narrow peak of the GNMR is often interpreted as an intermixing of different disorder scattering contributions. [23, 35] Bockhorn et al. [14] applied this model on their experimental data in great detail. For a detailed presentation of this analysis, the reader is revered to Subsection 3.3.2. The negative magnetoresistivity is explained within this model (for magnetic fields below the percolation threshold) to be caused by skipping electron trajectories between LG obstacles. Weak background scattering disturbs this, and the peak can be modeled using equation 3.3.2.1, which predicts a parabolic dependency:

$$\rho_{xx}(B) \propto -B^2 \tag{6.2.0.2}$$

From the fit of the experimental data to equations 3.3.2.1 and 3.3.2.4, one is able to determine the obstacle density n_s. As detailed in Subsection 3.3.2, the scattering times of the weak background disorder τ_L and the hard-core scattering τ_s can be directly determined from the experimental data. The fits of equation 3.3.2.1 are performed for the interval $B \leq B_t$. The fit parameter is the obstacle density n_s. For the study presented here, it is therefore possible to compare the lithographic specifications of n_s for the different 2DLGs with the results from the analysis.

The results from the fits are shown in Fig. 6.4 at the 2DLGs with $n^* = 0$ (part (a)), $n^* = 0.0031$ (part (b)), and $n^* = 0.0125$ (part (c)). The peak of the $n^* = 0$ does not show a parabolic shape. Still, the obtained fit value of $n_s = 2.8 \cdot 10^8\,\mathrm{m}^{-2}$ is a reasonable value compared with the literature. [14] The parabolicity of the magnetoresistivity peaks improves with n^*. The fit values for n^* are smaller than the lithographic specifications. For the 2DLG with $n^* = 0.0031$ (lithographic design), the fit value is a factor of 7.4 smaller. From the 2DLG with $n^* = 0.0125$ a fit value that is too small by 2.8 is obtained. For $n^* = 0.025$, the ratio between the lithographic design and fit value drops to 1.68. The observation of the fit results being more accurate as n^* increases might be because of the reduced relevance of edge scattering. This means for the Hall bar width that it is: $w \gg n_s^{-0.5}$.

To conclude, the applicability of the fit as proposed by Bockhorn et al. [14] is restricted at low n^* by scattering contributions other than scattering at LG-obstacles. One dominant scattering contribution originates from the edges. Therefore, the fit is more accurate as n^* increases. On the other hand, with increasing n^*, the validity of Mattheisen's rule is hardly valid because of increased memory contributions such as the corridor effect. [141]

In the regime of elevated n^*, where kinetic models are not applicable [15] ($n^* \lesssim 0.025$), the magnetoresistivity evolves a structure that resembles GNMR features (see Fig. 6.1, part (c)). A narrow peak around $B = 0$ is on top of a broader shoulder. This structure has a zero-field resistivity much higher than that of GNMR. The broader part of the magnetoresistivity with elevated n^* is temperature stable, which is in strong contrast to the GNMR shoulder, and moreover it is not influenced by an in-plane magnetic field. The GNMR shoulder on the other hand vanishes with $B_{||}$ (see Subsection 3.2.6). The shape of the magnetoresistivity of 2DLGs with elevated n^* has been explained in terms of classical

memory effects. [15, 19, 21, 23, 71] Schluck et al. [141] explained the small peak on top in terms of retroreflection at Lorentz obstacles. This causes an almost linear negative magnetoresistivity.
From the results of the present study, a systematic suppression of the temperature-dependent GNMR with increasing density of strong scatterers is observed.

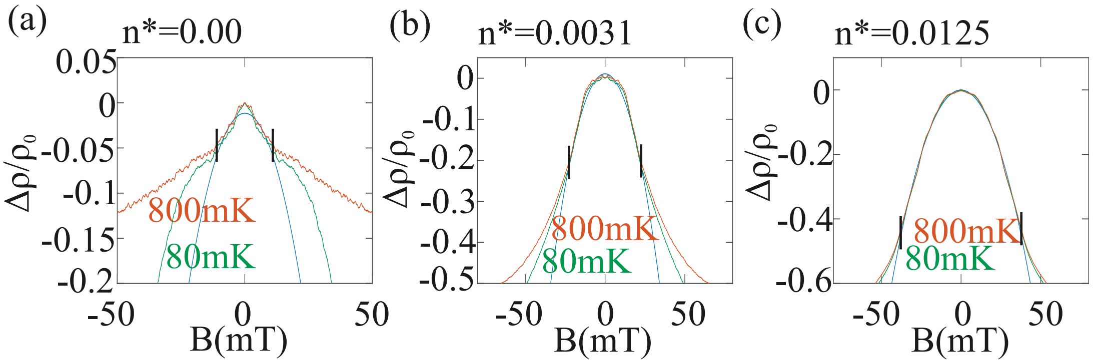

Figure 6.4: Parabolic fits (in blue) of the narrow peaks to the $\rho_{xx}(B)$-traces at 80 mK for $n^* = 0.00$ (a), $n^* = 0.0031$ (b), and $n^* = 0.0125$ (c). The fit interval corresponds to temperature-independent B-fields, marked by vertical lines. The 800 mK traces are shown as well.

The broad temperature-dependent part of the GNMR

The shoulder of the GNMR, which is highly dependent on the temperature for the interval below 1 K, can be explained by the model of an interaction-induced correction in the presence of long- and short-range disorder. [143] Hatke et al. [66] and Bockhorn et al. [33] analyzed their experimental data along the lines of this model (see Subsection 3.2.6).
The model of interaction-induced correction predicts a parabolic and temperature dependent magnetoresistivity, which is given by

$$\frac{\rho_{xx}(B)}{\rho_{xx}(0)} = 1 - \beta \frac{c_0}{2 n_e^2 \pi^2 \sqrt{\hbar k_B T \tau}} \tag{6.2.0.3}$$

Here, $c_0 \approx 0.276$ is a numerical constant; n_e denotes the electron density; k_B is the Boltzmann constant; T is the temperature; and τ is the Drude scattering time. β, which determines the opening of the parabolic temperature-dependent GNMR part, is defined using

$$\beta = \frac{4\sqrt{\tau/\tau_q}}{k_F d} \tag{6.2.0.4}$$

where τ_q is the quantum scattering time, k_F is the Fermi wave vector, and d denotes the distance between the 2DEG and the δ-doping layer. In the samples presented in this study, $d = 40$ nm. For the pristine 2DEG with $\tau = 290\,\mathrm{ps}$ and $\tau_q = 3.5\,\mathrm{ps}$, one expects $\beta = 7.2$.

The data are fitted to equation 6.2.0.3, which is presented in Fig. 6.5. In blue, the normalized resistivity change to the zero-field value $\Delta\rho/\rho_0$ is depicted, and the red parabolas are fits to the data in the intervals marked by the black vertical lines.

From the fit of the sample with $w = 100\,\mu\mathrm{m}$, β is found to deviate by a factor of 1.65 from the expected 7.2. At 800 mK, the magnetoresistivity trace is hardly a parabola, but the value of the fitted β deviates only by 0.85 from the expected one.

As n^* increases the shoulder of the temperature-dependent GNMR part broadens, but a parabola to which the model can be fitted is not discernible. This is visible in Fig. 6.5 (c). Possible reasons for the deviations from a parabolic characteristic are the increasing contributions from hard scatterers. Moreover, the $\vec{E} \times \vec{B}$ drift at the sample edges has a higher contribution because the relevant regime is shifted to higher$B$-fields. Another reason for the nonvalidity of the model of interaction-induced correction in the presence of long- and short-range disorder can be that even the lowest nonvanishing value of $n^* = 0.0031$ is too large for equation 6.2.0.3 to hold. Despite these considerations, the fit value for β is comparable to the one found for $n^* = 0$.

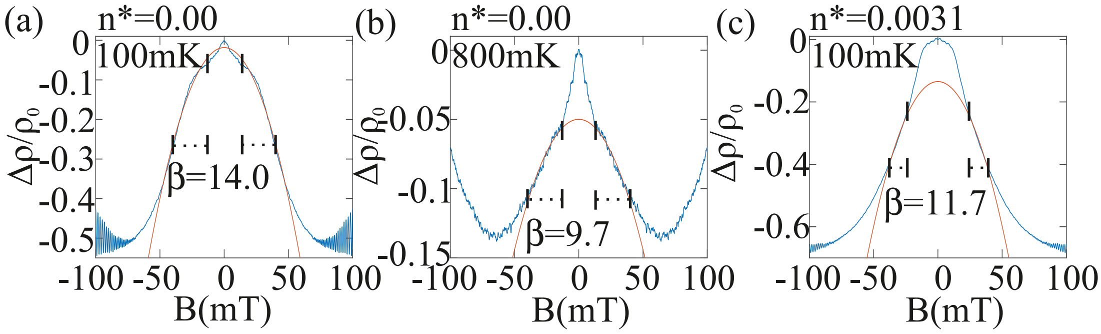

Figure 6.5: Parabolic fits (in orange) to the temperature-dependent part of the GNMR, with β, the opening of the parabola, as the fit parameter. The fit intervals are marked by the vertical lines. (a) Relative difference $\Delta\rho/\rho_0$ for $T = 100\,\mathrm{mK}$ vs. B (blue) and the resulting fit function (red). (b) The same representation as for (a) at 800 mK. (c) The same representation for $n^* = 0.0031$ at 100 mK.

6.3 GNMR modified by a dilute 2DLG in parallel magnetic fields

In the same magnetic field interval in which the magnetoresistivity trace shows a high temperature dependency (the temperatures being below 1 K), an in-plane magnetic field $B_{||}$ also modulates the magnetoresistivity significantly.

Reported experimental results [14, 66] were obtained by measuring the longitudinal magnetoresistance in tilted B-fields. Here, the total amount of B_{tot} is varied, while the sample is tilted at a certain, constant angle α with respect to the magnetic field lines. One major disadvantage of this experimental setup is that both components of the magnetic field (in-plane $B_{||}$ and perpendicular $B_{\perp}$ to the sample surface) are reduced simultaneously while B_{tot} is decreased.

To compare the measurements from the literature to results from the samples used in the present study, the same experimental setup was implemented, and the results are presented in Fig. 6.6. As indicated in the figure, the sample was maintained at a constant angle α, while the total magnetic field B_{tot} was changed in an interval of approximately −2 T to 12 T. The respective value for$B_{\perp}$ is recalculated and represented on the x-axis of the diagram, and the same phenomenology as that observed by Bockhorn et al. [14] and Hatke et al. [66] is found (see Subsection 3.2.6 for a short summary).

From the measurement, it becomes clear that the bell shape of the broad GNMR part is highly diminished by the in-plane component of the total magnetic field B_{tot}. Here, the traces are only qualitatively comparable because $B_{||}$ reduces with$B_{\perp}$.

To modify the two perpendicular B-field components independently, a second magnet (perpendicularly aligned to the first one) can be used.

Another option, which was used for the results presented here, is to rotate the sample by small steps of α in a constant B_{tot}. Here, the sample is aligned almost parallel to the magnetic field lines at high magnetic fields in the range of a few Tesla.

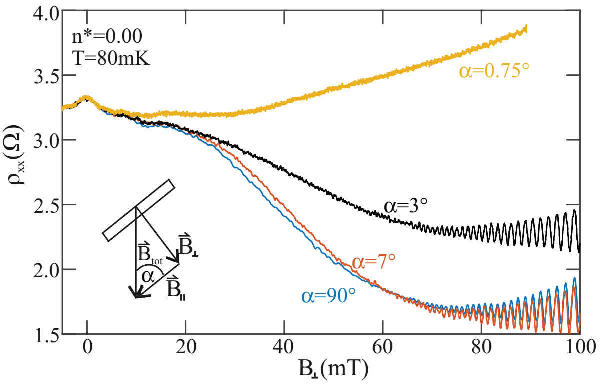

Figure 6.6: Longitudinal magnetoresistivity of the tilted sample ($n^* = 0.00$, $w = 100\,\mu$m) for different angles α. With decreasing α the $B_{||}$ contribution of B_{tot} increases, showing that the negative slope of GNMR diminishes.

The in-plane magnetic field component is given by $B_{||} = \cos(\alpha) \cdot B_{\mathrm{tot}}$. The perpendicular component of the magnetic field is: $B_\perp = \sin(\alpha)\cdot B_\mathrm{tot}$. For small angles it follows for the two components: $B_\perp = \sin(\alpha)\cdot B_\mathrm{tot} \approx B_\mathrm{tot}\alpha$ and $B_{||} = \cos(\alpha)\cdot B_\mathrm{tot} \approx B_\mathrm{tot}$. The inset of Fig. 6.6 illustrates the vector decomposition.

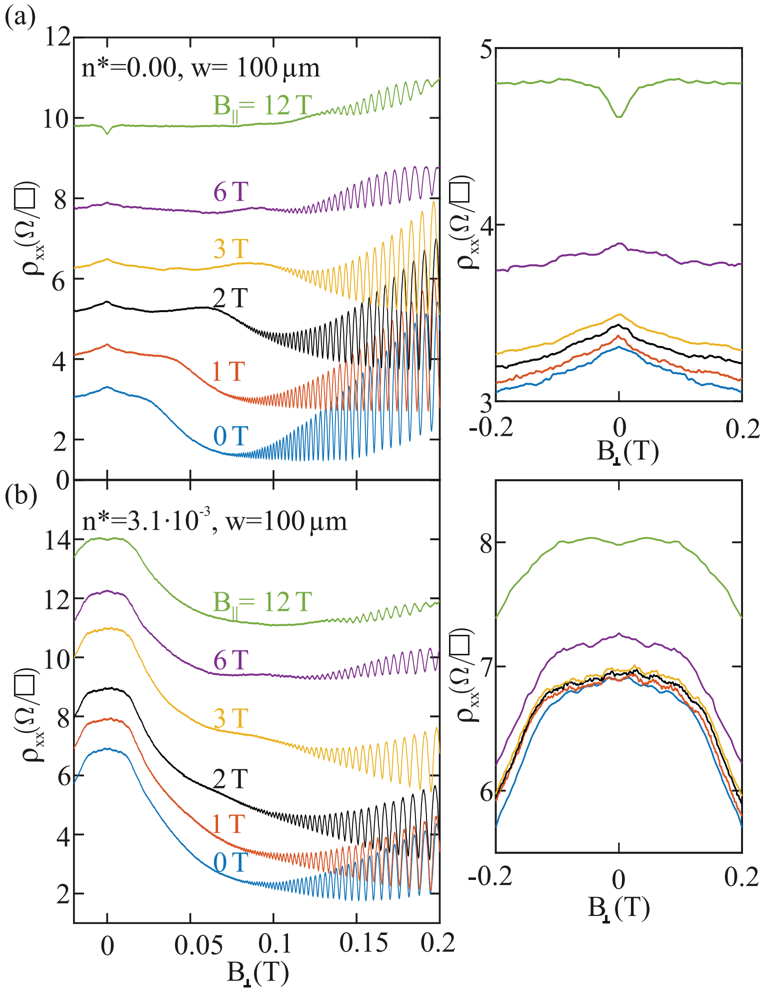

Figure 6.7: Dependency of the magnetoresistance on the in-plane magnetic field $B_{||}$ of (a) the $n^* = 0$ sample and (b) the $n^* = 0.0031$ sample. For both samples, the width is $w = 100\,\mu\mathrm{m}$. Adjacent traces have an offset of $1\,\Omega$ for clarity. The right parts of (a) and (b) are zoom-ins of the data with no offset.

Therefore, it is possible to measure $\rho_{xx}(B_\perp)$ with $B_{||}$ as an independent parameter. The small angle approximation is valid here. For example, with $B_\mathrm{tot} = 10\,\mathrm{T}$, a perpendicular magnetic field of $B_\perp = 300\,\mathrm{mT}$ corresponds to a rotational angle of $\alpha = 1.7°$. At this angle, the in-plane component is $B_{||} = 9.995\,\mathrm{T}$. The magnetoresistivities of the plain 2DEG and the 2DLG with $n^* = 0.0031$ are presented in Fig. 6.7 (both for the $w = 100\,\mu\mathrm{m}$-wide Hall bar). Each adjacent trace was offset by $1\,\Omega$ for the sake of clarity. As the in-plane magnetic field increases, the negative slope of the GNMR reduces (for $B_{||} = 1\,\mathrm{T}$) and changes to a positive slope for elevated in-plane $B_{||}$-fields. This behavior is observed for

both measurement fields, the plain 2DEG (part (a)) and the 2DLG with $n^* = 0.0031$ (part (b)).
Similar results to the $n^* = 0.00$ and $w = 100\,\mu\text{m}$ case were observed in the studies of [144]. There, the focus was on the influence of $B_{||}$ on MIRO, which is why the results obtained in darkness were left undiscussed in that work.
The magnetoresistivity remains essentially unchanged by the influence of intermediate $B_{||}$ in the same magnetic field intervals, which are observed to be temperature-independent. The right-hand side of Fig. 6.7 (a) and (b) are zoom-ins close to $B_\perp = 0\,\text{T}$. Here, the traces do not have an offset and it is visible that the zero-field resistivity slightly increases with $B_{||}$.
For $B_{||} = 12\,\text{T}$, a dip is observed for $\rho_{xx}(B_\perp = 0)$ $(n^* = 0.00)$. This can be explained by the parabolic positive magnetoresistivity of systems with two sub-bands. [145] Here, this is realized by spin splitting, which also causes modulations of the SdHo (see, for example, the traces with $B_{||} = 12\,\text{T}$ above $B_\perp = 200\,\text{mT}$).
The increase of $\rho_{xx}(B_{||})$ for $B_\perp = 0$ is almost parabolic. The respective percentual change with respect to $\rho_{xx}(B_{||} = 0)$ is presented in Fig. 6.8 (a). The quantum scattering time τ_q is found to decrease with increasing $B_{||}$ (see Fig. 6.8 (b)). τ_q is determined from the envelope of the SdHo along the lines of [146]. Similar behavior is also observed for the 2DLGs with $n^* = 0.0031$ for $\rho_{xx}(B_{||}, B_\perp = 0)$ and $\tau_q(B_{||})$.

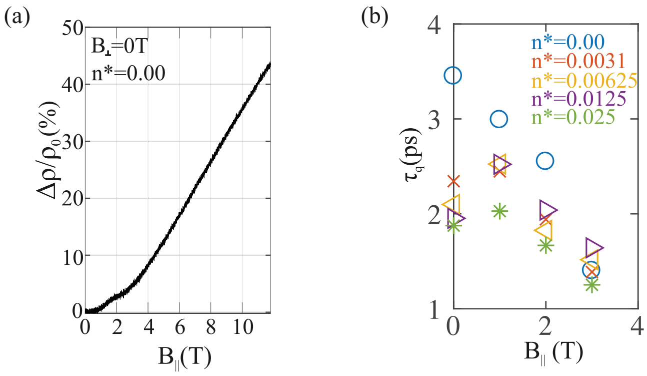

Figure 6.8: (a) $\Delta\rho_{xx}/\rho(B = 0)$ at $B_\perp = 0$ represented against $B_{||}$. An almost parabolic increase of the zero-field resistivity is observed as $B_{||}$ increases, indicating that the scattering at the quantum well boundaries increases with $B_{||}$. This is confirmed by (b). Here, τ_q is depicted against $B_{||}$, showing a decrease of τ_q with $B_{||}$ for all n^*. Both diagrams show results of the $w = 100\,\mu\text{m}$ wide sample.

Therefore, it can be stated that moderate $B_{||}$ values increase scattering rates, leading to increased resistivities. Modifications of the $\rho_{xx}(B_\perp)$-shape are mainly observed in the temperature-dependent interval.
These findings are independent of the Hall bar width. Fig. 6.9 (a) presents the measurement on the plain 2DEG with $w = 20\,\mu\text{m}$. The same phenomenology is observed as that for the $w = 100\,\mu\text{m}$ plain 2DEG. The interval near $B_\perp = 0$ is only slightly modified by $B_{||}$, while the GNMR peak reduces with in-plane magnetic fields.

With increasing n^*, one observes, similar to the investigations on temperature influences, that the middle peak remains mainly unchanged by $B_{||}$, whereas for elevated $B_\perp$ the GNMR peak reduces with $B_{||}$. The interval of the middle peak increases with n^*. See Figs. 6.7 and 6.9 (b) for comparison.

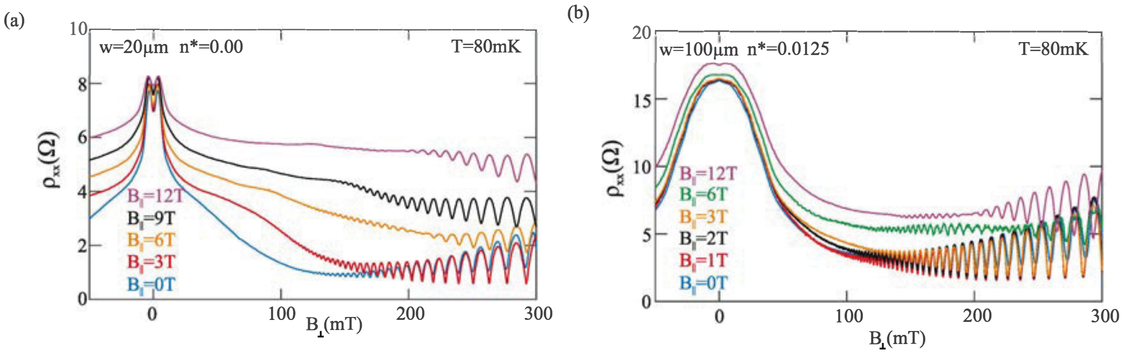

Figure 6.9: (a) $\rho_{xx}(B_\perp)$ of the $w = 20\,\mu$m-wide sample with different in-plane magnetic fields $B_{||}$. Close to zero in the same interval in which the magnetoresistivity is temperature-independent, only a small modulation is found, which is in strong contrast to the regime in which the GNMR bell shape occurs. Here with increasing $B_{||}$, $\rho_{xx}(B_\perp)$ increases. (b) The same representation as in (a) but for the sample with $n^* = 0.0125$ and $w = 100\,\mu$m. Because of the increased electron scattering at LG obstacles, the $B_\perp$-interval which is independent of $B_{||}$ broadens, while the modulation of the GNMR-dominated $B_\perp$-field interval remains qualitatively the same.

Different to the influence of temperature on GNMR, a model for the influence of $B_{||}$ on mixed disorder influenced 2DEG samples does not exist. Therefore, the influence of $B_{||}$ is only interpreted in a qualitative manner. In Fig. 6.8 (part (b)) the evolution of the quantum scattering time τ_q is presented against $B_{||}$ for the plain 2DEG and the dilute 2DLGs of the sample with $w = 100\,\mu$m. τ_q is strongly reduced by the in-plane magnetic field.

Heisz et al. [147] theoretically studied the position of the electron wave function in the growth direction of a heterostructure, which depends on the in-plane magnetic field as well as on the direction-averaged transport scattering time. The latter does not only depend on the quantum scattering time. It decreases because of scattering contributions from wave vectors, which can be caused by a displacement of the wave function toward the remote delta doping layer. Finite values of $B_{||}$ displace the wavefunction toward this layer, and therefore the scattering times reduce not only by the perpendicular B-field component but also the in-plane B-field. This is a plausible explanation for the experimentally observed reduction of τ_q with $B_{||}$ shown in Fig. 6.8 (part (b)).

As stated in [147], these evolutions also cause a positive magnetoresistivity with increasing $B_{||}$, while the perpendicular magnetic field is maintained at zero. This is also experimentally observed in the presented data of Fig. 6.8 (part (a)). With both magnetic field components exposed to the sample, a positive magnetoresistivity is also expected. This is observed in the experiment for all samples, as shown in Fig. 6.7.

Although models describing the effect of $B_{||}$ on the broad peak of GNMR are lacking, it is plausible that the peak's broadening by an in-plane magnetic field is caused by decreased scattering times. Other effects resulting from $B_{||}$ such as Zeeman splitting might cause the nonmonotonous shape of the magnetoresistivity in elevated in-plane magnetic fields.

The experimental studies presented in subsection 3.2.6 found the broad GNMR peak to depend on the sample's Hall bar width w. A rough scaling with $1/\sqrt{w}$ is proposed.

Comparing the nonpatterned samples of $w = 100\,\mu\text{m}$ and $w = 20\,\mu\text{m}$ with $n^* = 0$, the same phenomenology concerning the scaling of the peak broadness in $B_\perp$ is found. On the other hand, as n^* increases, the ratio of the peak widths for the same n^* approaches 1. As detailed with regard to the wire peak [64], the contribution of scattering at the sample edges decreases with increasing n^*. This indicates that the dependence of the GNMR on w is mainly caused by scattering at the sample edges. From the sample with $w = 20\,\mu\text{m}$ and $n^* = 0$, a τ_q of 2.2 ps is found. This is a factor of almost 2 smaller than for the sample with $w = 100\,\mu\text{m}$. Therefore, decreasing w by a factor of 5 causes a similar effect, similar to increasing $B_{||}$ to 2 T. This also indicates that the reduced τ_q of the narrower sample is caused by scattering at the sample edges.

To sum up the influence of an in-plane magnetic field on the discussed samples, an interval in which no pronounced dependency is observed was found. This interval is the same as that in which the GNMR is temperature-independent and increases with n^*. With $B_\perp$ being higher than the upper boundary of this interval but below the onset of the SdHo, the GNMR shoulder shows a high dependency on in-plane magnetic fields. This is attributed to higher scattering contributions of the wave vectors, caused by a reduced distance of the electron wavefunction to the delta-doping layer. This increased scattering is observed in an increased zero-field resistivity ($\rho_{xx}(B_\perp = 0, B_{||})$) and a reduction of the quantum scattering time τ_q.

6.4 Temperature evolution of the dilute 2DLG and a comparison with the hydrodynamic model

The term GNMR describes the magnetoresistance of pristine 2DEG samples with the phenomenology described in Subsection 3.2.6. In the previous chapters, both parts of the GNMR the small temperature and in-plane magnetic field-independent part and the broader part, which conveys a strong dependency on both parameters were discussed. It was reported how a dilute 2DLG influences the GNMR phenomenology. Alekseev [91] claimed to have described the GNMR using the hydrodynamic model. The measurements from Shi et al. [68] are taken as experimental counterparts to prove the hydrodynamic electron flow.

When comparing the experimental phenomenologies of other studies on the GNMR [14, 32, 66, 148], the following questions are found to remain open: Why does the peak in magnetoresistivity measured by Shi et al. [68] not depend on in-plane magnetic fields? Why is the temperature interval in which the hydrodynamic model can be applied in the range of a few Kelvin (1-30 K in [68]), while the usually observed peak is not visible in this interval any more [31]? Instead, at temperatures below 1 K, GNMR characteristics are observed.

Recent publications [88–90] that have proposed agreement between experiments and the hydrodynamic model have been based on measurements on long and narrow Hall bar samples in temperature intervals above 1 K and below 30 K. The hydrodynamic regime is realized by the geometry of a long and narrow Hall bar. On the other hand, due to this sample geometry, contributions from edge scattering are enhanced. In [88] (Fig. 1) clear signatures of the wire peak (see Subsection 3.2.5) are seen. This indicates that specular scattering at the sample boundaries also contributes to the magnetoresistivity. In this section, fits of the magnetoresistivity traces of dilute 2DLGs in accordance with the expressions of the hydrodynamic model [34] are provided using the following two expressions:

$$\rho = \frac{m^*}{e^2 n\tau}\frac{1}{1-\tanh(\xi)/\xi} \tag{6.4.0.1}$$

$$\xi = \sqrt{\frac{3\tau^*}{\tau}\left[1+(2\omega_c\tau_2)^2\right]} \tag{6.4.0.2}$$

Here, τ, τ^* and τ_2 are fitting parameters. The magnetoresistivity $\rho(\omega_c)$ is taken from measurement, with $\omega_c = eB/m^*$ denoting the cyclotron frequency.

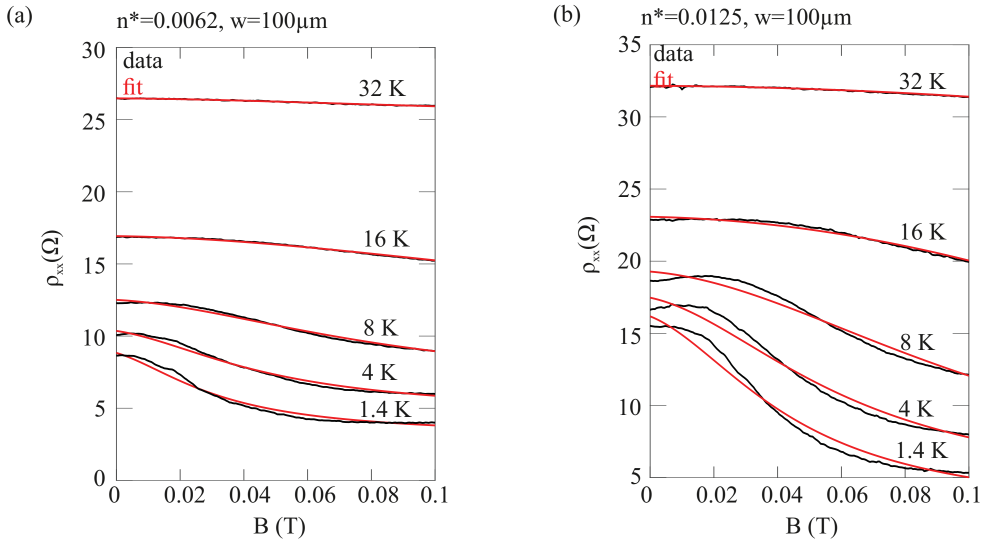

Figure 6.10: Experimental magnetoresistivity traces (shown in black) and their fits to equations 6.4.0.1 and 6.4.0.2. (a) Representation for the w = 100 µm-wide sample with n^* = 0.0062. (b) The same diagram for the sample but with w = 100 µm and n^* = 0.0125.

Figs. 6.10 and 6.11 present comparisons between the fitted curves and measurement results. The 2DLG samples with w = 100 µm (presented in Fig. 6.10) show better agreement in magnetoresistivity as the temperature increases. For both densities under investigation ($n^* = 0.0062$, part(a)) and ($n^* = 0.0125$, part (b)) τ decreases with increasing temperature, such as the sample with $n^* = 0.0062$ for the first fitting parameter decreasing from $\tau(1.4\mathrm{K}) = 426.5\,\mathrm{ps}$ to $\tau(32\mathrm{K}) = 0.385\,\mathrm{ps}$. A similar evolution is observed for τ_2 (from $\tau_2(1.4\mathrm{K}) = 3.9\,\mathrm{ps}$ to $\tau_2(32\mathrm{K}) = 0.28\,\mathrm{ps}$) and for τ^* (from $\tau^*(1.4\mathrm{K}) = 68.6\,\mathrm{ps}$ to $\tau^*(32\mathrm{K}) = 2.9\,\mathrm{ps}$).

In the same manner as Fig. 6.11, Fig. 6.10 presents results for the samples with $w = 20\,\mu\mathrm{m}$, $n^* = 0.0062$ (part (a)) and $w = 20\,\mu\mathrm{m}$, $n^* = 0.0125$ (part(b)). Due to the narrow sample width, contributions of the wire peak can be identified at $B \approx 3\,\mathrm{mT}$, while for elevated B, agreement between the fitted and measured traces is found. Additionally, for the$w = 20\,\mu\mathrm{m}$-wide sample, one observes better agreement as the temperature increases with a decreasing standard deviation.

In conclusion, it can be said that at elevated temperatures (above ≈ 4 K), the hydrodynamic model proposed by Alekseev [34, 91] provides agreement with the magnetoresistivity of dilute 2DLGs. This is surprising because additional LG-obstacles and phonons must promote electron–electron scattering as a consequence of the agreement to the hydrodynamic model.

Moreover, it can be stated that the peaks caused by the 2DLGs are not GNMR peaks following the original descriptions with the phenomenologies detailed in Subsection 3.2.6. This is especially proven by their independence from in-plane magnetic fields (see Section 6.3) and their independence from temperatures below 1 K.

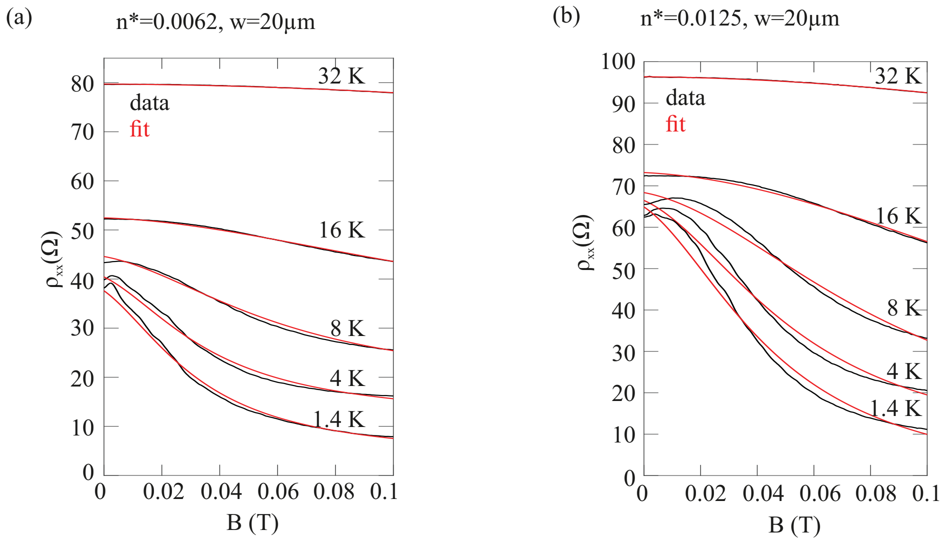

Figure 6.11: The same representation as in Fig. 6.10 but for the samples with $w = 20\,\mu\mathrm{m}$ and $n^* = 0.0062$ part (a) and with $w = 20\,\mu\mathrm{m}$ and $n^* = 0.0125$ part (b).

CHAPTER 7

EXPERIMENTS ON 2DLG SAMPLES IN THE NONEQUILIBRIUM REGIME

In this chapter, experimental results regarding nonequilibrium phenomena at low magnetic fields performed on plain 2DEG and 2DLG samples are presented. A brief explanation of each discussed phenomenon can be found in Section 3.4 For further reading, one can refer to [17].

All presented low magnetic field effects share a periodicity of $1/B$, where the oscillation period depends on the energy of the exciting particle, requiring a magnetic field range where the LLs still overlap in such a way that transitions along several LLs are allowed by selection rules. [17]

The most prominent example of microwave induced resistance oscillations (MIRO) [114, 116, 120] and their far-infrared version (FIRO)[124, 125] are caused by resonant photon-absorption, accompanied by a transfer into a higher LL. These are also possible at higher orders, where multiple photons contribute to the electronic transition. [121, 126]

The other two types of $1/B$ -periodic oscillations at high filling factors are not caused by electromagnetic radiation: the first is Hall field induced magnetoresistance oscillations (HIRO) [112, 149], which occur because of a large Hall electric field that tilts the LLs. Therefore, the cyclotron diameter fits the transverse, isoenergetic distance between LLs.

The second type is phonon-induced resistance oscillations (PIRO) [113, 123, 130, 134, 136, 137, 150], which are the main focus of this chapter. PIRO are caused by electrons selectively absorbing energy from acoustic phonons of the right frequency to enable transitions between LLs. [17] The results presented in this chapter were also published in [151].

7.1 Microwave-induced resistance oscillations

MIRO are a highly investigated phenomenon of $1/B$ induced resistance oscillations in 2DEG samples. These oscillations occur in a 2DEG sample if it is subjected to magnetic fields (in the range of a few 100 mT) and electromagnetic radiation in the range of tens to hundreds of GHz. A detailed description of this phenomenon can be found in Subsection 3.4.1.

To prove the existence of MIRO in our 2DEG heterostructures, a standard MIRO measurement was performed on a 100 µm × 100 µm Hall bar with an electron density of $n_e = 2.5 \cdot 10^{15}\,\mathrm{m}^{-2}$. This measurement was performed at the *Physikalisch-Technische Bundesanstalt, Branschweig* by Lars Freise. The sample was illuminated in continuous wave mode with microwave radiation of 25 and 30 GHz provided by a synthesized sweeper (HP 83650A). Simultaneously, the longitudinal resistance was measured with a standard lock-in technique (17.7 Hz, 500 nA) while the magnetic field was varied between 0 mT and 300 mT. The experiment was performed for different attenuation factors of microwave radiation. To couple the microwave radiation into the 2DEG, a gold bonding wire 1 mm in length was used as an antenna. It was grounded at one end and connected to the synthesized sweeper at the other. The measurement was performed in a dry dilution refrigerator's chamber while the temperature did not exceed 100 mK during the experiment.

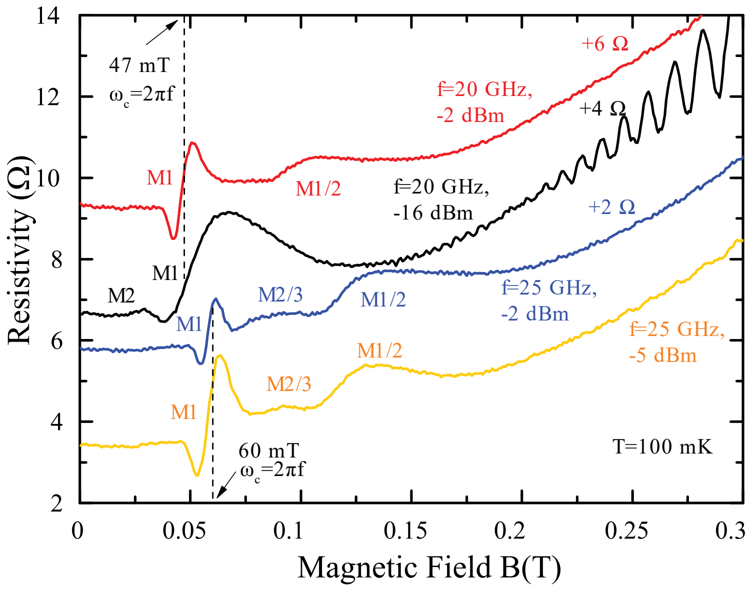

Figure 7.1: MIRO superimposing the magnetoresistivity of the 100 µm × 100 µm Hall bar. At the highest attenuation of −16 dBm, conventional MIRO of the first (M1) and second order (M2) were visible. With increased optical output power, fractional MIRO occurred, marked by the respective resonance (e.g., M1/2), where two microwave photons assist the transition along one LL distance.

Fig. 7.1 presents the measurement results. As marked by the respective value in the diagram, the upper tree traces are vertically offset. At an irradiation frequency of $f = 20\,\mathrm{GHz}$, attenuations of

−2 dBm (red trace) and −16 dBm (black trace) were used. Conventional MIRO [114] are present in the black trace marked with M1 and M2, where the minimum power is used. M1 occurs at the cyclotron resonance, which is marked by the vertical dotted line. M2 denotes the resonance at which the LL spacing corresponds to half the cyclotron frequency, such that the photon energy is twice the LL spacing. An electron is lifted along two LL distances by absorbing one photon.

All other traces exhibit fractional MIRO [126] because of the high microwave intensity. The cyclotron resonance of the red trace (20 GHz, −2 dBm) occurs as for the attenuation of −16 dBm and $f = 20\,\mathrm{GHz}$ at $B = 47\,\mathrm{mT}$. The fractional MIRO M1/2 is positioned at twice the magnetic field ($B = 94\,\mathrm{mT}$). Here, two photons assist the transition of an electron along one LL.

For the measurements performed at a frequency of 25 GHz (blue trace, measured with an attenuation of −2 dBm and orange trace, measured at an attenuation of −5 dBm), the cyclotron resonance shifts to a magnetic field of 60 mT. For both attenuation factors, the M2/3 and the M1/2 fractional MIRO resonances are visible, where the magnetoresistivity oscillations of the less attenuated trace (−5 dBm) is more pronounced. The MIRO marked with M2/3 corresponds to the magnetic field at which it is possible that three photons together possess twice the energy difference between the LLs (i.e., $3hf = 2\hbar\omega_c$). [126]

In sum, the used heterostructures indeed show MIRO, which is also proof of the high mobility because these oscillations are only observed in high-mobility samples. [17]

7.2 Hall-induced resistance oscillations in dilute 2DLG

As detailed in Chapter 6, two samples with Hall bar widths of $w = 20\,\mu\mathrm{m}$ and $w = 100\,\mu\mathrm{m}$, each exhibiting four 2DLGs with obstacle densities between $n^* = 0.0031$ and $n^* = 0.025$ and a naked reference field, were prepared. As the HIRO-extrema positions depend on the Hall bar width (see Subsection 3.4.2), the first HIRO maximum is expected to shift to magnetic fields five times larger for the narrower Hall bar. For both samples, circular LG obstacles with a radius of 1 µmare chosen.

The same experiment was conducted on a meander-shaped Hall bar with a width of $w = 50\,\mu\mathrm{m}$ and length of 22 mm. This sample consisted of a plain 2DEG structure with no additional patterning.

The HIRO measurements were conducted using the following well-established method [112]: an AC-current of 500 nA, $f = 17.7\,\mathrm{Hz}$ was applied along the source-drain direction and the longitudinal voltage drop along the respective structure of interest was recorded with a lock-in technique. Additionally, a DC-current I_{DC} was applied along the source-drain direction such that the voltage drop corresponded to a differential measurement signal v_{ac}. The differential resistance was $r_{xx} = (\delta V/\delta I)_{I_{DC}} = v_{ac}/i_{dc}$.

Fig. 7.2 (a) depicts the differential resistance for source drain currents between 1 µA and 50 µA. The first four HIRO-maxima for the 50 µA trace are marked by integers. Comparing the position of the first maximum for the 50 µA and 30 µA trace, one observes a shift to lower magnetic fields. This shift is linear as proven by part (b) of Fig. 7.2, which represents the magnetic field position of the minimum or maximum of the respective period j against the applied source-drain current. As proposed by the HIRO theory detailed in Subsection 3.4.2, the data follow

$$I_{SD} = j\frac{\hbar B n_e e^2 w}{2m^{*2} v_F} \tag{7.2.0.1}$$

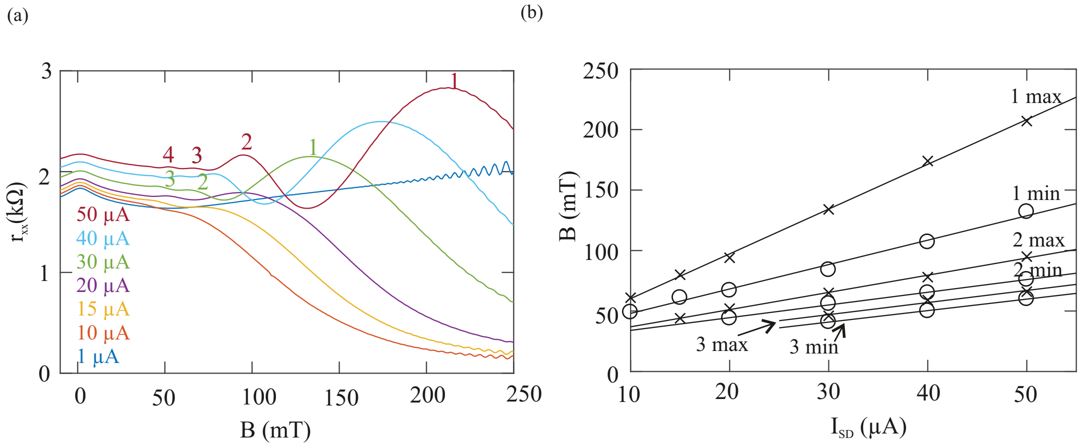

Figure 7.2: (a) Differential magnetoresistance traces for different source-drain currents between 1 µA and 50 µA. (b) I_{SD} vs. the magnetic field position of occurrence. The positions of the extrema shift linearly with the used source-drain current for each maximum and minimum.

From the slopes of the linear fits in Fig. 7.2 (e.g., $2.69 \cdot 10^{-4}$A/T for the trace of the first maximum), one is able to determine the Hall bar width with the other known parameters to be 49.9 µm, which is in excellent agreement with the lithographic design of the Hall bar width of 50 µm.

As the source-drain current is increased, the HIRO do not directly develop. Before their first occurrence at 15 µA, the additional source-drain current causes a negative magnetoresistance. This can be seen when the trace with no additional dc-current admixture is compared with the 10 µA trace. The almost linear magnetoresistance in the interval of 50 mT to 200 mT changes to a bell-shaped trace resembling GNMR (discussed in Subsection 3.2.6). This phenomenon was measured by another group before [152] and explained by a nonohmic conductivity correction undergoing a sign reversal to negative magnetoresistance caused by electron heating. The increase of the zero-field differential resistance is also a sign for electron heating (the traces are not vertically offset).

Starting from the experimentally and theoretically well-described phenomenon of HIRO, the question arises of whether HIRO is observable in 2DLG samples. Compared with the plain 2DEG sample, the LG-obstacles reduce the path an electron is able to move freely along. Here the question of interest is, if the condition for the HIRO-mechanism is possible, whether the electron needs to move in a nonscattered manner from the Hall bar edge to the opposite one.

The experimental results of the 100 μm × 100 μm measurements fields are presented in Fig. 7.3.

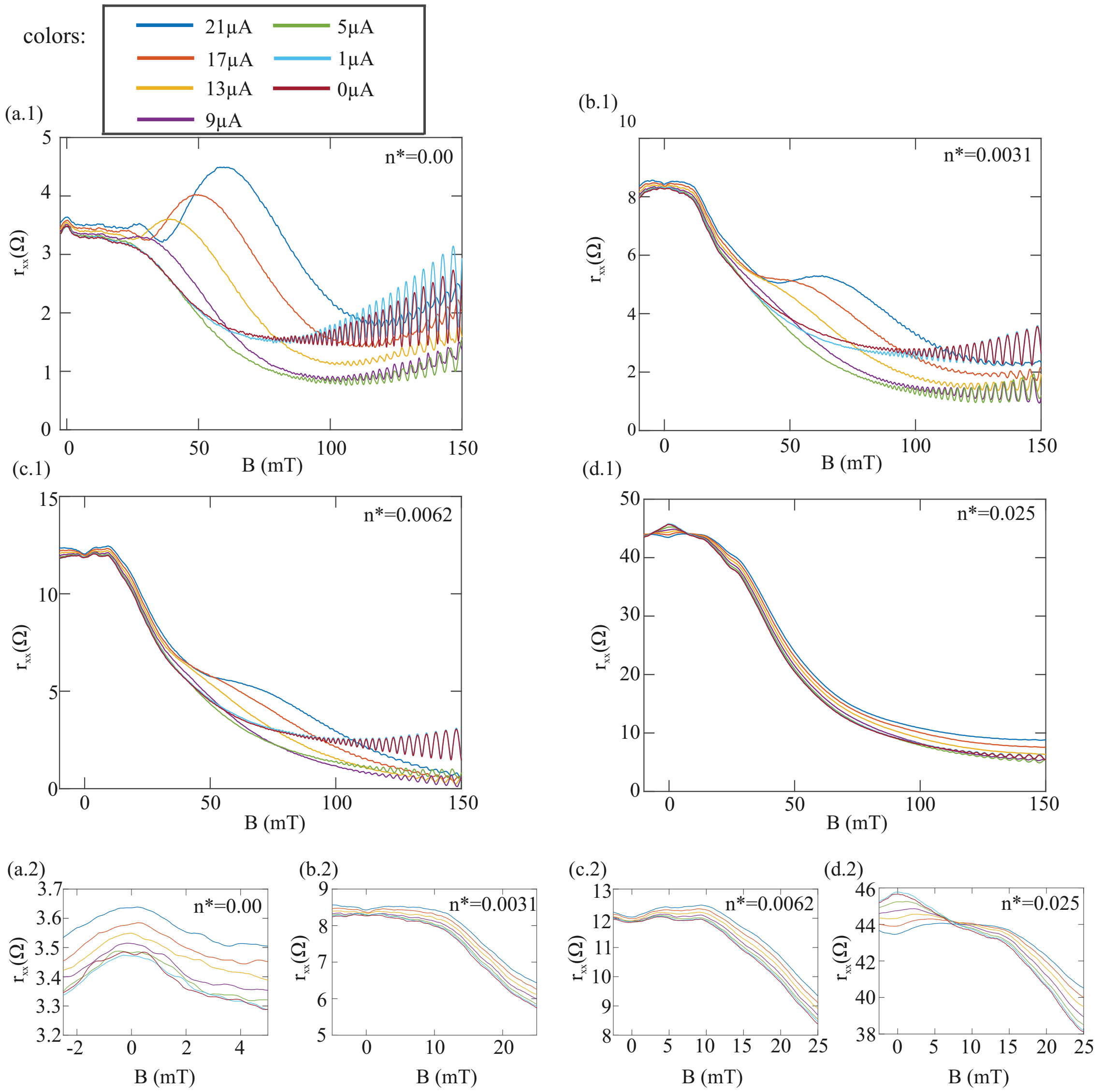

Figure 7.3: (a.1) - (d.1) Differential magnetoresistivity of the 100 μm × 100 μm Hall bar for the pristine sample (a.1 and a.2), and the dilute 2DLG (b-c). Each color corresponds to a certain source drain current. As the 2DLG density is increased, the interval in which HIRO occur reduces systematically from lower magnetic fields. The lower panel (a.2-d.2) presents zoom-ins of the respective measurement.

Five measurement fields, the first with no 2DLG and the following four with increasing obstacle densities from $n^* = 3.1 \cdot 10^{-3}$ to $n^* = 25 \cdot 10^{-3}$, are patterned on the sample. The measurement field of the plain 2DEG exhibits the well-known HIRO characteristics (see part (a.1) of Fig. 7.3). Moreover, the GNMR, which is already visible in the trace with no additional source-drain current, becomes more pronounced for $I_{SD} = 5\,\mu\text{A}$, followed by the formation of HIRO first observed with $I_{SD} = 9\,\mu\text{A}$.

As the obstacle density increases to $n^* = 3.1 \cdot 10^{-3}$, only the first HIRO oscillation is observable. The interval in which the HIRO effect is visible is reduced from the low B-field side by the negative magnetoresistance of the 2DLG, and therefore it starts from approximately 32 mT. This magnetic field is slightly higher than that of percolation, which follows Mirlin et al. [35] $B_c = 22.6\,\mathrm{mT}$ for this density. The upper boundary is caused by the onset of SdHo at approximately 100 mT. The position of the first maximum is slightly shifted (from 59 mT to 66.1 mT) although the same $I_{SD} = 21\,\mu\mathrm{A}$ current is applied.

Both observations are consistent with the other 2DLG, which exhibit higher obstacle densities.

The magnetic field at which the HIRO set in for $n^* = 6.2 \cdot 10^{-3}$ is 35.9 mT. The position of the first maximum for this density is for the $I_{SD} = 21\,\mu\mathrm{A}$ trace at 72.2 mT.

One possible explanation for the shift of the HIRO position to higher magnetic fields as the obstacle density is increased might be that the channel width of the 2DEG is effectively reduced by the area covered with obstacles, considering that all other parameters such as electron density n_e and the lithographic channel width are not changed. The paths in the y-direction along which an electron is able to drift are disturbed by the obstacle's hard potential walls.

Comparing these measurements to the temperature- dependent measurements on these samples in Section 6.4 and the measurements regarding the influence of an in-plane magnetic field in Section 6.3 it seems like HIRO are only possible in the same magnetic field interval in which the GNMR is present.

At an obstacle density of $n^* = 0.025$, no HIROs are observable. The variations between the measurement traces are caused by the increased electron temperature induced by the large source-drain currents, as proven by the reduced amplitude of the SdHo observable in the interval of 100 mT – 150 mT.

The lower line of Fig. 7.3 depicts zoom-ins of all 2DLGs at low magnetic fields. Comparing part (a.2), which shows the results of the nonpatterned measurement field with part (d.2), a qualitatively different behavior is observed. While the measurement traces shift upwards for $n^* = 0$, the small peak around ±5 mT of the $n^* = 0.025$ field evolves to a dip as the source-drain current is increased. One possible explanation is that the density of $n^* = 0.025$ is sufficiently high for the effect of retroreflective corridors, which are broken by the thermal smearing caused by the increased electron temperature (see Chapter 5). The magnetoresistance in the regime of the corridor effect was detailed by Schulck et al. in [141]. The peak of the $n^* = 0$ reference field is caused by contributions of a Lorentz gas formed by oval defects and boundary scattering, as detailed in Chapter 6.

The sample with a Hall bar width of $w = 20\,\mu\mathrm{m}$ was patterned with the same obstacle densities as the sample with $w = 100\,\mu\mathrm{m}$. Measurement results of the HIRO evolution are presented in Fig. 7.4. Comparing the reference field (part (a.1)) to the plain field of the $w = 100\,\mu\mathrm{m}$-wide sample conveys two major differences: the GNMR is more pronounced by means of a wider peak (approx. ±150 mT), and at low magnetic fields (±10 mT) a double peak structure is observed (see the zoom-in in part (a.2)). As discussed in Chapter 6, this double peak structure can be attributed to the ballistic effect of boundary scattering.

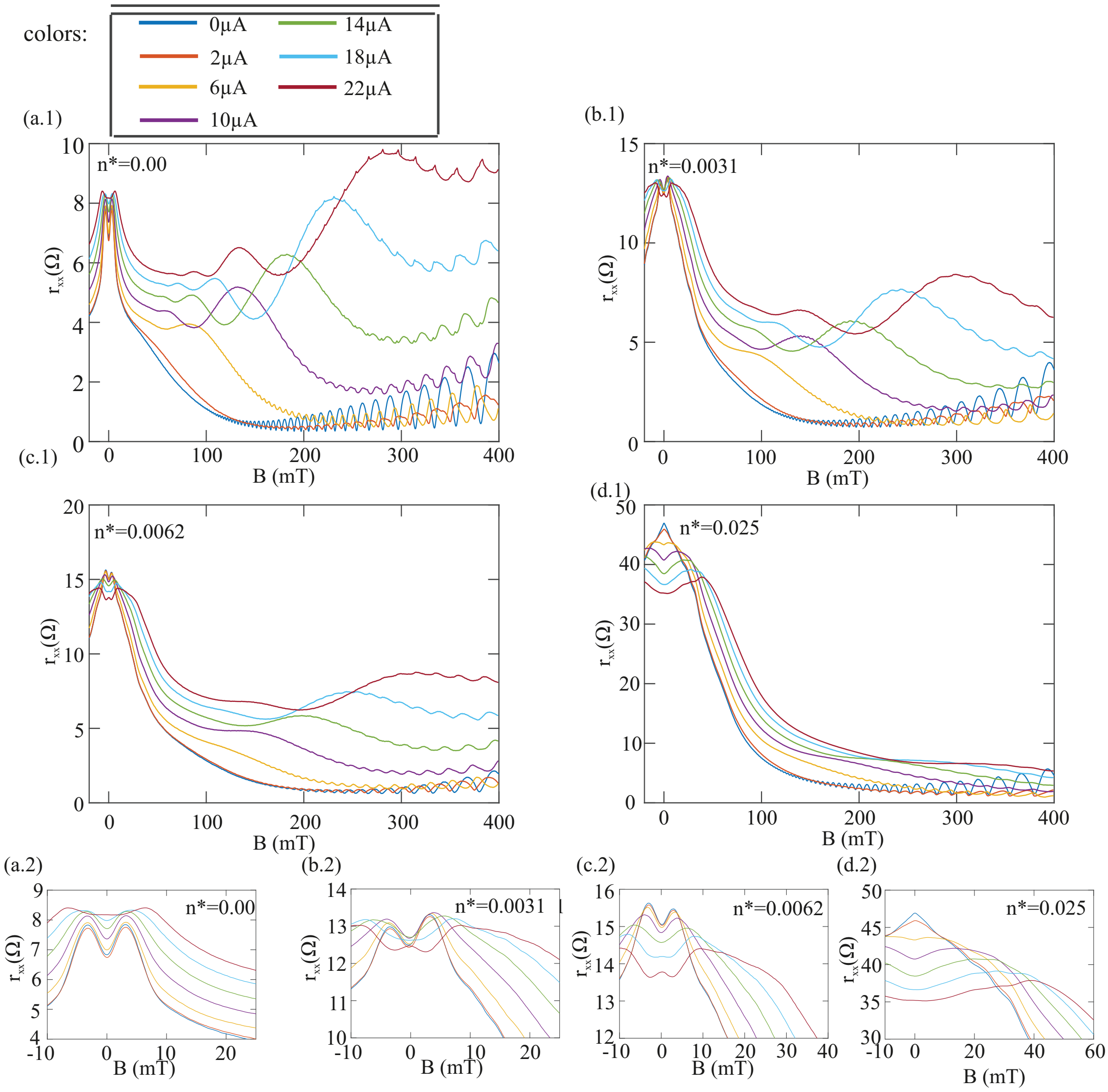

Figure 7.4: (a.1) - (d.1) Differential magnetoresistivity of the 20µm × 100µm Hall bar fields. Part (a. 1) depicts the data from the unpatterned 2DEG field, showing a highly pronounced wire peak occurring from boundary scattering at the sample edges. With increasing n^* the HIRO are less pronounced, as can be seen in parts (b.1)-(d.1). The lower panel shows zoom-ins of the four measurement fields at low magnetic fields.

For $I_{SD} = 22\,\mu\text{A}$, the first HIRO maximum occurs at 284 mT, which scales as expected with a factor of 5 compared with the first HIRO maximum of the $w = 100\,\mu\text{m}$-wide sample. As the position of the respective HIRO-period shifts toward larger magnetic fields, the interval in which HIRO are observable increases and more periods (at least five for the $I_{SD} = 22\,\mu\text{A}$ of the $n^* = 0$ sample) are measurable. As for the $w = 100\,\mu\text{m}$-wide sample, the lower boundary of the magnetic field interval in which HIRO occur is shifted toward higher magnetic fields as the obstacle density n^* is increased. For

$n^* = 6.2 \cdot 10^{-3}$, three oscillations are still observable, whereas for $n^* = 0.025$, only the first maximum is resolved. The maxima positions shift from 284 mT to 335.5 mT as n^* is increased from $n^* = 0$ to $n^* = 0.025$. The increased source-drain current leads to electron heating as proven by the reduced SdHo amplitude in each measurement. The evolution at low magnetic fields is presented in the zoom-ins ((a.2)-(d.2) in Fig. 7.4).

HIRO can occur in the magnetoresistance of 2DLG, but only in a magnetic field interval above the percolation threshold and below the onset of SdHo. In the 2DLG-dominated magnetic field interval (i.e., approximately below the percolation threshold B_c), an increased source-drain current induces temperature effects rather than HIRO contributions. Moreover, a shift of the respective HIRO amplitudes is observed as the obstacle density is increased. This could be attributed to an effectively narrower Hall bar width, offering less space for the drift motion along the direction perpendicular to the source-drain direction, which is caused by the depleted areas of LG obstacles.

7.3 Phonon-induced resistance oscillations

As detailed in Subsection 3.4.3, PIRO are another class of $1/B$-periodic magnetoresistance oscillations. The following two subsections discuss how PIRO are observed once the acoustic phonon branches of GaAs are populated through increasing the bath temperature. Additionally, it is possible to induce PIRO by irradiating the sample with THz-photons. Here, the excitation of the acoustic phonon branch is caused by an indirect effect since the energy of the participating phonon (deduced from the $1/B$-period) does not match the photons' excitation energy. The effect of PIRO generation by THz-irradiation dominates any direct photon-induced effects such as MIRO, although at gigahertz frequencies the samples exhibit the well-established MIRO phenomena (compare Section 7.1).

7.3.1 PIRO induced by 1.8 THz-irradiation

7.3.1.1 Measurement setup and THz-QCL characteristics

The same experiment was conducted on three different samples to compare the influence of electron density. The first sample has an electron mobility of $239\,\mathrm{m^2V^{-1}s^{-1}}$ and an electron density of $n_e = 4.0 \times 10^{15}\,\mathrm{m^{-2}}$, and the 2DEG has a depth of 75 nm. The Hall bar is meander-shaped with 16 turns over a length of 22 mm and a stripe width of 50 µm. The other two samples host a 2DEG 150 nm below the surface, providing a mobility of $307\,\mathrm{m^2V^{-1}s^{-1}}$ (with $n_e = 2.5 \times 10^{15}\,\mathrm{m^{-2}}$) and $523\,\mathrm{m^2V^{-1}s^{-1}}$ (with $n_e = 2.6 \times 10^{15}\,\mathrm{m^{-2}}$) after illumination. These two samples have the shape of a Hall bar with a width of 100 µm and a distance of 100 µm between the voltage probes.

The experiments, which exposed the samples to THz-radiation, were performed in a liquid gas flow cryostat to enable the minimum temperature of 1.4 K to be reached and the cooling power to be sufficient to cool the THz-quantum cascade laser (QCL). [153, 154] The THz-QCL was placed in the sample holder, 20 cm above the sample. This not only prevented heating of the 2DEG but also that the THz-QCL was not exposed to the magnetic field of the superconducting solenoid. A polished brass tube (inner diameter 7 mm) was used as a wave guide to transfer the THz radiation to the sample surface.

The THz-QCL, which was purchased from Alpes Lasers SA, has a multi-mode emission spectrum centered at 1.8 THz with a range from 1.6 THz to 2.0 THz in continuous operation mode, depending on the QCL current [155], as depicted in Fig. 7.5.

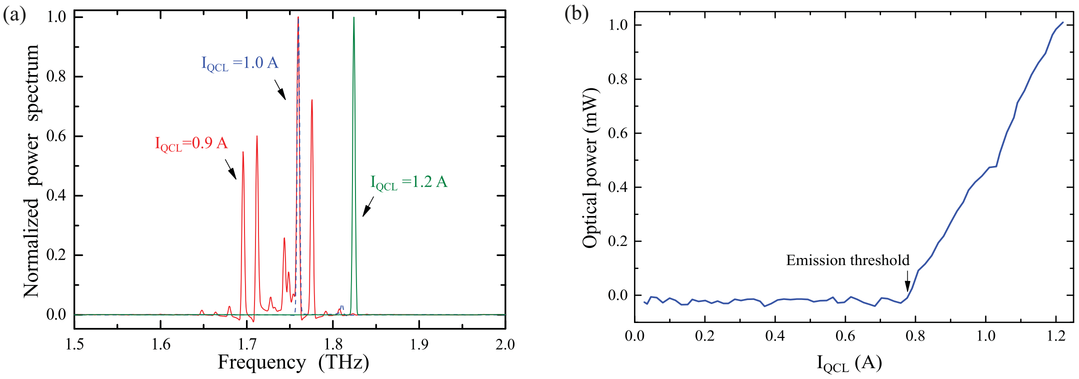

Figure 7.5: (a) Emission spectra of the THz-QCL in continuous mode for three different currents. The 1.0 A and 1.2 A traces are single peaks at 1.76 THz and 1.82 THz, whereas the trace at 0.9 A is a multi-mode spectrum between 1.68 THz and 1.75 THz. (b) Optical power plotted against the current through the THz-QCL. The optical power increases almost linearly as I_{QCL} increases with a threshold current at 0.78 A. Data from [155].

Through the variation of the current through the laser I_{QCL}, the emission profile was expected to change. The THz-QCL was used in pulsed mode at a frequency of 17.7 Hz and a duty cycle of 20 %. One purpose of this operating mode is to keep the cryostat temperature at 1.4 K. Moreover, pulsing the THz-QCL allowed for referencing the longitudinal voltage drop of the sample to the rising edge of the laser pulse. The measurement setup was as follows:

A DC source-drain current in the range of 100 nA – 5 µA was applied to the sample and the longitudinal voltage drop in the current direction was measured using a lock-in amplifier (referenced to the QCL driving frequency), as well as a DC-voltmeter simultaneously. The photoresistivity was determined from the Fourier transform of the rectangular signal. The magnetic field was varied during the measurements. The 2DEG in all experiments was positioned perpendicular to the magnetic field direction and wave guide, which is also known as Faraday geometry. [156]

Variation of I_{QCL} leads to a change in the optical output power. As shown in Fig. 7.5 (b), it had an almost linear I_{QCL} vs. optical power characteristic with a threshold current of 0.78 A. At 1.1 A the THz-QCL produced an optical power output of 0.8 mW.

7.3.1.2 Cyclotron resonance and bolometric heating

Fig. 7.6 presents the photoresistivity (blue trace) and resistivity (black trace) responses of the meander-shaped sample. The photoresistivity is the photo-voltage divided by the DC source-drain current (here 1 µA). The effect of the cyclotron resonance is visible at magnetic fields between 3.5 T and 5 T. In this interval, the photoresistivity has several pronounced maxima, whereas the magnetoresistivity shows an additional modulation.

The physical mechanism of the cyclotron resonance is a direct absorption of the irradiated photon by the 2DEG. This absorbed energy leads to the excitation of an electron from the uppermost filled LL to the lowermost unfilled one. This direct transition is accompanied by an increase in photoresistivity because of the increased number of charge carriers. As the LL distance is linear to the applied magnetic field, the position of the cyclotron resonances B_c provide information about the QCL emission frequencies f as they can be calculated with

$$f = 2\pi \cdot \frac{eB_c}{m^*} \tag{7.3.1.1}$$

The blue trace in Fig. 7.6 is the photoresistivity of the meander-shaped sample as the magnetic field is varied while $I_{\mathrm{QCL}} = 1.1\,\mathrm{A}$. Three overlapping peaks are observed at 3.87 T, 4.11 T, and 4.57 T, which are caused by the cyclotron resonances [157] of different THz-QCL modes. These correspond to laser frequencies of 1.61 THz, 1.72 THz, and 1.91 THz, respectively [155].

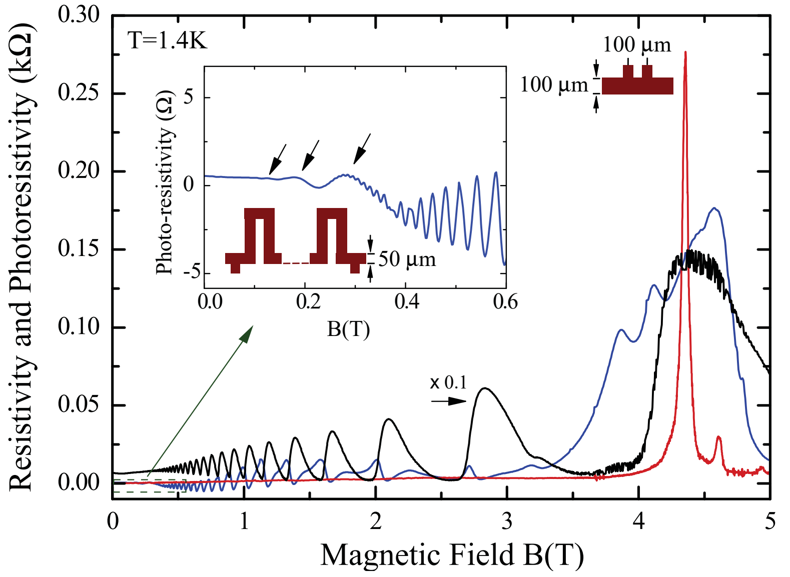

Figure 7.6: Photoresistivity of the meander-shaped Hall bar (blue trace) and of the 100µm × 100µm Hall bar (red-trace). The black trace is the DC-resistivity of the meander-shaped sample under THz-irradiation measured at the same time as the blue trace. The photoresistivity at low magnetic fields is shown in the zoom-in. Here, oscillations marked by arrows of larger periods than the SdHo occur, which are induced by THz-radiation. Figure from [151].

The peak of the cyclotron resonance can be narrowed using a bandpass filter. [158] The red trace was measured while the filter was situated between the THz-QCL and the $100\,\mu\text{m} \times 100\,\mu\text{m}$ sample ($n_e = 2.6 \times 10^{15}\,\text{m}^{-2}$). Therefore, the THz-emission was narrowed to a window with a center frequency of 2 THz and an FWHM of 0.4 THz. Because of the filter, the THz radiation was attenuated by 15 % at the center frequency, showing a cyclotron resonance at 4.45 T (1.82 THz).

The amplitude of the cyclotron resonance is strongly affected by the position of the Fermi level with respect to the LLs. The maximum sensitivity occurs for the Fermi level positioned between two LLs. [159, 160]

In addition to the cyclotron resonance occurring at distinct magnetic field values, the photoresistivity of the meander-shaped sample shows bolometric heating. [124, 161–163] The radiation heats the electron gas through the absorption of photons, which is a nonresonant effect and occurs at any magnetic field, independent of the radiation frequency. This increases the electron velocity and results in thermal smearing of the SdHo. The photoresistivity, on the other hand, reveals an oscillatory part with the same period as the SdHo. At minima positions of the SdHo, the photoresistivity is maximized and vice versa.

The inset of Fig. 7.6 shows the photoresistivity trace at low magnetic fields in the range of 0 to 0.6 T. Here, another oscillation occurs with a larger period compared with the SdHo. The oscillation maxima, which are two orders of magnitude smaller than the cyclotron resonance, are marked by arrows. These oscillations are PIRO and the main focus of the following subsection.

7.3.1.3 Characterization and analysis of the PIRO

To characterize the oscillations occurring at low magnetic fields, the optical output power of the THz-QCL is varied by changing I_{QCL}. These two parameters are almost linearly connected to each other, as detailed above.

Fig. 7.7 depicts the photoresistivity as a function of B of the $100\,\mu\text{m} \times 100\,\mu\text{m}$ Hall bar ($n_e = 2.6 \cdot 10^{15}\text{m}^{-2}$) for low magnetic fields under THz-irradiation at different optical powers. As the THz-intensity is at its maximum, the oscillations (indicated by arrows) are highly pronounced (red trace, $I_{\text{QCL}} = 1.1\,\text{A}$). Their amplitude reduces monotonously as the optical output power is reduced. Below the lasing threshold at $I_{\text{QCL}} = 0.75\,\text{A}$, the PIRO as well as any sign of bolometric heating are absent. This indicates that the oscillations are produced by THz radiation. Moreover, the positions at which minima and maxima occur do not depend on the laser power.

Comparing the different emission profiles from Fig. 7.5 (a) with the photoresistivity at different I_{QCL}, it becomes clear that the exact emission frequency profile (which varies by ±10 %) does not change the resonance positions.

These observations were found for all samples under investigation, with and without the use of the bandpass filter.

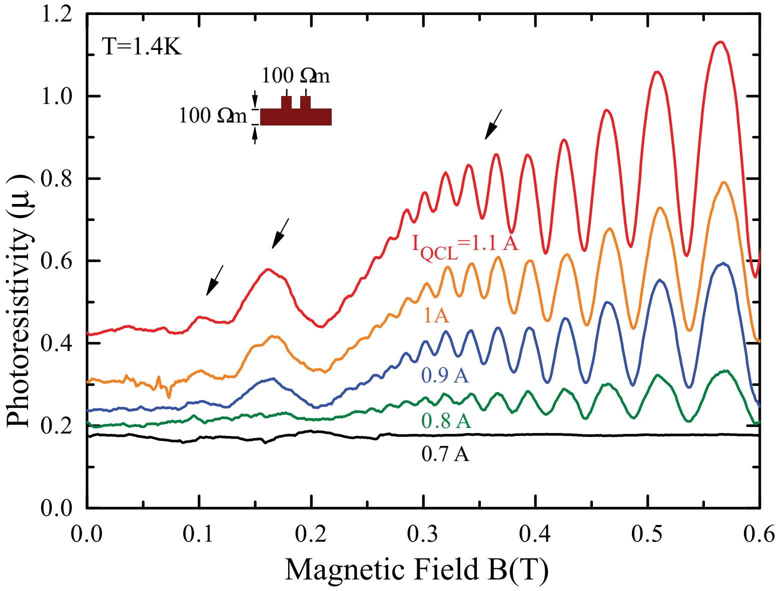

Figure 7.7: Photoresistivity in the magnetic field interval from 0 to 600 mT for the 100 µm × 100 µm Hall bar under THz-irradiation. The different traces correspond to measurements with different I_{QCL} applied through the THz-QCL. As I_{QCL} is below the lasing threshold, no PIRO or bolometric heating is recorded. As the optical power scales linearly with I_{QCL}, a monotonous increase of the amplitudes is observed, proving that their positions do not depend on the exact emission frequency profile. The emission profile is slightly changed by the variation of I_{QCL}. Figure from [151].

In the following paragraphs, these oscillations are proven to be PIRO by analyzing them along the lines of the PIRO phenomenology detailed in [113, 123]:
Only those phonons from the phonon dispersions that have the frequency

$$\omega_{\text{p}} = 2k_{\text{F}}s \tag{7.3.1.2}$$

can be resonantly absorbed by the 2DEG [113]. This selection rule is a consequence of the momentum conservation of this effect. k_{F} is the Fermi wave number, and s is the sound velocity in GaAs. The absorption of energy by electrons is accompanied by transitions between LLs. At the magnetic fields at which PIRO occur, the LLs still overlap, also proven by the not completely evolved SdHo.
As the physical mechanism of PIRO was detailed in Subsection 3.4.3, PIRO occur with a periodicity ϵ given by the ratio of the phonon frequency ω_{p} and the cyclotron frequency ω_{c}:

$$\epsilon = \frac{\omega_{\text{p}}}{\omega_{\text{c}}} = 2s\sqrt{2n_{\text{e}}\pi} \cdot \frac{m^*}{e}\frac{1}{B} \tag{7.3.1.3}$$

In eq. 7.3.1.3, m^* is the effective mass of the electrons, n_{e} is the electron density, and e is the elementary charge.
The inset of Fig. 7.8 is a representation of the PIRO against the inverse magnetic field. In this representation the maxima positions are equidistantly spaced, proving their $1/B$ periodicity. This is valid for all three samples under investigation.

The analysis of the oscillation in accordance with Hatke et al. [123] (detailed in Subsection 3.4.3) proves them to be PIRO:

The right axis of the inset counts the respective maximum number (filled markers) by attributing it to an integer number n.. The minima are counted with half integers (open circles). The red line is a linear fit of these points, of which the slope is proportional to the sound velocity s. The intercept of this line is the phase δ, which is a measure of how much the maxima positions ϵ differ from an integer value n.

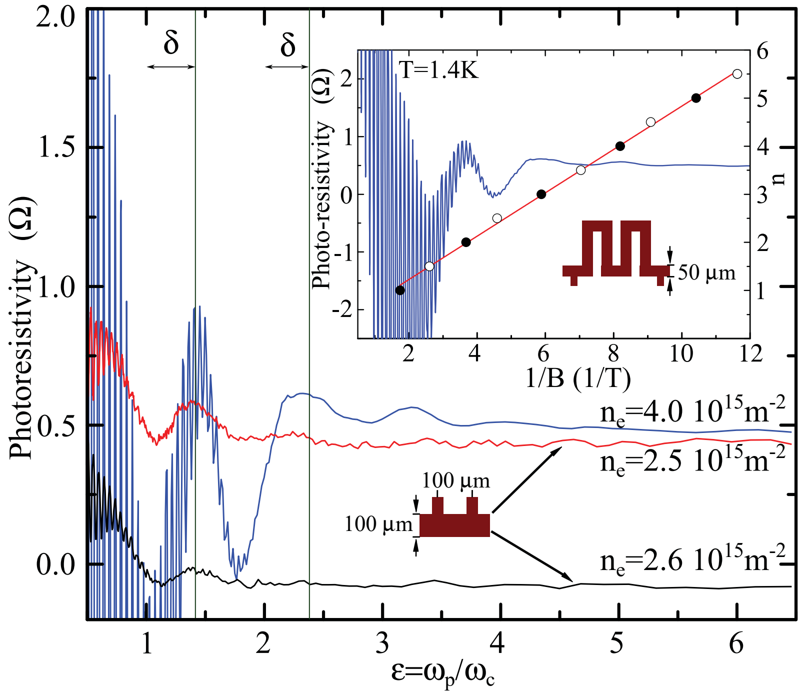

Figure 7.8: Inset: Photoresistivity of the meander-shaped sample vs. $1/B$. The red line is a linear fit of the integer number dedicated to the respective oscillation maximum vs. $1/B$. From this slope the sound velocity s can be determined. Main figure: The photoresistivity data of the three samples are represented against ϵ conveying that the extremal points fall on the same positions (note the differences in electron density n_e). Figure from [151].

For the meander-shaped sample, this analysis gives a value of $s = 3.7\,\mathrm{km/s}$. The sound velocity for the $100\,\mu\mathrm{m} \times 100\,\mu\mathrm{m}$ samples are $s = 2.6\,\mathrm{km/s}$ ($n_e = 2.5 \cdot 10^{15}\mathrm{m}^{-2}$) and $s = 2.4\,\mathrm{km/s}$ ($n_e = 2.6 \cdot 10^{15}\mathrm{m}^{-2}$). These values are in good agreement with values in the literature, which are in the range of 2–5 km/s. [113, 130, 131, 150, 164]

For the calculation of s, the value for the electron mass m^* was assumed to be $0.067\,m_0$; however, the literature shows that under irradiation the values for m^* range from $0.058\,m_0$ to $0.067\,m_0$. [87] To be certain of calculating s with the correct value of m^*, a MIRO measurement of the plain 2DEG $100\,\mu\mathrm{m} \times 100\,\mu\mathrm{m}$ sample was taken to determine m^* from the position of the MIRO maxima (see Fig. 7.1). From this, m^* was determined to be $m^* = 0.066$, which is within the experimental error and the same value as the 0.067 m_0 in darkness in the literature.

The difference in the sound velocity for the meander-shaped Hall bar compared with the other two samples can be explained by the 90°-turns of the conduction channel. The electron transport in two directions enables interactions with multiple phonon branches, leading to an effective average sound velocity. [54] This is absent for the 100 µm × 100 µm square-shaped Hall bars.

In the main part of Fig. 7.8, the photoresistivity is represented against ϵ. This means that each trace is scaled with the product $s\sqrt{n_e}$ such that the maxima and minima of the different samples fall on the same positions. This results in a linear representation of the extrema number as a function of $1/B$. The difference of the extremal points to an integer or half integer value is the extracted phase δ.

As a result it can be stated that the observed THz-induced magneto oscillations are fully compatible with PIRO.

The photoresistivity in the interval between 0 and 5 T (see Fig. 7.6) does not show any signature of MIRO or FIRO. [124, 125] From the literature, it is known that their amplitudes are suppressed as the frequency of the radiation is increased toward the THz regime, caused by the separation of LLs at higher magnetic fields. [116] As discussed in Section 7.1, the used 2DEG samples exhibited MIRO under irradiation of 20 GHz and 25 GHz (see Fig. 7.1).

In summary, no PIRO signature was detected in the MIRO experiment at GHz-frequencies (compare Fig. 7.1). Furthermore, no MIRO were observed in the PIRO experiments as the sample was exposed to THz-irradiation. Additionally, it was found that the PIRO extremum points do not change the magnetic field position at which they occur as the THz-QCL emission frequency is changed by the variation of I_{QCL}. This is in direct contrast to the idea of direct photon absorption.

To explain the PIRO occurring under these experimental conditions, a population of the acoustic phonon branches is first required. The temperature under THz-irradiation is therefore estimated from the amplitudes of the SdHo (trace 3 in Fig. 7.6) using Ando's formula [165]. From this, the electron temperature is estimated to be 3.3 K, which is higher than the bath temperature of 1.4 K of the sample chamber. Thus, the increased electron temperature is expected to lead to an equilibration with the lattice temperature.

Two mechanisms could populate the acoustic phonon branch through an indirect mechanism: Brillouin scattering and a three-step mechanism involving the absorption of THz-photons by the 2DEG, followed by electron–phonon coupling.

Brillouin scattering is a well- known mechanism for measuring the sound velocity. [166–168] Light in the visible and infrared regime scatters elastically at crystal atoms, enabling the sound velocity to be deduced from spectroscopic information. Photons with THz-frequencies may also contribute to this. Once acoustic phonons are present, the PIRO mechanism described above is possible. Inelastic scattering of THz-photons at lattice imperfections can lead to a population of the acoustic phonon branch. [169]

The second imaginable scenario is a three-step process. Initially the THz radiation is absorbed by the 2DEG. It is known (first step) that radiation is absorbed by the 2DEG at magnetic fields not in resonance with the frequency of the irradiating photon. [124] This heats the electron gas, which also causes the signatures of bolometric heating in the photoresistivity traces and smears the SdHo in the magnetoresistivity trace. As a next step, the absorbed energy transfers to phonons through electron–phonon coupling. [170–174] Just phonons of the acoustic phonon branch are excited because the energies of the optical branches are above 30 meV and the THz-photons have an energy of 7.4 meV. [131, 162, 175] The third step of this process is the conventional PIRO mechanism of the 2DEG resonantly absorbing only these acoustic phonons, which have a frequency of $\omega_p = 2k_F s$, whereby electrons are scattered into energetically higher or lower LLs leading to oscillations in the magnetoresistance [113]. Notably, within the PIRO mechanism, only the component of the phonon momentum vector contributes in plane of the 2DEG. This is also the predominant direction of phonon emission (second step).

To conclude, PIRO were found to generate in a 2DEG by exposing the sample to THz-irradiation at 1.8 THz. This effect occurs in samples that show conventional MIRO when irradiated with much lower frequencies. In the THz regime, the effect of PIRO dominates the MIRO effect because the photoresistivity does not show a signature of MIRO, and vice versa, no PIRO are observed when the sample is irradiated with radiation in the GHz regime. Two mechanisms that cause PIRO are suggested: Brillouin scattering and the classical heating of the 2DEG followed by thermalization of the lattice through the excitation of acoustic phonons. It might be that both processes contribute to the acoustic phonon population. For a further detailed characterization and enhanced understanding, improved control of the THz source is desirable with regard to spectral resolution and polarization. Whether the bulk or interface phonons are involved remains to be clarified. Moreover, the values for the coupling constants and transition rates of the contributing processes that depend on the frequency could be characterized in future studies.

7.3.2 PIRO induced by thermal excitation

To compare the observed PIRO under THz irradiation with the well-established process of PIRO caused by increased bath temperature, the usual PIRO measurement was performed on the meander-shaped Hall bar and on the 100 µm × 100 µm sample. Therefore, the sample chamber's temperature was increased to 20 K, which caused the population of the acoustic phonon branches by heating the crystal lattice. The magnetoresistivity was recorded using the standard lock-in technique (detailed in Section 2.2) at a reference frequency of 17.7 Hz, while the source-drain current was set to 1 µA. To qualify the oscillation extremum points more accurately, the background (i.e., the floating average with 100 data points) of the magnetoresistance trace was subtracted from the original magnetoresistivity trace. Fig. 7.9 shows the PIRO oscillations after this data processing. Here, the PIRO amplitude is maximized in a temperature interval between 4.5 K and 8 K. Above 8 K, the amplitude reduces and is absent at 20 K. At the lowest temperature of 1.4 K, no PIRO are recorded. A detailed study of the temperature dependence of PIRO can be found in [134], where it was proven that thePIRO are mostly pronounced at the temperature that energetically corresponds to $k_B T = 2k_F s$.

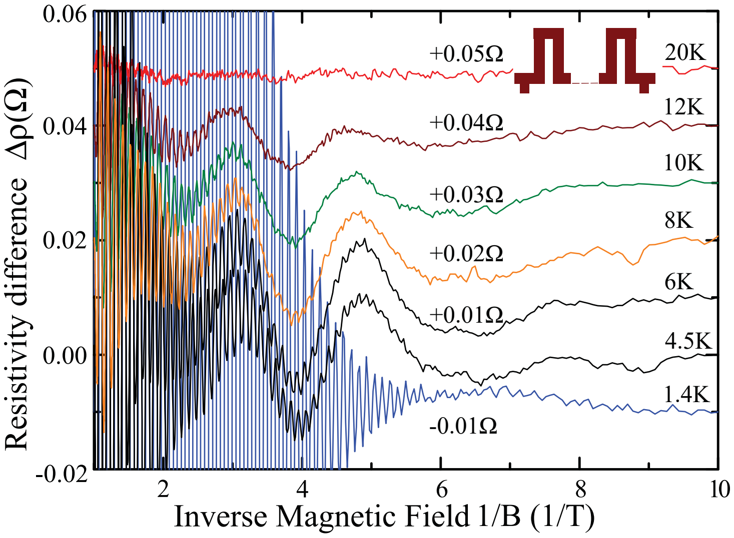

Figure 7.9: Temperature evolution of the oscillating part of the magnetoresistivity of the meander-shaped Hall bar. No PIRO are visible at 1.4 K, whereas they are highly pronounced in the interval from 4.5 K to 12 K and absent at 20 K. Figure from [151].

Following the analysis detailed in Subsection 3.4.3 and performed on the THz-induced PIRO in Subsection 7.3.1, the phonon sound velocity was extracted from the data. This results in a value of $s = 3.65\,\text{km/s}$, which is in excellent agreement with the sound velocity of $s = 3.70\,\text{km/s}$ that was determined from the PIRO data under THz irradiation.

As a resume, it can be stated that GaAs/AlGaAs heterostructures exhibit PIRO as the temperature is increased. It was found experimentally that the excitation mechanism for populating the acoustic phonon branches—either through heating the sample or irradiating it with THz light—does not matter in the occurrence of PIRO in magnetoresistivity.

CHAPTER 8

CONCLUSION AND OUTLOOK

This thesis contributes insights into electron transport within 2DLGs with regard to four major questions. In the following paragraphs, each question is addressed with a short summary along with suggestions for further possible research approaches.

In Chapter 4, the main research question addressed was as follows: *Does anomalous transport exist in retroreflecting 2DLGs, and are signatures of it distinguishable at low magnetic fields?*
Experimentally it was possible to distinguish a local maximum at low magnetic fields, which occurs in the magnetoconductivity of retroreflecting 2DLGs but remains absent for 2DLGs formed by circular obstacles. This was interpreted to be caused by the increasing magnetic field breaking retroreflecting corridors, which is a well-established concept within the classes of memory effects. [24, 141] Simultaneously, weak localization contributions could be excluded. The corridor effect reduced the conductivity but the bending of trajectories increased it. This effect was less temperature-stable than the conductivity maximum caused by guided electron transport along the 2DLG contour due to $\vec{E} \times \vec{B}$-drift. This was found from the temperature evolution of the magnetoconductivities.
Furthermore, from temperature elevation, it was found that the local maximum at low magnetic fields is more pronounced for larger RCs. Equally oriented crosses provide a more temperature-stable and pronounced local maximum.
MD simulations provide valuable insights into the mean squared displacement, the local exponent γ, and the trajectories of tracer particles. It was found from simulations at zero-magnetic field that a diffusion constant cannot be determined from the long time limit of the Einstein relation, which is in agreement with predictions from the EWT. [107] The asymptotic exponent γ linearly decreased for the equally oriented RCs with increasing dimensionless obstacle density n^*, whereas γ for randomly oriented RCs saturated to approximately $\gamma = 0.73$. If small magnetic fields were applied, the diffusion

constant could be determined. From the temporal derivative of the MSD, the trace of the $B = 0$ case was found not to saturate. For finite magnetic fields, the traces fell onto each other until a time τ_B, after which the traces with magnetic fields saturated to a value from which the diffusion constant could be determined. Furthermore, τ_B decreased with B. The decay of the conductivity versus the magnetic field proved a power law dependence of $\sigma \propto B^{\delta}$, showing the same signature of the anomalous transport behavior at $B = 0$ in the simulation data, which was observed in experiments.
Both simulations and experiments showed reasonable agreement, while deviations were caused by the inevitable background scattering from phonons and host crystal impurities.

In Chapter 5, the main research question addressed was as follows:
How do dynamic and static background scattering modulate the magnetoresistivity / magnetoconductivity of a 2DLG compared with an undisturbed 2DLG?
It was shown that both background modulations can be explained by the different memory contributions, which are highly dependent on the applied magnetic field. At low magnetic fields, additional static background scattering reduced the conductivity because the static obstacles of the secondary 2DLG opened additional retroreflecting corridors. In this magnetic field regime, dynamic scattering, provided by phonons, increased the conductivity. This was explained by electrons being de-pinned from their initial trajectory because of scattering at phonons [29].
At magnetic fields where guided $\vec{E} \times \vec{B}$ drifting along the contour of obstacles causes a maximum in conductivity [15, 30], both types of background scattering reduced the conductivity. This is explained by the de-pinning of the electron from this guided path. At elevated magnetic fields, on the other hand, the decreased cyclotron radius caused bound states of the electrons in closed orbits around voids or assemblies of LG-obstacles, which reduced the conductivity and marked the percolation transition. [18] Both types of background scattering have the same influence in this regime, which is to increase the conductivity; the electrons are de-pinned from bound states.

The first two major research questions dealt with 2DLGs for which the density of obstacles is in the dense limit. The dilute limit, on the other hand, offers other exciting questions because for this regime, analytic expressions of magnetotransport have been provided. [19, 24] Moreover, GNMR [14, 31, 32] occurs in unpatterned plain 2DEG samples, which raises the following question, addressed as the main research question in Chapter 6: *How does a 2DLG modulate giant negative magnetoresistance?*
The experimental results presented in Chapter 6: suggested that the middle peak of GNMR is caused by both scattering at the sample edges [64] and a dilute 2DLG existing in pristine samples due to defects [32] that occur during sample growth. The experimental observations at the lowest temperature were in qualitative agreement with the interaction model. [23, 71] Within this model, Polyakov et al. predicted the long-range disorder to become more important as the magnetic field increases. At low magnetic fields, on the other hand, strong magnetoresistance modulations were found because of the hard scattering at LG-obstacles. The percolation magnetic field provided in theory [18] was

approximately the same as the magnetic field at which the magnetoresistivity only exhibited a low temperature dependence. This confirms the idea that the outer part of the 2DLG magnetoresistivity is dominated by long-range scattering. These observations are consistent with the measurements of applied in-plane magnetic fields, temperature, and varied sample width.
In addition, it was found that the middle peak of GNMR is caused by short-range scattering caused by oval defects, the sample walls, and LG-obstacles.
The hydrodynamic model [34], on the other hand, provided agreement with the magnetoresistivities of dilute 2DLGs measured at elevated temperatures, at which the interaction model does not provide predictions.

Finally in Chapter 7, nonequilibrium effects were addressed. The main research question was as follows:
Do nonequilibrium effects exist in the magnetoresistivity of 2DLGs, and how does the magnetic field interval in which they might occur correlate to the properties of 2DLGs?
Nonequilibrium $1/B$-phenomena [17] could not be observed in magnetic fields intervals that were dominated by the 2DLG (i.e., at magnetic fields below the percolation threshold). Therefore, the percolation magnetic field provides a lower boundary, above which all nonequilibrium phenomena are measurable. This characteristic was also found for the nonpatterned samples. Within the small and temperature-independent peak of GNMR, no $1/B$-periodicity occurred. This was in accordance with the finding that at these low magnetic fields, short-range scattering dominates, which is caused by the dilute 2DLG formed by oval defects and the sample edge potential. [32, 64, 91]
Another major finding was that when a 2DEG is subjected to THz irradiation, acoustic PIRO were observed rather than oscillations directly caused by photons. When the same experiment was performed at GHz irradiation, MIRO aere observed and PIRO remained absent. This indicated that in different frequency regions, different mechanisms dominate magnetoresistance. [151]

This thesis evaluated different aspects of the magnetotransport of 2DLGs. This fascinating system offers several further universal features, which lack a comprehensive understanding.
One question left open is how the magnetotransport of a retroreflecting 2DLG is modified by an additional secondary 2DLG of lower density as a static background disorder source. How does the static background influence the observed local maximum at low magnetic fields? This local maximum is a signature of the anomalous transport predicted by the EWT, such that high modulations are expected from an additional source of static background disorder.
Another path is the study of bimodal 2DLGs at sub-Kelvin temperatures. It would be interesting to analyze whether the magnetoresistance of secondary 2DLGs approaches the predictions of Bobylev et al. [19], with a further reduction in phonon scattering. Here and for the results concerning the dilute 2DLGs, MD simulations are desirable, which would allow the contributions from long-range scattering and its interaction with short-range scattering contributions to be distinguished.

Moreover, a question left open is to what extent quantum effects influence the transport properties of 2DLGs. At large magnetic fields, Landau quantization causes a strong modulation of the density of states, which is clearly visible in experiments through the onset of SdHo. Weak localization occurring around zero magnetic field is another quantum effect that could influence magnetotransport. In studies thus far, contributions of weak localization around zero magnetic field could not be identified, but because such localization requires the electronic wave function to split into two partial beams, a strong dependence on the obstacle size and diffusivity is expected. For both issues, quantum simulations are desirable.

In Chapter 7, nonequilibrium phenomena were presented. PIRO were observed once THz irradiated the 2DLG samples. Here, enhanced control of THz radiation would be desirable (i.e., its spectral resolution and polarization). Which type of phonons (bulk or interface) are involved in the process remains to be investigated. Thus far, the coupling constants and transition rates of relevant processes are unknown, as are their frequency dependence.

BIBLIOGRAPHY

[1] H. Lorentz,
Proc. R. Acad. Sci. Amsterdam **7**, 438 (1905).

[2] P. G. Kennedy,
The Lancet Neurology **12**, 186 (2013).

[3] T. Krüger and M. Engstler,
The European Physical Journal Special Topics **225**, 2157 (2016).

[4] M. R. Horton, F. Höfling, J. O. Rädler, and T. Franosch,
Soft Matter **6**, 2648 (2010).

[5] F. Höfling, T. Franosch, and E. Frey,
Phys. Rev. Lett. **96**, 165901 (2006).

[6] T. O. E. Skinner, S. K. Schnyder, D. G. A. L. Aarts, J. Horbach, and R. P. A. Dullens,
Phys. Rev. Lett. **111**, 128301 (2013).

[7] S. K. Schnyder, M. Spanner, F. Hofling, T. Franosch, and J. Horbach,
Soft Matter **11**, 701 (2015).

[8] F. Kümmel, B. ten Hagen, R. Wittkowski, I. Buttinoni, R. Eichhorn, G. Volpe, H. Löwen, and C. Bechinger,
Phys. Rev. Lett. **110**, 198302 (2013).

[9] M. Han, J. Yan, S. Granick, and E. Luijten,
Proceedings of the National Academy of Sciences **114**, 7513 (2017).

[10] M. Zeitz, K. Wolff, and H. Stark,
The European Physical Journal E **40**, 23 (2017).

[11] B. C. Steele and A. Heinzel,
in *Materials For Sustainable Energy: A Collection of Peer-Reviewed Research and Review Articles from Nature Publishing Group*, World Scientific, 2011, pp. 224–231.

[12] A. Kloke,
Adv. Mater **24**, 2916 (2012).

[13] C. Leang, N. S. Malvankar, A. E. Franks, K. P. Nevin, and D. R. Lovley,
Energy & Environmental Science **6**, 1901 (2013).

[14] L. Bockhorn, I. V. Gornyi, D. Schuh, C. Reichl, W. Wegscheider, and R. J. Haug,
Phys. Rev. B **90**, 165434 (2014).

[15] N. H. Siboni, J. Schluck, K. Pierz, H. W. Schumacher, D. Kazazis, J. Horbach, and T. Heinzel,
Phys. Rev. Lett. **120**, 056601 (2018).

[16] J. Schluck, M. Hund, T. Heckenthaler, T. Heinzel, N. Siboni, J. Horbach, K. Pierz, H. Schumacher, D. Kazazis, U. Gennser, et al.,
Phys. Rev. B **97**, 115301 (2018).

[17] I. A. Dmitriev, A. D. Mirlin, D. G. Polyakov, and M. A. Zudov,
Rev. Mod. Phys. **84**, 1709 (2012).

[18] A. Kuzmany and H. Spohn,
Phys. Rev. E **57**, 5544 (1998).

[19] A. V. Bobylev, F. A. Maaø, A. Hansen, and E. H. Hauge,
Phys. Rev. Lett. **75**, 197 (1995).

[20] P. Drude,
Annalen der Physik **306**, 566 (1900).

[21] E. M. Baskin, L. N. Magarill, and M. V. Entin,
Sov. Phys. JETP **48**, 365 (1978).

[22] A. Dmitriev, M. Dyakonov, and R. Jullien,
Phys. Rev. B **64**, 233321 (2001).

[23] D. G. Polyakov, F. Evers, A. D. Mirlin, and P. Wölfle,
Phys. Rev. B **64**, 205306 (2001).

[24] A. Dmitriev, M. Dyakonov, and R. Jullien,
Phys. Rev. Lett. **89**, 266804 (2002).

[25] R. Lohmann, B. Horn-Cosfeld, J. Schluck, M. Dominique, H. Schumacher, K. Pierz, T. Heinzel, and J. Horbach,
under review .

[26] J. Schluck,
Heinrich-Heine-Univeristät Düsseldorf, PhD Thesis (2018).

[27] P. Ehrenfest,
Collected Scientific Papers , 229 (1959).

[28] W. W. Wood and F. Lado,
J. Comp. Phys. **7**, 528 (1971).

[29] B. Horn-Cosfeld, J. Schluck, A. Röben, M. Cerchez, K. Pierz, H. Schumacher, D. Mailly, and T. Heinzel,
EPL **128**, 67004 (2019).

[30] W. Schirmacher, B. Fuchs, F. Höfling, and T. Franosch,
Phys. Rev. Lett. **115**, 240602 (2015).

[31] R. G. Mani, A. Kriisa, and W. Wegscheider,
Scientific Reports **3**, 02747 (2013).

[32] L. Bockhorn, A. Velieva, S. Hakim, T. Wagner, E. P. Rugeramigabo, D. Schuh, C. Reichl, W. Wegscheider, and R. J. Haug,
Appl. Phys. Lett. **108**, 092103 (2016).

[33] L. Bockhorn, A. Hodaei, D. Schuh, W. Wegscheider, and R. J. Haug,
Journal of Physics: Conference Series **456**, 012003 (2013).

[34] P. Alekseev,
Phys. Rev. Lett. **117**, 166601 (2016).

[35] A. D. Mirlin, E. Tsitsishvili, and P. Wölfle,
Phys. Rev. B **63**, 245310 (2001).

[36] Y. Beltukov and M. Dyakonov,
Phys. Rev. Lett. **116**, 176801 (2016).

[37] P.-G. De Gennes,
Superconductivity of metals and alloys,
CRC Press, 2018.

[38] A. De Waele,
Journal of Low Temperature Physics **164**, 179 (2011).

[39] F. Pobell,
Matter and methods at low temperatures, volume 2,
Springer, 2007.

[40] H. London, G. Clarke, and E. Mendoza,
Phys. Rev. **128**, 1992 (1962).

[41] O. V. Lounasmaa,
Experimental principles and methods below 1K,
Academic Press, 1974.

[42] R. Mehrotra, C. J. Guo, Y. Z. Ruan, D. B. Mast, and A. J. Dahm,
Phys. Rev. B. **29**, 5239 (1984).

[43] F. M. Peeters and P. M. Platzman,
Phys. Rev. Lett. **50**, 2021 (1983).

[44] E. Fortunato, P. Barquinha, and R. Martins,
Adv. Mater **24**, 2945 (2012).

[45] Y. Zhang, Y.-W. Tan, H. L. Stormer, and P. Kim,
Nature (London) **438**, 201 (2005).

[46] T. Ando, A. B. Fowler, and F. Stern,
Rev. Mod. Phys. **54**, 437 (1982).

[47] M. Z. Hasan and C. L. Kane,
Rev. Mod. Phys. **82**, 3045 (2010).

[48] M. J. Manfra,
Annu. Rev. Condens. Matter Phys. **5**, 347 (2014).

[49] T. Heinzel,
Mesoscopic Electronics in Solid State Nanostructures,
Wiley-VCH, 2007.

[50] R. Dingle, H. L. Störmer, A. C. Gossard, and W. Wiegmann,
Appl. Phys. Lett. **33**, 665 (1978).

[51] P. Yu and M. Cardona,
Fundamentals of Semiconductors,
Springer, Berlin, 1999.

[52] S. Succi,
The lattice Boltzmann equation: for fluid dynamics and beyond,
Oxford University Press, 2001.

[53] A. Sommerfeld and H. Bethe,
in *Aufbau Der zusammenhängenden materie*, Springer, 1933, pp. 333–622.

[54] M. Levinshtein,
Handbook series on semiconductor parameters, volume 1,
World Scientific, 1997.

[55] R. Peierls,
Zeitschrift für Physik **80**, 763 (1933).

[56] L. Landau,
Zeitschrift für Physik **64**, 629 (1930).

[57] I. Yugova, A. Greilich, D. Yakovlev, A. Kiselev, M. Bayer, V. Petrov, Y. K. Dolgikh, D. Reuter, and A. Wieck,
Phys. Rev. B **75**, 245302 (2007).

[58] L. Shubnikov and W. J. De Haas,
Nature **126**, 500 EP (1930).

[59] K. von Klitzing, G. Dorda, and M. Pepper,
Phys. Rev. Lett. **45**, 494 (1980).

[60] D. C. Tsui, H. L. Stormer, and A. C. Gossard,
Phys. Rev. Lett. **48**, 1559 (1982).

[61] C. W. J. Beenakker and H. van Houten,
Solid State Physics, volume 44,
Academic Press, 1991.

[62] R. Taboryski and P. E. Lindelof,
Semiconductor science and technology **5**, 933 (1990).

[63] G. Bergmann,
Physics Reports **107**, 1 (1984).

[64] T. J. Thornton, M. L. Roukes, A. Scherer, and B. P. van de Gaag,
Phys. Rev. Lett. **63**, 2128 (1989).

[65] L. Bockhorn, P. Barthold, D. Schuh, W. Wegscheider, and R. J. Haug,
Phys. Rev. B **83**, 113301 (2011).

[66] A. T. Hatke, M. A. Zudov, J. L. Reno, L. N. Pfeiffer, and K. W. West,
Phys. Rev. B **85**, 081304(R) (2012).

[67] V. Umansky, R. de Picciotto, and M. Heiblum,
Appl. Phys. Lett. **71**, 683 (1997).

[68] Q. Shi, P. D. Martin, Q. A. Ebner, M. A. Zudov, L. N. Pfeiffer, and K. W. West,
Phys. Rev. B **89**, 201301(R) (2014).

[69] R. L. Samaraweera, H.-C. Liu, B. Gunawardana, A. Kriisa, C. Reichl, W. Wegscheider, and R. G. Mani,
Scientific Reports **8**, 10061 (2018).

[70] V. Senz,
PhD Thesis,
PhD thesis, ETH Zürich, 2002.

[71] A. D. Mirlin, D. G. Polyakov, F. Evers, and P. Wölfle,
Phys. Rev. Lett. **87**, 126805 (2001).

[72] I. Gornyi and A. Mirlin,
Phys. Rev. Lett. **90**, 076801 (2003).

[73] L. Li, Y. Proskuryakov, A. Savchenko, E. Linfield, and D. Ritchie,
Phys. Rev. Lett. **90**, 076802 (2003).

[74] Y. Dai, R. R. Du, L. N. Pfeiffer, and K. W. West,
Phys. Rev. Lett. **105**, 246802 (2010).

[75] R. Gurzhi,
Sov. Phys. JETP **19**, 490 (1964).

[76] R. Gurzhi and S. Shevchenko,
Sov. Phys. JETP **27**, 1019 (1968).

[77] R. Gurzhi et al.,
Sov. Phys. Usp **11**, 255 (1968).

[78] L. Molenkamp and M. De Jong,
Phys. Rev. B **49**, 5038 (1994).

[79] R. Gurzhi, A. Kalinenko, and A. Kopeliovich,
Phys. Rev. Lett. **74**, 3872 (1995).

[80] H. Buhmann, L. Molenkamp, R. Gurzhi, A. Kalinenko, A. Kopeliovich, and A. Yanovsky,
Low Temperature Physics **24**, 737 (1998).

[81] H. Predel, H. Buhmann, L. Molenkamp, R. Gurzhi, A. Kalinenko, A. Kopeliovich, and A. Yanovsky,
Phys. Rev. B **62**, 2057 (2000).

[82] A. Tomadin, G. Vignale, and M. Polini,
Phys. Rev. Lett. **113**, 235901 (2014).

[83] M. Mendoza, H. J. Herrmann, and S. Succi,
Scientific Reports **3**, 1052 (2013).

[84] A. Andreev, S. A. Kivelson, and B. Spivak,
Phys. Rev. Lett. **106**, 256804 (2011).

[85] T. Scaffidi, N. Nandi, B. Schmidt, A. P. Mackenzie, and J. E. Moore,
Phys. Rev. Lett. **118**, 226601 (2017).

[86] Z. Qian and G. Vignale,
Phys. Rev. B **71**, 075112 (2005).

[87] A. Hatke, M. Zudov, J. Watson, M. J. Manfra, L. Pfeiffer, and K. West,
Phys. Rev. B **87**, 161307 (2013).

[88] G. Gusev, A. Levin, E. Levinson, and A. Bakarov,
AIP Advances **8**, 025318 (2018).

[89] A. Levin, G. Gusev, E. Levinson, Z. Kvon, and A. Bakarov,
Phys. Rev. B **97**, 245308 (2018).

[90] G. Gusev, A. Levin, E. Levinson, and A. Bakarov,
Phys. Rev. B **98**, 161303 (2018).

[91] P. Alekseev and M. Semina,
Phys. Rev. B **98**, 165412 (2018).

[92] V. V. Cheianov, A. P. Dmitriev, and V. Y. Kachorovskii,
Phys. Rev. B **68**, 201304 (R) (2003).

[93] J. Schluck, S. Fasbender, T. Heinzel, K. Pierz, H. W. Schumacher, D. Kazazis, and U. Gennser,
Phys. Rev. B **91**, 195303 (2015).

[94] F. Höfling and T. Franosch,
Reports on Progress in Physics **76**, 046602 (2013).

[95] A. Morin, D. L. Cardozo, V. Chikkadi, and D. Bartolo,
Phys. Rev. E **96**, 042611 (2017).

[96] C. O. Reichhardt and C. Reichhardt,
New Journal of Physics **20**, 025002 (2018).

[97] T. Bauer, F. Höfling, T. Munk, E. Frey, and T. Franosch,
The European Physical Journal Special Topics **189**, 103 (2010).

[98] S. K. Schnyder and J. Horbach,
Phys. Rev. Lett. **120**, 078001 (2018).

[99] K. Ērglis, Q. Wen, V. Ose, A. Zeltins, A. Sharipo, P. A. Janmey, and A. Cēbers,
Biophysical Journal **93**, 1402 (2007).

[100] K. Martens, L. Angelani, R. Di Leonardo, and L. Bocquet,
The European Physical Journal E **35**, 84 (2012).

[101] E. Baskin and M. Entin,
Physica B: Condensed Matter **249-251**, 805 (1998).

[102] Y. G. Chai and R. Chow,
Appl. Phys. Lett. **38**, 796 (1981).

[103] K. Akimoto, M. Dohsen, M. Arai, and N. Watanabe,
Journal of Crystal Growth **73**, 117 (1985).

[104] S.-L. Weng,
Appl. Phys. Lett. **49**, 345 (1986).

[105] M. Shinohara and T. Ito,
Journal of Applied Physics **65**, 4260 (1989).

[106] S. Mertens and C. Moore,
Phys. Rev. E **86**, 061109 (2012).

[107] P. Ehrenfest and T. Ehrenfest,
Encyklopädie der mathematischen Wissenschaften **4**, 32 (1911).

[108] D. Gates,
Journal of Mathematical Physics **13**, 1315 (1972).

[109] E. H. Hauge and E. G. D. Cohen,
Journal of Mathematical Physics **15**, 397 (1969).

[110] E. H. Hauge and E. G. D. Cohen,
Phys. Rev. Lett. **25A**, 78 (1967).

[111] H. V. Beyeren and E. H. Hauge,
Phys. Rev. Lett. **39A**, 397 (1972).

[112] C. L. Yang, J. Zhang, R. R. Du, J. A. Simmons, and J. L. Reno,
Phys. Rev. Lett. **89**, 076801 (2002).

[113] M. A. Zudov, I. V. Ponomarev, A. L. Efros, R. R. Du, J. A. Simmons, , and J. L. Reno,
Phys. Rev. Lett. **86**, 3614 (2001).

[114] M. A. Zudov, R. R. Du, J. A. Simmons, and J. L. Reno,
Phys. Rev. B **64**, 201311 (2001).

[115] R. G. Mani, J. H. Smet, K. von Klitzing, V. Narayanamurti, W. B. Johnson, and V. Umansky,
Nature **420**, 646 (2002).

[116] C. L. Yang, M. A. Zudov, T. A. Knuuttila, R. R. Du, L. N. Pfeiffer, and K. W. West,
Phys. Rev. Lett. **91**, 096803 (2003).

[117] A. Bykov, I. Marchishin, A. Goran, and D. Dmitriev,
Appl. Phys. Lett. **97**, 082107 (2010).

[118] Z. Yuan, C. Yang, R. Du, L. Pfeiffer, and K. West,
Phys. Rev. B **74**, 075313 (2006).

[119] S. Wiedmann, G. Gusev, O. Raichev, T. Lamas, A. Bakarov, and J. Portal,
Phys. Rev. B **78**, 121301 (2008).

[120] R. G. Mani,
Appl. Phys. Lett. **85**, 4962 (2004).

[121] R. G. Mani, C. Gerl, S. Schmult, W. Wegscheider, and V. Umansky,
Phys. Rev. B **81**, 125320 (2010).

[122] M. Vavilov, I. Dmitriev, I. Aleiner, A. Mirlin, and D. Polyakov,
Phys. Rev. B **70**, 161306 (2004).

[123] A. T. Hatke, M. A. Zudov, L. N. Pfeiffer, and K. W. West,
Phys. Rev. B **84**, 121301 (2011).

[124] A. Wirthmann, B. D. McCombe, D. Heitmann, S. Holland, K.-J. Friedland, and C.-M. Hu,
Phys. Rev. B **76**, 195315 (2007).

[125] Z. D. Kvon, D. A. Kozlov, S. N. Danilov, C. Zoth, P. Vierling, S. Stachel, V. V. Bel'kov, A. K. Bakarov, D. V. Dmitriev, A. I. Toropov, and S. D. Ganichev,
JETP Lett. **97**, 41 (2013).

[126] M. A. Zudov, R. R. Du, L. N. Pfeiffer, and K. W. West,
Phys. Rev. B **73**, 041303 (2006).

[127] I. Dmitriev, M. Vavilov, I. Aleiner, A. Mirlin, and D. Polyakov,
Phys. Rev. B **71**, 115316 (2005).

[128] A. C. Durst, S. Sachdev, N. Read, and S. Girvin,
Physica E: Low-dimensional Systems and Nanostructures **20**, 117 (2003).

[129] D. Tsui, G. Dolan, and A. Gossard,
Bull. Am. Phys. Soc **28**, 365 (1983).

[130] W. Zhang, M. A. Zudov, L. N. Pfeiffer, and K. W. West,
Phys. Rev. Lett. **100**, 036805 (2008).

[131] D. Strauch and B. Dorner,
J. Phys. Condens. Matter **2**, 1457 (1990).

[132] V. Gurevich and Y. A. Firsov,
Soviet Phys. JETP **13**, 137 (1961).

[133] D. Tsui, T. Englert, A. Cho, and A. Gossard,
Phys. Rev. Lett. **44**, 341 (1980).

[134] A. T. Hatke, M. A. Zudov, L. N. Pfeiffer, and K. W. West,
Phys. Rev. Lett. **102**, 086808 (2009).

[135] A. A. Bykov and A. V. Goran,
JETP Lett. **90**, 578 (2009).

[136] I. A. Dmitriev, R. Gellmann, and M. G. Vavilov,
Phys. Rev. Lett. **82**, 201311 (2010).

[137] O. E. Raichev,
Phys. Rev. B **80**, 075318 (2009).

[138] R. Lohmann,
Heinrich-Heine-Univeristät Düsseldorf, Master Thesis (2019).

[139] T. Ando,
J. Phys. Soc. Jpn. **36**, 959 (1974).

[140] J.-S. Ferenc and Z. Néda,
Physica A: Statistical Mechanics and its Applications **385**, 518 (2007).

[141] J. Schluck, M. Hund, T. Heckenthaler, T. Heinzel, N. Siboni, J. Horbach, K. Pierz, H. Schumacher, D. Kazazis, U. Gennser, et al.,
Phys. Rev. B **97**, 115301 (2018).

[142] S. Hikami, A. I. Larkin, and Y. Nagaoka,
Progress of Theoretical Physics **63**, 707 (1980).

[143] I. Gornyi and A. Mirlin,
Phys. Rev. B **69**, 045313 (2004).

[144] C. Yang, R. Du, L. Pfeiffer, and K. West,
Phys. Rev. B **74**, 045315 (2006).

[145] E. Zaremba,
Phys. Rev. B **45**, 14143 (1992).

[146] T. Ando,
J. Phys. Soc. Jpn. **36**, 1521 (1974).

[147] J. Heisz and E. Zaremba,
Phys. Rev. B **53**, 13594 (1996).

[148] L. Bockhorn, J. Inarrea, and R. Haug,
arXiv:1504.00555 (2015).

[149] A. A. Bykov,
JETP Lett. **88**, 394 (2008).

[150] A. A. Bykov, A. K. Kalagin, and A. K. Bakarov,
JETP Lett. **81**, 523 (2005).

[151] B. Horn-Cosfeld, M. Cerchez, T. Heinzel, L. Freise, K. Pierz, and H. Schumacher,
Phys. Rev. B **100**, 245407 (2019).

[152] Z. Wang, R. L. Samaraweera, C. Reichl, W. Wegscheider, and R. G. Mani,
Scientific reports **6**, 38516 (2016).

[153] C. Walther, M. Fischer, G. Scalari, R. Terazzi, N. Hoyler, and J. Faist,
Appl. Phys. Lett. **91**, 131122 (2007).

[154] B. S. Williams,
Nature Photonics **1**, 517 (2007).

[155] Alpes Lasers S. A., http://www.alpeslasers.ch .

[156] T. Arikawa, X. Wang, A. A. Belyanin, and J. Kono,
Optics Express **20**, 19484 (2012).

[157] D. Suzuki, S. Oda, and Y. Kawano,
Appl. Phys. Lett. **102**, 122102 (2013).

[158] Thorlabs GmbH, product number: FB19M150, https://www.thorlabs.com .

[159] K. Hirakawa, K. Yamanaka, Y. Kawaguchi, M. Endo, and M. Saeki,
Phys. Rev. B **63**, 085320 (2001).

[160] H. Sakuma, K. Ikushima, S. Komiyama, and K. Hirakawa,
Infrared Physics and Technology **48**, 235 (2006).

[161] F. Neppl, J. P. Kotthaus, and J. F. Koch,
Phys. Rev. B **19**, 5240 (1979).

[162] Y. Kawano, Y. Hisanaga, H. Takenouchi, and S. Komiyama,
Journal of Applied Physics **89**, 4037 (2001).

[163] N. G. Kalugin, Y. B. Vasilyev, S. D. Suchalkin, G. Nachtwei, B. E. Sagol, and K. Eberl,
Phys. Rev. B **66**, 085308 (2002).

[164] J. Zhang, S. K. Lyo, R. R. Du, J. A. Simmons, and J. L. Reno,
Phys. Rev. Lett. **92**, 156802 (2004).

[165] T. Ando,
J. Phys. Soc. Jpn. **37**, 1044 (1974).

[166] L. Brillouin,
Ann. Physique **17**, 88 (1922).

[167] R. G. Ulbricht and C. Weisbuch,
Resonant Brillouin scattering in semiconductors,
Springer, 1978.

[168] A. Pine,
in *Light Scattering in Solids I*, Springer, 1983, pp. 253–273.

[169] M. D. McCluskey,
Journal of Applied Physics **87**, 3593 (2000).

[170] P. A. Russel, F. F. Ouali, N. P. Hewett, and L. J. Challis,
Surface Science **229**, 54 (1990).

[171] S. Komiyama, T. Takamasu, S. Hiyamizu, and S. Sasa,
Solid State Communications **54**, 479 (1985).

[172] W. Xiaoguang, F. M. Peeters, and J. T. Devreese,
Phys. Rev. B **32**, 6982 (1985).

[173] M. Cankurtaran, H. Çelik, and N. Balkan,
Phys. Stat. Sol. **229**, 1191 (2002).

[174] D. R. Leadley, R. J. Nicholas, J. J. Harris, and C. T. Foxon, Semicond. Sci. Technol. **4**, 879 (1989).

[175] P. Hawker, A. J. Kent, O. H. Hughes, and L. J. Challis, Semicond. Sci. Technol. **7**, B29 (1992).

Supplementary Figures – Section 4.2

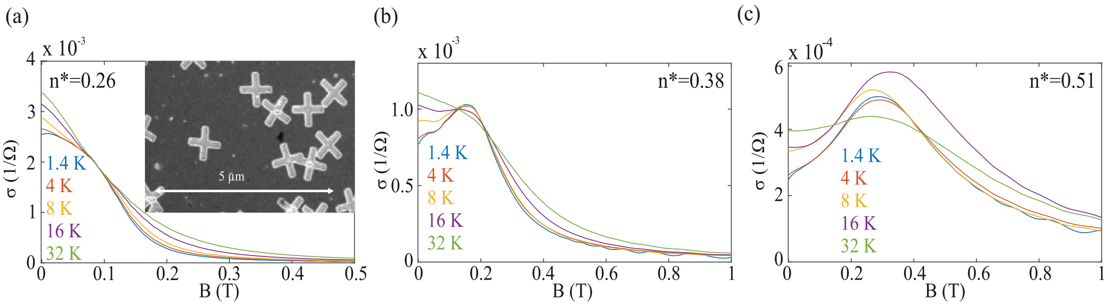

Figure 8.1: Temperature dependency of the measured magnetoconductivities for randomly oriented RC 2DLGs with different n^* and $d = 850\,\text{nm}$. The scanning electron microscopy image in the inset of (a) shows a sample section.

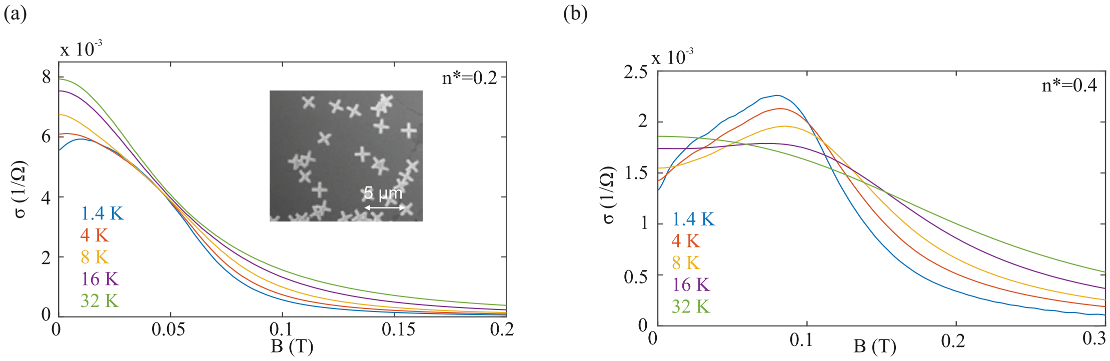

Figure 8.2: Magnetoconductivity traces for $n^* = 0.2$ (a) and $n^* = 0.4$ (b) for the $d = 1850\,\text{nm}$ sized RCs at different temperatures. The inset in (a) shows a scanning electron microscopy image of a sample section.

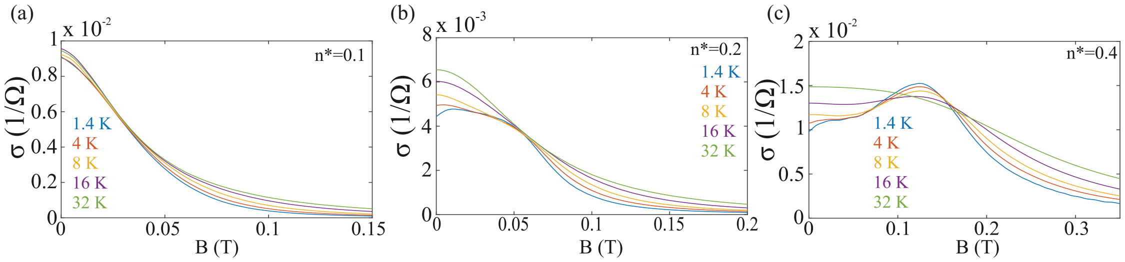

Figure 8.3: Magnetoconductivity of $d = 1850\,\mathrm{nm}$ sized equally oriented RCs with dimensionless densities of $n^* = 0.1$ (a), $n^* = 0.2$ (b), and $n^* = 0.4$ (c).

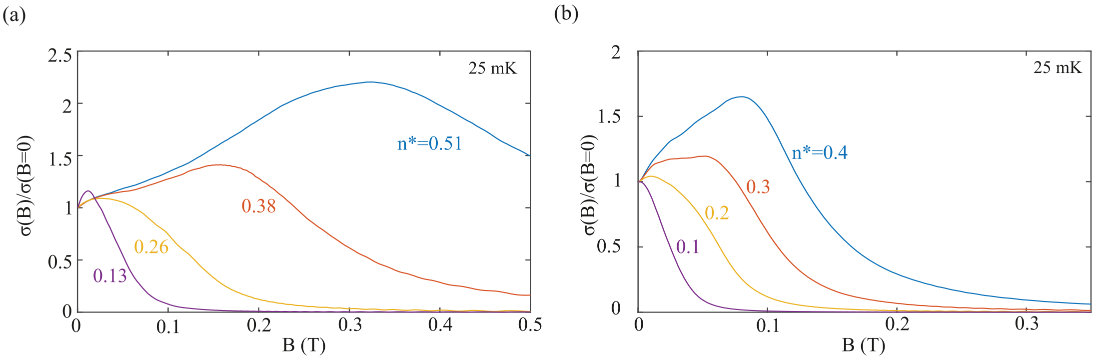

Figure 8.4: Normalized magnetoconductivity of the $d = 850\,\mathrm{nm}$ (a) and $d = 1850\,\mathrm{nm}$ (b) randomly oriented RCs. Most of the measurement traces exhibit a similar slope near $B = 0$, indicating that they share a similar exponent δ approaching $\tilde{B} = 0$: $\sigma_{xx} \propto \tilde{B}^{\delta}$.

Supplemental Figures – Chapter 5

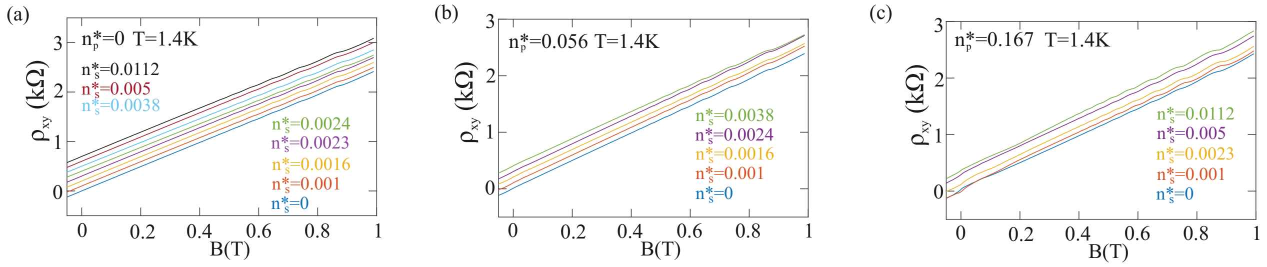

Figure 8.5: Hall-resistivities of (a) the secondary 2DLGs, (b) the bimodal 2DLGs with $n_p^* = 0.056$, and (c) the bimodal 2DLGs with $n_p^* = 0.167$. The respective plain and unimodal 2DLGs are also included. Each subsequent trace has an offset of 100 Ω for the sake of clarity.

Fig. 1: (Colour on-line) Hall resistivities of (a) the secondary Lorentz gases, (b) the bimodal arrays with $n_p^\star = 0.056$, and (c) the bimodal 2DLGs with $n_p^\star = 0.167$. In (b) and (c), the corresponding unimodal primary 2DLGs are included as well. In all figures, subsequent traces are offset for clarity by 100 Ω.

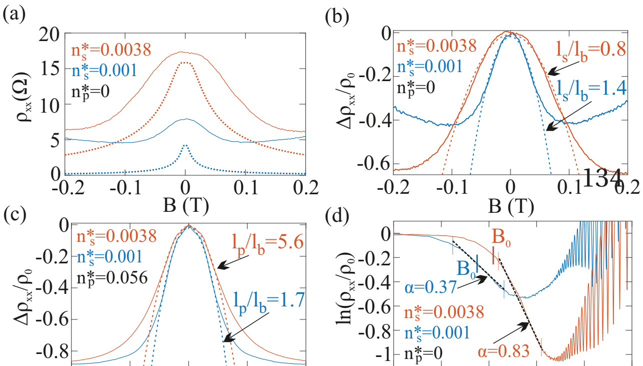

Also, the pattern transfer of the 2DLG may have generated additional disorder. However, a study of all unimodal primary arrays shows that the fit value of ℓ_b decreases systematically as n_s is increased. This indicates that in our samples, the background scattering length as obtained from the parabolic fits and the scattering at the Lorentz obstacles are interdependent, an observation which may be worth further theoretical study. Finally, it should be mentioned that at least for our samples with low $n_s^\star$, the condition $\ell_s \ll \ell_b$ required for eq. 2 to hold, is not strictly fulfilled.

DANKSAGUNG

Diese Seiten meiner Dissertation möchte ich mit großer Freude all denen widmen, die mich bei meiner Promotion unterstützt haben.

Vielen Dank an meinen Doktorvater Professor Thomas Heinzel dafür, dass mir die Möglichkeit geboten wurde an seinem Lehrstuhl für Festkörperphysik zu promovieren. Du warst immer ein unterstützender Ansprechpartner bei allen Projekten, der voller Begeisterung hinter seiner Forschung steht. Ich habe während meiner Promotionszeit nie den Rückhalt vermisst, wofür ich dir sehr dankbar bin. Danke auch dafür, dass ich die Gelegenheit hatte beim APS March Meeting in Boston 2019 und einigen anderen Tagungen die Arbeiten vor internationalem Fachpublikum zu präsentieren.

Ich danke Professor Jürgen Horbach für die Übernahme des Koreferats. Vielen Dank für deine Unterstützung und die vielen Diskussionen im Rahmen unserer erfolgreichen Zusammenarbeit zu den Retroreflektierenden 2D-Lorentzgasen. Ich wünsche viel Erfolg für den weiteren Projektverlauf und würde mich freuen bei der Frage nach den Abweichungen im Hall-Effekt beitragen zu können.

Mein Dank gilt zudem PD Dr. Mihai Cerchez. Vielen Dank, dass Du stets ansprechbar warst und mir geduldig mit Rat und Tat zu Seite standest, sei es im Labor, bei der Konzeptionierung der Experimente oder bei der Interpretation der Ergebnisse. Von Thomas und Dir habe ich gelernt, mit unbändiger Gelassenheit und Souveränität den Problemen im Labor zu begegnen und alle Energie auf ein problemlösungsorientiertes, effizientes und kreatives Arbeiten zu verwenden.

Vielen Dank an Jakob Schluck, von dem ich während unserer gemeinsamen Zeit in der Arbeitsgruppe viel Lernen konnte. Danke für die gelungene Übergabe des Lorentzgasprojektes.

Auch mit René Lohmann und Nima Siboni habe ich im Rahmen dieses Projektes zusammengearbeitet und möchte ihnen dafür danken.

Professor Hans Werner Schuhmacher und Dr. Klaus Pierz und von der PTB in Braunschweig danke ich für die Bereitstellung der wunderbaren, hochmobilen GaAs/AlGaAs Heterostrukturen. Vielen Dank an Lars Freise (PTB) für die Durchführung der MIRO Messungen im Rahmen des Terahertz-Projektes. Viel Erfolg bei der Fertigstellung deiner Dissertation.

Dr. Lina Bockhorn, von der Universität Hannover, danke ich für die gewinnbringenden Diskussionen und den wissenschaftlichen Austausch über dünne Lorentzgase.

PD Dr. Natham Jukam, Dr. Negar Hekmat, Dr. Sergej Markmann und Professor Andreas Wiek von der Ruhr-Universität Bochum möchte ich für viele hilfreiche Gespräche über Terahertz-Quantenkaskaden Laser, deren Handhabung und Eigenschaften danken.

Für technische Unterstützung danke ich Wilfried Gjungjek-Schützek, Uwe Zimmermann und Harald

Götz. Vielen Dank an Oliver Wyczisk und an seine Kollegen der Feinmechanik Werkstatt für den Bau des THz-QCL Probenhalters und anderer Anfertigungen und Reparaturen.

Bianka Lindenau möchte ich nicht nur für die vielen administrativen Dinge danken, die sie für mich erledigt hat, sondern auch für Ihre viele gute Laune und motivierenden Gespräche.

Auch die Betreuung von Bachelor- und Masterarbeiten hat mir viel Freude bereitet. Alles Gute und viel Erfolg weiterhin für Lukas, Felix, Andreas und Christopher.

Zudem möchte ich den anderen Doktoranden aus unserem Institut Laurin, Jakob, Svenja, Stefan und Christian für die nette Zusammenarbeit und den angenehmen Umgang danken.

Vielen Dank an Mihai, Jörg, Charlotte und Laurin, dass Ihr euch die Zeit für das Korrekturlesen genommen habt.

Einen großen Dank möchte ich meinen Eltern aussprechen. Vielen Dank Euch beiden für die enorme Unterstützung während des Studiums und der Promotionszeit.

Zu aller Letzt, vielen Dank an meinen Ehemann und die Konstante in meinem Leben Jörg. Danke, dass Du mich, wo du nur konntest, in der Promotionszeit unterstützt hast und ich mich immer auf Dich verlassen kann. Ich freue mich auf die vielen weiteren Abenteuer, die wir zusammen bestreiten werden.

EIDESSTATTLICHE VERSICHERUNG

Ich versichere an Eides Statt, dass die Dissertation von mir selbstständig und ohne unzulässige fremde Hilfe unter Beachtung der „Grundsätze zur Sicherung guter wissenschaftlicher Praxis an der Heinrich-Heine-Universität Düsseldorf“ erstellt worden ist.

(Beate Horn-Cosfeld)   Düsseldorf, Mär. 2020